3-24-2016

Effects of Additive Manufacturing Methods on the Dynamic Properties of 15-5PH Stainless Steel

Allison A. Dempsey

Effects of Additive Manufacturing Methods on the Dynamic Properties of 15-5PH Stainless Steel

THESIS

Allison A. Dempsey, Maj, USAF

AFIT-ENY-MS-16-M-205

DEPARTMENT OF THE AIR FORCE
AIR UNIVERSITY

AIR FORCE INSTITUTE OF TECHNOLOGY

Wright-Patterson Air Force Base, Ohio

AFIT-ENY-MS-16-M-205

EFFECTS OF ADDITIVE MANUFACTURING METHODS ON THE DYNAMIC PROPERTIES OF 15-5PH STAINLESS STEEL

THESIS

Presented to the Faculty

The Department of Aeronautics and Astronautics

Graduate School of Engineering and Management

Air Force Institute of Technology

Air University

Air Education and Training Command

in Partial Fulfillment of the Requirements for the

Degree of Master of Science in Aeronautical Engineering

Allison A. Dempsey, B.S., M.B.A.

Maj, USAF

March 2016

AFIT-ENY-MS-16-M-205

EFFECTS OF ADDITIVE MANUFACTURING METHODS ON THE DYNAMIC PROPERTIES OF 15-5PH STAINLESS STEEL

THESIS

Allison A. Dempsey, B.S., M.B.A.
Maj, USAF

Committee Membership:

Maj David Liu, PhD
Co-Chair

Dr. Anthony Palazotto, PhD
Co-Chair

Dr. Rachel Abrahams, PhD
Member

AFIT-ENY-MS-16-M-205

Abstract

Experimental research was conducted to determine the dynamic properties and characterize the microstructure of Stainless Steel manufactured through Direct Metal Laser Sintering (DMLS) additive manufacturing (AM) processes and heat treated using common heat treatment protocols. The intended material of study is 15-5PH stainless steel, one of the most common steel alloys used in aerospace applications. A thorough understanding of the material's properties is necessary before such parts are utilized in an operational capacity. This research assesses the expected dynamic properties at room temperature of parts made using 15-5PH stainless steel powder via DMLS with two different heat treatments and in two different build directions. Various techniques were used to determine the composition and examine the microstructure of the five total subject sets. Samples made from the sets were tested quasi-statically and dyamically, using a Split Hopkinson Bar (SHB) apparatus. Of the five builds, two deviated significantly from the specified composition of 15-5PH stainless steel, one of which contained a significant amount of retained austenite compared to the almost completely martensitic compositions of the other four. The remaining three builds, possessing the desired composition and crystalline structure, were tested in compression and tension at two strain rates. Tension tests using a reflected wave and a momentum trap SHB setup collected data reflecting a natural variation within builds and across builds and orientation of typically less than 7%. A slight build orientation bias is noted resulting in higher ductility of the horizontal build orientation compared to the vertical of the same material. A simplistic linear interpolation of true stress-strain curves show fairly consistent strain softening trends at higher strain rates across the material subject sets.

Acknowledgements

I would like to acknowledge several people who have helped me tremendously in this endeavor. First, my committee: Maj. Liu, Dr. Pallazotto, and Dr. Abrahams for their wisdom and advice. The sponsor, Mr. Don Littrell from AFRL/RW for enabling this project by envisioning the possibilities of additive manufacturing. A special thanks to Mr. Richard Harris and Mr. Philip Flater at AFRL/RW as well as Mr. Ronald Hoffman at UDRI for running these tests and helping interpret the results. Additionally, I appreciate the Materials Characterization Facility at AFRL/RX, particularly Kathleen Schugart, Bob Lewis, and Tommy Cissell. Finally, my family, for having the patience to let me spend the time needed to complete this research.

Allison A. Dempsey

Table of Contents

Page

Page

List of Acronyms

2D two-dimensional

3D three-dimensional

AFRL Air Force Research Laboratory

AM additive manufacturing

DMLS direct metal laser sintering

EBSD electron backscatter diffraction

EDS energy dispersive X-ray spectroscopy

EOS Electro Optical Systems

FDM fused deposition modeling

PH precipitation hardenable

SEM scanning electron eicroscope

SHB Split Hopkinson bar

SL stereolithography

SLM selective laser melting

SLS selective laser sintering

STF strain to failure

USAF United States Air Force

UTS Ultimate Tensile Stress

YS Yield Strain

List of Figures

List of Tables

List of Symbols

ϵ Strain

$\dot{\epsilon}$ Strain rate

σ Stress

EFFECTS OF ADDITIVE MANUFACTURING METHODS ON THE DYNAMIC PROPERTIES OF 15-5PH STAINLESS STEEL

I Introduction

A recent RAND report exhorts the world is on the cusp of a "Third Industrial Revolution" that will be driven by computer technology and additive manufacturing (AM) [4]. The 2013 science and technology vision document of the United States Air Force (USAF), Global Horizons, identifies AM as a "game changer" [5]. The computer based manufacturing capability known as AM, or 3D printing, refers to the body of techniques that build three-dimensional parts out of overlaying two dimensional cross-sections [6]. Because of its flexibility and capability, AM is predicted to bring many benefits to the armed services. Some potential benefits include the ability to fabricate parts using novel materials, provide mission specific reconfiguration ability, tailor material for specific applications, institute real-time structural health monitoring, reduce logistics time and overhead, and enable rapid replacement or repair for battle damage [5].

Although those are exciting capabilities, AM in the near term is drawing interest by opening up new avenues for weight and cost savings. Approximately 60,000 USAF weapon system component requisitions are ordered annually [7]. Many of these are costly due to low demand or obsolence, complex manufacturing, or high material waste in production. Once AM parts are approved for use in these applications, the manufacturing method holds particular promise for reverse engineering parts and for producing small batches quickly and cost effectively. Eliminating extensive machining and tool path planning could greatly reduce time and material waste. Enabling

complex geometries means parts can be optimized to fit an application without excess material, entire assemblies can be replaced with a single part without joints or welds, costly dies and molds can be replicated or eliminated. However, though AM techniques, equipment and technology have rapidly advanced in recent years, the maturity of many of the techniques and equipment are not sufficient enough for wide-spread, full rate manufacturing and reliability [4].

Daunting challenges in instituting AM in the USAF are linked to compliance with airplane safety and certification to meet performance standards. Investment is needed in research and development in all aspects of AM to ensure critical parts made with AM methods can meet the criteria for safety and end use suitability [4]. The Global Horizons vision calls for a redefined qualification and certification paradigm and advocates process qualification vice component qualification in order to take advantage of AM capability [5]. However, research and development can take advantage of AM's ability to directly manufacture complex structures that are not matchable by conventional methods to optimize those structures for new applications. A general comparison of the material of interest to the traditional material and an understanding of the property variation envelope goes beyond creating a new paradigm of certification to instead create a new design paradigm. A great benefit AM offers is optimized part design unencumbered by subtractive methods of shaping metal. Optimized design is intended to safely decrease weight by amassing material exactly where and in the form needed. In the case of high material variability, the safety and effectiveness of the optimized approach is compromised. This research into the dynamic properties of 15-5PH produced by direct metal laser sintering (DMLS) investigates how the 15-5PH AM material fares overall as a substitution for the traditional material, but also begins investigating the range and stability of AM specimens under dynamic loading conditions.

15-5PH, one of the most common stainless steel alloys used in aerospace applications, can be manufactured via a powder bed fusion AM process known as DMLS. The AM 15-5PH product has been shown to demonstrate static mechanical properties comparable to the wrought type of material [8]. However, it is possible there may be variations in material properties due to the method of manufacture. It is also conceivable there will be variability of the AM product due to the manufacturing process itself. The variety of options in DMLS and the idiosyncracies of building near net shape parts rather than standard geometries can introduce unintended effects. Potential effects include residual stresses, surface roughness, anisotropy, porosity, and changes in microstructure [6]. It is also unclear whether the 15-5PH AM material will react to heat treatment in the same manner as the traditional wrought material. One approach to addressing this issue is to perform dynamic testing of this material after typical heat treatment protocols under loading conditions of interest.

1.1 Research Scope

In order to achieve the reliability necessary for qualification, there needs to be a better understanding of the consistency of the equipment performance and a better understanding of the equipment parameter effects on the finished part or product [4]. Previous studies and anecdotal evidence suggests the properties of the AM material will be affected by the method of formation, but it is not clear exactly how much because of a lack of an established baseline of mechanical properties and structural performance under dynamic loading conditions. Several studies have demonstrated the mechanical and microstructural properties and quality depend on the type of AM technology, the base material, the layer thickness, build strategy, and post-processing [6]. There are few studies available regarding microstructure and mechanical properties of parts formed by DMLS using 15-5PH powder, and none

found regarding the resultant dynamic material properties. The focus of the research conducted in this study is to investigate the impact of build orientation and heat treatment upon the dynamic properties of AM stainless steel created from 15-5PH powder.

The material used in the tests will represent the AM material with specific variables introduced. To attempt to characterize the material itself without variability introduced from partially sintered powder, geometric instability, or surface roughness, all of the tensile specimens used were machined from larger AM shapes. Because of the way the material is built in successive layers, the strength and dynamic characteristics may change with build orientation [9]. Knowing the characteristics is important to designers and manufacturers, who may need to orient the way a part is printed to maximize its suitability for its intended application [4]. Comparison to the the wrought material and examination of the behavior variant after heat treatment is also desired.

This thesis furthers the knowledge of how using AM can produce variability in a product, and how the variability affects the properties of the intended final product. Each of the specimens intended for testing are manufactured with powder pre-alloyed to match the composition of one particular material, 15-5PH stainless steel. The paper pairs results of material tests (uniaxial tensile tests and dynamic strain rate reactions from results of Split Hopkinson Pressure Bar (SHB) tension and compression tests) to exploration of the localized effects of the impacts of the unique manufacturing method obtained via microscopy, backscatter diffraction, and failure mechanism assessment to ascertain any potential challenges if used in its traditional load conditions.

1.2 Background

For certain applications, AM is well established as a mainstream technology. Amid the current digital design boom of this seemingly space age technology, it is interesting to note the early AM visionaries emerged in the US in 1987 [10]. Many materials were tried; epoxy binders and ceramic powders, wax, paper, starch and paper, and traditional printer paper were used in the 1990s. Since 2002, 3D printers using thermoplastic material have been available for less than $500. A quick look online shows intriguing potential uses of 3D printing: manufacturing in space, new ways to improve turbine engine blades, customized bone and tooth replacement, and decorative food products, amid other things. AM is even currently used in the Department of Defense (DoD). Commodities groups in the USAF are using the printers mainly for prototypes and form, fit, function checks but are planning for more strategic uses of this manufacturing capability [11][12]. The US Navy's Fleet Readiness Center East in Cherry Point, NC, has used AM to create tooling to produce legacy spare parts threatened by obsolescence [4]. The US Army is investigating making weapon prototypes, warhead designs, and embedding electronic sensors into AM aircraft parts [9]. Although these examples are mostly confined to planning or supporting roles, boundaries to making AM viable in aerospace applications are currently being broken. In 2015, General Electric announced that the U.S. Federal Aviation Administration (FAA) cleared their first 3D printed part, housing for a compressor inlet temperature sensor, to fly [13]. Chinese scientists at Northwestern Polytechnical University in Xi'an have produced an 5m long AM titanium center wing spar that has met aviation standards and is expected to enter commercial service aboard a passenger plane in 2016 [14].

Investing resources into establishing a commercial US industrial base for defense applications is important to advancing the technology to where it can be of even greater benefit to the services [4]. DMLS, a process in which a laser fuses powder

materials together, was born during 1994 and 1995, a time of great advances for AM materials of interest to the aerospace industry. In 2010, EOS introduced the EOSINT M 280 system, used to make the material for this research. The machine has a dual mode system and can run in either a nitrogen or argon environment. The dual mode capability enables the manufacture of materials such as stainless steel and titanium alloys, with promise for use of nickel alloys, on a single machine type. In the past five years, there has been widespread use of AM machines, development of digital databases and best practices, testing and refinement of AM capabilities [10].

1.3 Research Objectives

The purpose of this research is to investigate the variation of the dynamic properties of AM 15-5PH stainless steel. Specifically, this thesis intends to examine the microstructure and determine the dynamic performance and variability of different batches of material built in juxtaposed orientations and subjected to common heat treatment protocols meant to age, or harden, the PH steel. To accomplish these objectives, extensive use of imaging techniques such as optical and scanning electron microscopy; characterization techniques such as energy dispersive x-ray spectroscopy (EDS) and electron backscatter diffraction (EBSD); and test apparatus such as the split hopkinson bar (SHB) and universal testing machine have been used. Ultimately, it will be determined if the microstructure and apparent composition of an AM part can be associated with its performance when subjected to a dynamic strain. The results offer an opportunity to see how intentional and natural variability in AM material might be characterized to quantify a standard or highlight potentially troubling variation.

Specifically, the research objectives for this project are threefold: First, to investigate the microstructure of different batches of 15-5PH material to determine the

effect of the manufacturing process upon the simple cylindrical shape. Second, to explore the dynamic results of two geometrically opposed build directions and two common heat treatment protocols. Finally, it will develop an estimate of the power law to compare to the properties of the wrought material.

1.4 Document Structure

This document is organized into five chapters. Chapter II provides background information on the microstructure of stainless steels and how a material is affected by alloying composition. It also describes possible AM process parameter effects and any observed heat treatment effects on the microstructure. Additionally, Chapter II gives an overview of the material, how to look at metallic microstructure, and how the SHB tests were conducted. Chapter III explains the methodology used to conduct this research and outlines how the coefficients were derived and what techniques were used to examine the microstructure. Chapter IV presents the results of the quasi-static and SHB tests and shows microstructure graphs and analyses. A summary of the results, final conclusions, and recommendations for future work are given in Chapter V. Additional information can be found in Appendices 1,2,3 and 4.

II Background & Theory

This chapter provides background information on the microstructure of the stainless steel material under scrutiny and describes possible AM process parameter effects. The known dynamic behavior of the traditional wrought material and the effects of heat treating it are described, followed by an overview of the SHB is used to obtain dynamic response of a material.

2.1 Additive Manufacturing Overview

AM is broadly described as a number of methods of producing parts by building up material instead of traditional subtractive processes. DMLS is one of several techniques under the umbrella term SLM. It is a powder bed fusion process, meaning it uses pre-alloyed metal powder melted or sintered in successive layers by a laser. Due to the nature of the layered formation, the AM material is subjected to different solidification protocols than traditionally cast or wrought material. This introduces a need to understand and manage the property ranges for materials considered for final part manufacturing [6]. The stainless steel specimens used in this study are made via DMLS on an EOS GmbH M280 DMLS. The parts are patterned off of a computer model design of a cylinder devolved into cross-sectional build layers. As each layer is sintered upon the last, the build plate moves and another thin layer of powder deposits. As subsequent layers are created, a complete part is typically formed in one build. Although the process may appear simple, there are complexities that make AM manufacturing techniques far different from the well investigated and standardized processes of forming and machining finished parts from the wrought stock material [15].

There are many DMLS inputs and process parameters, with a currently unquan-

tified influence on the AM part resulting from any changes to those parameters [6]. Modifying some parameters can induce desirable outcomes: less material waste, a faster build rate, better surface finish, or higher dimensional stability. However, the effect of each variation, as well as environmental conditions, must be understood so the product will attain the desired mechanical properties. Not only might the effects be seen in the microstructure, but also may result in lower density parts, layer delamination, or nonuniform shrinkage and the build-up of residual stresses, leading to curling or cracking of parts. Numerous researchers have also investigated residual stresses and distortion in these type of AM processes using analytical and finite element methods.

In addition to environmental parameters are difficult to control, there are several options on a DMLS machine can be manipulated to form production recipes. The factors to be considered are laser related, scan related, powder related, and temperature related [6]. Standard laser options for the continuous wave lasers typically used are spot size, pulse duration, and pulse frequency. The scan speed, scan spacing, and scan pattern can be changed to prevent undesirable residual stresses induced by the scanning. Melt pool size is highly dependent upon settings of laser power, scan speed, spot size and bed temperature. The powder can vary due to variations in initial stock and the practice of reusing powder from previous builds. However, the shape, size, and size distribution of the powder strongly influence laser absorption characteristics as well as powder bed density and powder spreading. The temperature may also be varied to influence the cooling rate or method of the AM part formation by adjusting the ambient temperature, heating the build plate, or varying the powder feeder temperature.

A characteristic pattern often observed in AM is the presence of layered beam traces, as seen in Figure 1, although the effect can be material and process dependent.

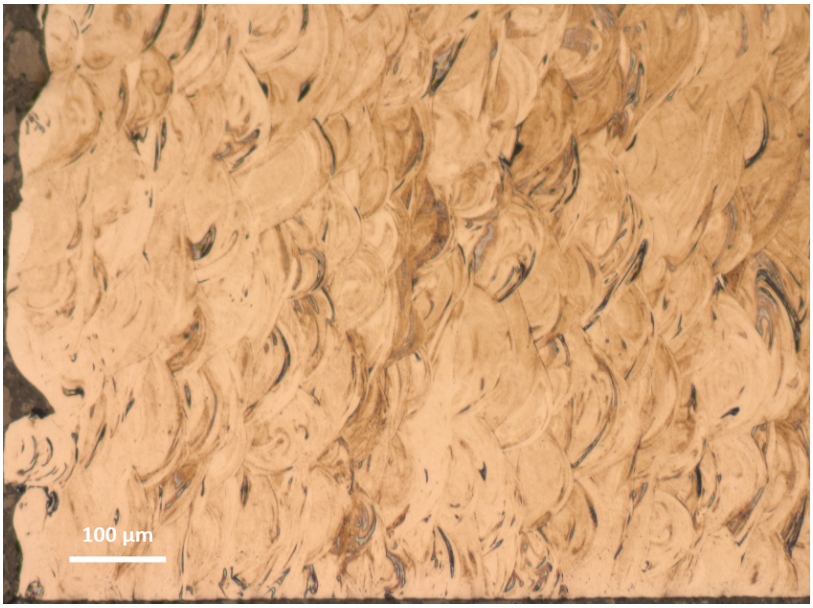

Figure 1. Example of beam trace and melt pool influence, optical microscope

For certain alloys it is not uncommon for contiguous grain growth across layers while for other materials, such as those that have a higher melting point, the layering may be more prevalent. In addition, layering is more likely for process parameter combinations of lower bed temperature, lower beam energy, faster scan rate, thicker layers, and/or larger scan spacing.

2.2 Material Properties and Microstructure of 15-5 PH Stainless Steel

The focus material of this study is an AM PH stainless steel. The main distinction of PH stainless steels from other stainless steels is the aging treatment. Added elements, either aluminum, titanium, niobium, or copper increase strength by forming intermetallic compounds or precipitate matrices when properly aged via heating to a certain temperature range and holding for a prescribed period of time [16]. This capability, combined with a low carbon content, contribute to the comparatively high strength and toughness of the material.

The precipitation hardenable (PH) stainless steels were first developed in the

1940's out of the need for high-strength, corrosion-resistant materials of reasonable cost that retain considerable strength up to moderately elevated temperatures [17]. The formation of 15-5PH through traditional methods evolved over the years to produce purer, cleaner steels with more carefully controlled compositions and better material properties than earlier techniques [16]. 15-5PH is in a family of PH stainless steels containing 12 to 18% Cr, 0.15 to 1.25% C, Ni, Si, Mn, and other elements [18]. The material's particular composition is specified in the AISI S15500 standard and can be found in table 1 [16]. The PH steel type or classification is related to the crystallographic matrix. 15-5PH is designated as martensitic, with a body-centered tetragonal crystal matrix that is formed upon cooling from the annealing temperature, where it is an almost completely austenite, face centered (FCC) crystal structure [17]. These atom arrangements are displayed in Figure 2 [15]. Some of the PH steels may have small amounts of weaker, less tough body centered cubic (BCC) delta ferrite present at the annealing temperature, but it is generally undesirable [18].

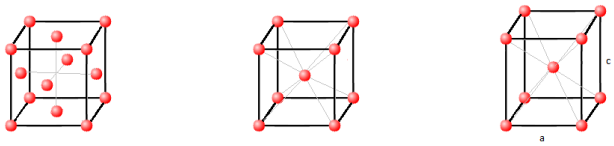

(a) FCC Crystalline Unit Structure (b) BCC Crystalline Unit Structure (c) BCT Crystalline Unit Structure

Figure 2. Comparison of the Crystalline Structures of a) Austenite, b) Ferrite, and c) Martensite. Adapted from Kalpakjian (1995)

There are two hardening mechanisms for martensitic PH material, one is the transformation of the FCC austenite to BCT martensite upon cooling from the annealing temperature [17]. The martensitic structure is depicted in Figure 3. The annealing temperature for a PH material is carefully selected to provide the optimal austenite composition for the subsequent transformations that will harden the material [18].

15-5PH has a specified annealing temperature of 1900°F, using temperatures lower or higher than the annealing temperature has repurcussions on the microstructure. Using lower temperatures tend to result in a softer martensite that is lower in carbon content. Higher temperatures produce cooled structures with high amounts of retained austenite and the possible formation of delta ferrite. The retained austenite will produce a high ultimate strength but lower yield strength and the delta ferrite will cause low ductility and poor impact performance [18].

If the proper annealing temperature is used, the 15-5PH should be almost fully martensite, with perhaps some retained austenite but no delta ferrite. However, previous research on AM 17-4PH, a material very similar to 15-5PH, found the AM process conditions can produce a structure with a structure composed of nearly 50% FCC retained austenite, which could significantly inhibit the precipitation reaction [19]. The martensite start M_s and martensite finish M_f temperatures are key to understanding how a material is transformed completely to martensite or retains some austenite [16]. They are the temperatures at which, upon cooling from an elevated temperature, the martensitic transformation from an austenitic structure begins.

With the exception of cobalt and aluminum, the elements added to a stainless steel tend to lower the martensitic range of the steel [16]. Therefore, as the alloy content increases, the $(M_s) - (M_f)$ range shifts. Alloying at levels above approximately 12% Cr serves to delay ferrite formation and reduces the (M_s) temperature. Although decreasing the nickel content can often decrease corrosion resistance, molybdenum can be added and, along with copper and a relatively high chromium content, result in giving the PH grades a moderate-to-good corrosion resistance [16]. When higher chromium levels are used to improve corrosion resistance, nickel can help maintain the desired microstructure and prevent excessive free ferrite.

2.3 Heat Treatment of 15-5PH Stainless Steel

The other hardening mechanism is the formation of interstitial precipitates upon a later heat treatment, or aging, process [17]. Heating the material to a moderate temperature allows for atom migration to occur. In the case of 15-5PH, the Cu alloy in the material forms a microscopic intermetallic compound along the crystallographic planes of the matrix material [18]. The difference in lattice dimensions between the precipitate compound and the matrix cause the matrix to become severely strained, strengthening the material. The heat treatment temperature range is 480 to 620 °C (900 to 1150 °F) [16]. Maximum strengthening for this alloy is attained by aging it at 850 to 900 °F, this is referred to as being "fully aged". At this condition, the copper precipitate is so fine it can only be detected with a high powered electron microscope. The precipitate particles are small and uniformly distributed at this stage. As the temperature is increased, the precipitate particles grow larger and are less effective at strengthening. At temperatures high in the precipitation range, where the material is considered "overaged", shearing takes place between the precipitate and matrix. The shearing relieves the strain, decreasing the strength [18].

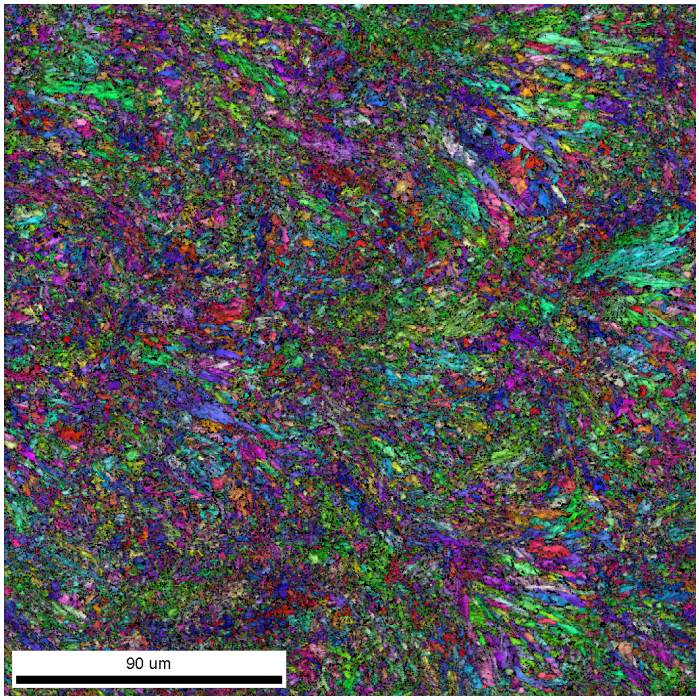

Figure 3. Martensite grain structure of non-heat treated AM 15-5PH)

2.4 Differences Between Wrought and AM Stainless Steel

The many processing parameters available in AM and ability to produce complex parts from raw materials makes it both more flexible than the traditional forming methods and more complicated to determine the final material properties. Traditional wrought iron is usually shipped from the manufacturer in standard shapes [3]. The material in these forms has been annealed and homogenized to refine the grain shapes and sizes and avoid residual stresses and internal cracking [18]. The manufacturer delivers the material in this condition, referred to as condition A, to the customer. The customer then machines the alloy into the final manufactured shape and applies a precipitation hardening heat treatment tailored to obtain the desired material properties for the application [17]. The properties of the standard condition A material and the effect of the heat treatment upon the material are well characterized and the material characteristics of the final net shape can be predicted.

Conversely, the mechanisms to standardize and characterize the final properties of material made via AM are not established.

2.5 SHB Test

A SHB, or Kolsky bar, is the most widely used characterization tool for the mechanical response of materials deformed at high strain rates (10^2 to $10^4 s^{-1}$) [20]. It is named in memory of John Hopkinson and his son, Bertram who both designed apparatus to measure impact stress wave propagation through a material in the late 1800's. Kolsky, in 1949, extended the technique to measure stress-strain response of materials under impact loading conditions. Today's SHB consists of two elastic bars with a specimen between, a striker to deliver a controlled impact, and strain gauges to measure the effect by analyzing the stress wave propagation through the test apparatus and the material. With slight variations in setup, the SHB can perform compression or tension tests. Impact velocity, bar material, and specimen size are variables to achieve different strain rates. The setup and methods of obtaining dynamic stress-strain graphs are discussed in Chapter 3.

III Methodology

This chapter describes the methods used to perform the study and is broken into five sections. The first section details how the samples and specimens were produced, followed by a section describing how the representative samples were prepared and examined to use as a microstructure baseline. The third section shows how the samples were prepared and tested for the quasi-static tests. The fourth section describes the process of running the dynamic tests upon two different SHB, followed by the fifth section presenting the method of preparing those measurements for comparison.

3.1 Representative Material

3.1.1 DMLS Sample Manufacturing

The first objective of this research is to accurately represent the AM material by obtaining prototypical samples of the material itself to test. Although this sounds relatively simple, the flexibility of AM and the many processing parameters available requires consideration before manufacturing begins. To get the proper material properties, it is essential to decide which variations are wanted, eliminate areas which might suffer from incomplete processing, and replicate processing parameters as precisely as possible.

The parameters of each DMLS build are based upon the recommended procedure by the manufacturer [2]. The powder used is a pre-alloyed stainless steel known as EOS Stainless Steel PH1 in fine powder form supplied by a third party vendor. The chemistry of EOS Stainless Steel PH1 conforms to the compositions of DIN 1.4540 and UNS S15500. Each powder batch is checked and verified by the vendor before sending to the AM manufacturer. Standard processing parameters on an EOSINT M280 use a 200 or 400 W laser and an inert N_2 environment. The standard processing

parameters are intended to attain a density matching the standard 15-5PH with full melting of the entire geometry and a minimum recommended layer thickness of 20 μm. If faster build speed is necessary, 40 μm layer thickness is suggested to meet the same density requirement. This test did not attempt to test the properties of the material made with thicker layers. The manufacturer asserts the parts made from this powder bear further processing and machining from the "as built" condition, which in this research will be likened to condition A of a wrought material.

This study relies upon five separate orders of material. Four of the five included unexposed powder reused from previous builds for cost effectiveness. The cylindrical dog bone shaped specimens pictured in Figure 4 necessary for the tensile and SHB tests were manufactured as 2 in. long, 0.5 in. diameter cylinders and machined into final shape prior to heat treatment. This was done in an attempt to attain uniform properties throughout with as little impact from edge effects, geometric instabilities, surface roughness, or warping due to residual stresses. This also ensures the samples fit consistently in the test apparatus. Because of the variance in composition, one set of small cylinders used for the SHB compression tests was machined from excess material and one was manufactured in net shape.

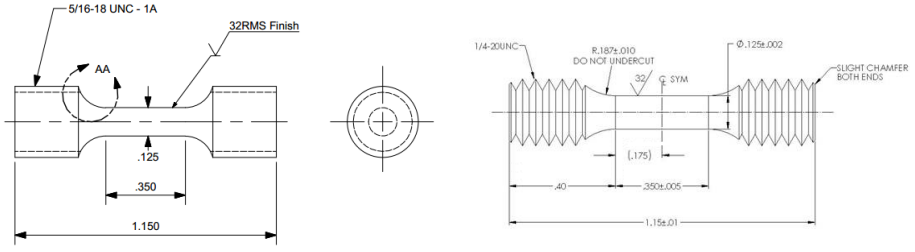

(a) SHB Indirect Tension Sample (b) SHB Direct Tension Sample

Figure 4. Examples of Tension SHB samples used in this research

3.1.2 Build Orientation

It is of interest in this research to determine whether the build orientation results in anisotropy under dynamic loading [6]. To examine this, specimens are built in two directly opposing conditions: layers oriented perpendicular to and in the load direction as shown in Figure 5. A cylinder built of circular layers sintered on top of each other, termed in this paper a "vertical" orientation, results in a very well defined cylinder. Intuitively, this would appear an ideal orientation for such a part. However, many parts will have complex features on multiple axes and thus must bear forces in ways inconsistent with a single test axis. Therefore, this test also includes a "horizontal" build direction, where the cylinder is built on its side and made of varying sizes of rectangular cross-sections. One of the horizontal builds was not well supported during the build, and experienced residual stresses and considerable, visible, warping.

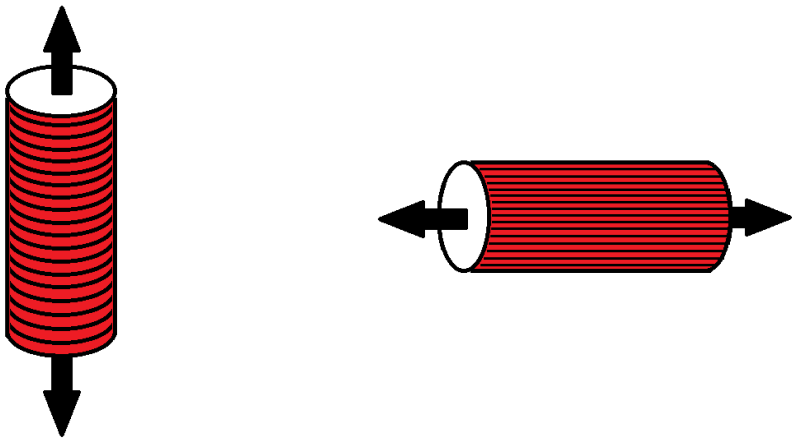

(a) Vertical Build Direction (b) Horizontal Build Orientation

Figure 5. Build Orientations

3.1.3 Heat Treatment

15-5PH is not recommended for service in Condition A, instead this material is typically heat treated in a number of standard protocols. Maximum tensile strength properties are obtained by using the H900 heat treatment protocol, which can be found in table 8 in appendix A [18, 21]. Higher ductility and toughness values at lower strengths are anticipated by overaging the material by heating it a longer time at temperatures ranging from 925 to 1150°F. The two protocols used for the test samples are heat treated to H900 and H1025. H1025 is recommended over H900 when good fracture toughness or impact properties are required as it provides a lower transition temperature and more useful levels of fracture toughness [3].

3.2 Microscopy Sample Preparation

The microstructure of the material cannot be easily examined without damaging the test specimen, so samples prepared from the same build are used instead of damaging the test specimens. These are cut from the AM cylinders as shown in Figure 6. Using this configuration produces a rectangular cross section and a circular or semicircular section of each build, build orientation, and heat treatment protocol. These are mounted in a conductive phenolic compound compressed into 1.25 in. diameter circular pucks and are planarized and polished for examination.

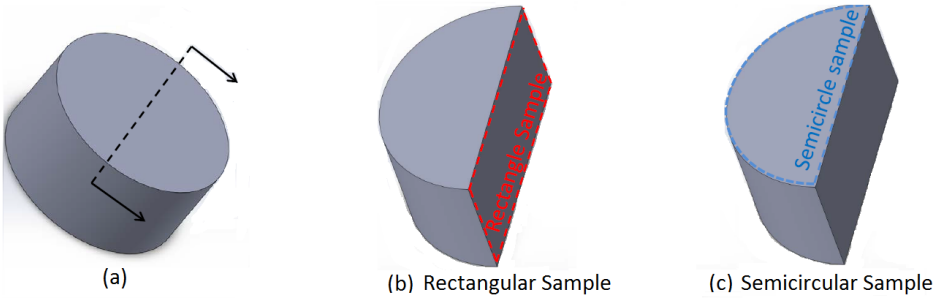

Figure 6. Example of sectioning for microstructure study

Taking care with the polishing steps should avoid deformation and scratching. In this case, a Struers automatic polisher with the ability to polish up to 10 specimens at one time was used for both grinding and final polishing. Fine grinding is accomplished using a polycrystalline diamond suspension on a rigid disc, then a finer diamond suspension a soft cloth disk. The final polish uses colloidal silica on a silk pad to remove fine scratches.

3.3 Tools for Examining Microstructure

3.3.1 Energy Dispersive X-ray Spectroscopy (EDS)

EDS is a technique using energy detected from x-rays emitted from a sample during electron imaging to estimate the composition of a material [22]. The sample is loaded and rotated to cause the electrons accelerated from the SEM column to be incident to it, interactions of the electrons with the atoms in the sample cause the transfer of kinetic energy. The collisions within this interaction eject some inner level electrons (low energy). Each ejected electron is replaced by an electron from a higher energy shell. The energy lost as the electron moves from the high energy shell to the low energy shell is released in the form of x-rays. During this transition the electrons give off energy in the form of photons. These x-rays are analyzed either by wavelength dispersive methods or energy dispersive methods to determine the type of atoms present.

The system consists of three main components installed in conjunction with a SEM: an x-ray detector, pulse processing circuitry, and analyzer equipment [23]. After emission from the sample, each x-ray photon creates a charge pulse in the detector. The pulse processing circuitry converts the charge pulse into a voltage pulse whose amplitude reflects the energy level of the detected x-ray. The energy level of the radiation is converted into a digital signal, adding one count to the corresponding

voltage channel of a multichannel analyzer.

What makes EDS particularly useful is the direct relationship these counts bear to the concentration of the elements (mass or atomic fraction) [23]. Even though each element has many energy levels and therefore many potential vacancy-filling mechanisms, each element emits a different pattern of x-rays. Therefore, it is possible to convert the x-ray measurements into a final spectrum like in Figure 7. Sometimes a single element is represented by multiple peaks, which can be added to get an approximate assessment of concentrations of the various elements present.

The breadth of each peak in Figure 7 indicates the imprecision resulting from measurement of the energy of an individual x-ray [22]. The amount of charge the x-ray generates in the detector is vulnerable to systemic and random error resulting in signal and background noise. To understand the results, it is vital to know the minimum concentration of a particular element capable of detection by the system. Transition metals such as chromium, iron, copper and nickel are easily detected even at extremely low concentrations. The low energy x-rays produced by carbon, nitrogen and oxygen atoms generate much lower count rates, making it difficult to detect these atoms at low concentrations. The general rule to get good peak resolution is to use accelerating voltage of at least two times the highest peak energy expected, 20kV here.

3.3.2 Electron Backscatter Diffraction (EBSD)

EBSD also uses the beam of a scanning electron microscope (SEM) to collect crystallographic information about the microstructure of a material [24]. In the technique, a sample of the material is tilted at a 70° angle from horizontal and a detector is used to obtain patterns diffracted from interaction of the beam with a point of interest on the sample. These patterns form when a small fraction of the atoms of

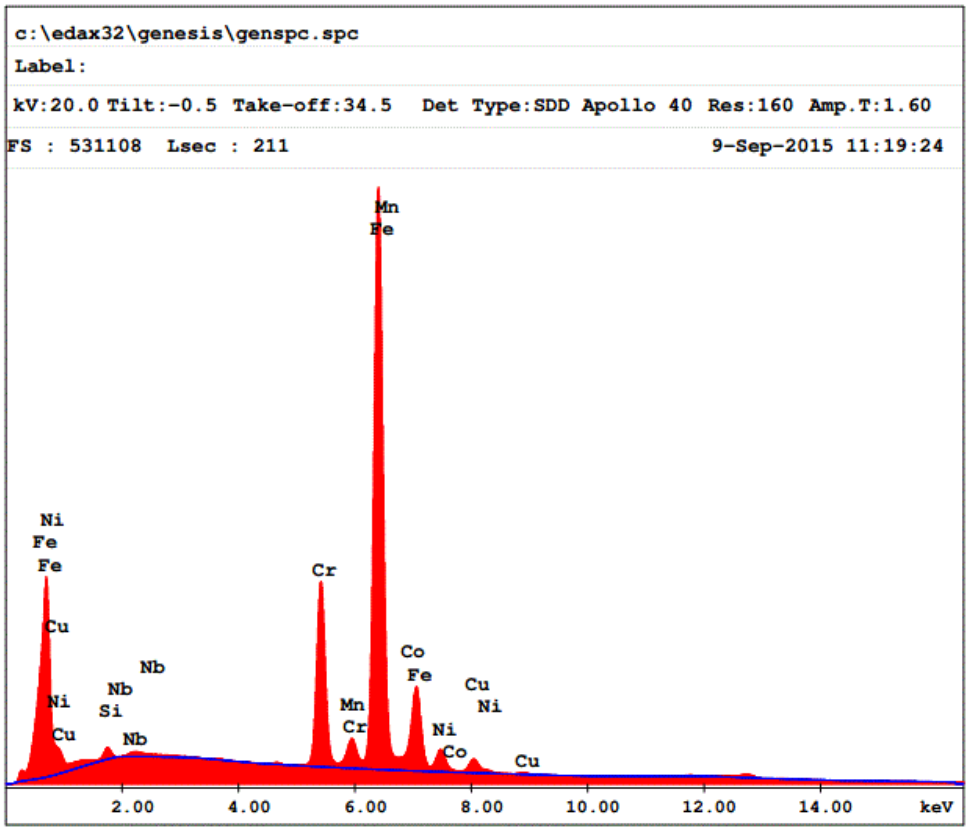

EDAX ZAF Quantification (Standardless)
Element Normalized
SEC Table : Default

Element	Wt %	At %	K-Ratio	Z	A	F
SiK	0.67	1.31	0.0032	1.1163	0.4251	1.0014
NbL	0.55	0.33	0.0037	0.9104	0.7380	1.0010
CrK	13.94	14.86	0.1623	0.9984	0.9877	1.1808
MnK	0.73	0.74	0.0072	0.9812	0.9947	1.0139
FeK	73.44	72.94	0.7229	1.0006	0.9749	1.0090
CoK	2.59	2.44	0.0251	0.9814	0.9818	1.0048
NiK	4.51	4.26	0.0411	1.0180	0.8951	1.0000
CuK	3.57	3.12	0.0317	0.9707	0.9138	1.0000
Total	100.00	100.00				

Figure 7. EDS spectrum for Build 3 material

the beam are inelastically scattered by the atoms of the material to form a divergent source of electrons close to the surface of the sample. Those electrons incident on atomic planes satisfying the Bragg equation form a paired set of cones corresponding to each diffracting plane. The regions of enhanced intensity at the point where the cones intersect the screen project a pattern on the screen called Kikuchi bands. The

areas of highest intensity are used for pattern recognition and indexing and translated by use of the Hough transform. The diffraction pattern collected is characteristic of the crystal structure and orientation of the material. The software turns these patterns into detailed maps of the grain morphology, orientations, and boundaries of the sample region of interaction.

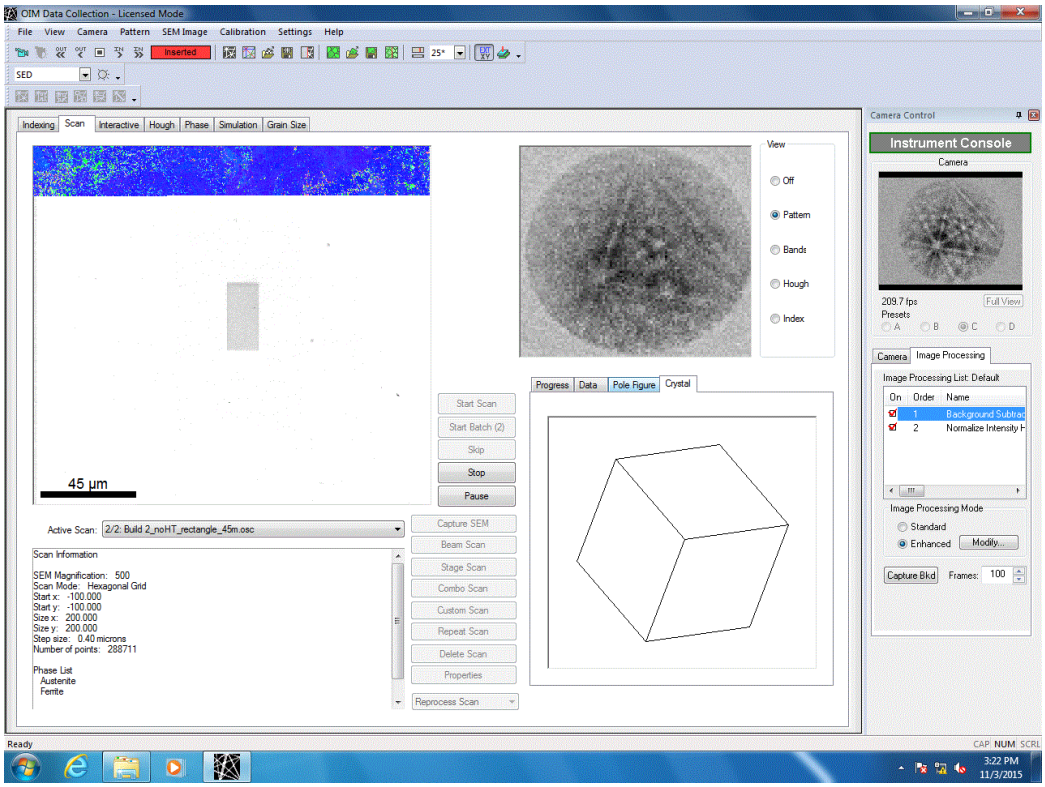

Figure 8. Screenshot of EBSD

This technique is not perfect, however. It is difficult for EBSD to distinguish phases with similar crystal structures because it generally uses only the angles between the bands to identify the phase [24]. In this case, this means it is difficult for the technique to tell the difference between the body-centered tetragonal (BCT) martensite and the body-centered cubic (BCC) ferrite because the b to a ratio for this BCT structure is very close to unity. For ease of comparison, in the EBSD scans used for this research only the ferrite is selected to classify both and the resultant

grain morphology map is used to determine which phase is present by visual recognition. There also are areas with poor pattern quality, overlapping patterns, poor band detection, or various other issues. Post-processing of each image can often help smooth some of the inconsistencies, these methods are applied to the EBSD results in Chapter 4.

3.4 Split Hopkinson Bar (SHB)

The SHB test apparatus consists mainly of two long, slender elastic bars [20]. The bars are mounted, aligned, and rigidly supported in the horizontal direction by bearings. A test specimen is positioned between these bars. A striker bar is launched in a repeatable manner and guided down the apparatus to strike the end of the incident bar [25]. The strain conditions and reactions are determined by measuring the reflected and transmitted waves through the bars.

In a SHB compression test, shown in Figure 9, a 5.08 mm (0.2 in.) right cylinder specimen is positioned between the bars [20]. The incident bar is loaded by external dynamic loading by launching a striker bar to impact the incident bar. The impact generates a compressive stress wave propagating towards the specimen sandwiched between the incident and transmitter bars. When the wave reaches the specimen, part of it reflects back and the rest travels into the specimen and reflects back and forth inside the specimen, compressing the specimen. Readings from the strain gauges and knowledge of the bar and striker enable assembly of stress-strain graphs as discussed in the next section.

A slight change in setup enables the same SHB to apply a tension wave via what is known as compression wave reflection. The compression wave reflection SHB setup is pictured in Figure 10. A slightly more refined version applies the tensile wave more directly and utilizes a method to trap the momentum. It is shown in Figure 11. The

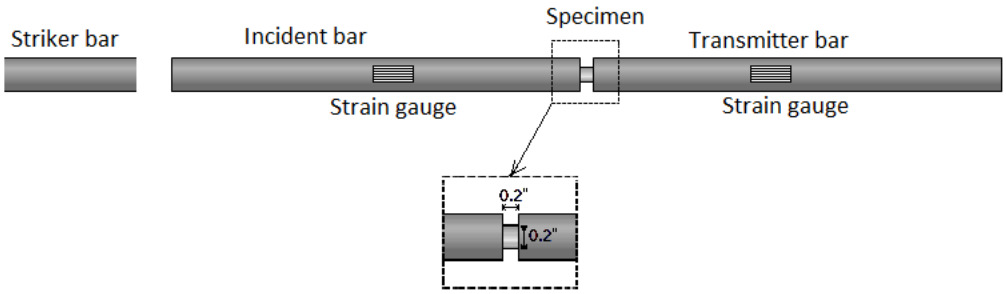

Figure 9. Split Hopkinson Pressure Bar: compression configuration

change in direction and addition of a transfer flange and momentum trap is designed to subject the test specimen to only a single tensile pulse. Both methods were used, the results are presented in Chapter 4. The specimens used to conduct the tests, specified in Figure 4 are virtually identical except for the threading specification.

The reflection wave test uses a compression bar modified as illustrated in Figure 9 [20]. The main change from the compression setup is the rigid collar placed over the specimen. Upon striker impact, the compression wave travels through the incident bar, passes through the collar and transfers into the transmission bar. The specimen is spared most of this initial compression wave due to the geometry of the collar. At the free end of the transmission bar, the compression wave is reflected back as a tensile wave. When this wave arrives at the specimen, the rigid collar cannot support the tensile wave and the specimen is subjected to the tensile pulse.

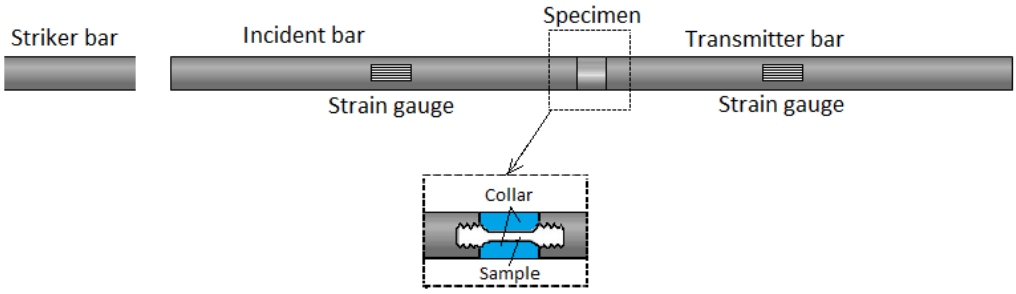

Figure 10. SHB Reflected Wave Tension Test Setup

In the direct tension SHB test used, a tubular striker is driven by a gas gun. This

tube slides on the incident bar until it impacts a hard stop at the end of the incident bar. A tensile pulse generated by the gas gun in the incident bar propagates to the specimen, subjecting it directly to tension. The momentum trap has a transfer flange on the incident bar. As it impacts the stop, the tensile pulse is reflected back at the incident bar/specimen interface, becoming compression. The compressive pulse directly transmits into the momentum trap bar, and is reflected back at the far end as a tensile pulse. The interface with the transfer flange does not support tension, so the pulse is trapped within the momentum trap bar. Therefore, the specimen is affected by only the first tensile loading and not subjected to reverberation [20]. Because of this distinct benefit, direct measurement of the actual cross-sectional area is used in chapter 4 as a representation for the final cross-section subjected to the single, tensile pulse.

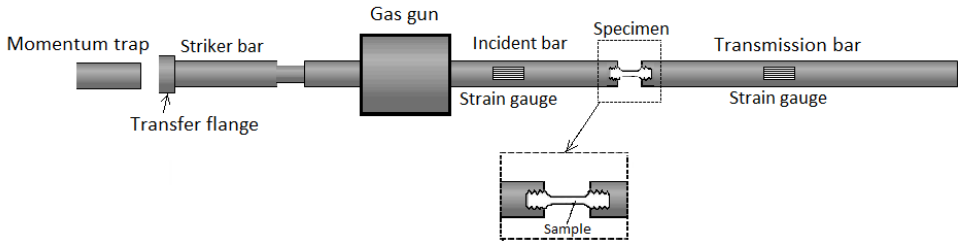

Figure 11. SHB Momentum Trap Tension Test Setup

3.4.1 SHB Results Analysis

The principal result from a SHB test is a graph of engineering stress versus engineering strain for the entire test. Comparing two or more tests at differing rates should give an indication of the strain rate sensitivity of the material. Multiple curves, often conducted at varying material temperatures, are used to derive a model for the dynamic behavior of a material. These are particularly useful for finite element

modeling software and for understanding creep effects. Gaining representative stress-strain curves from the SHB test relies upon a knowledge of how the wave propagating through the SHB rig and test specimen relates to the strain it is undergoing.

Each strike of the striker bar generates a stress pulse in the incident bar, this pulse travels through the bar until it is affected by contacting the sample. The amplitude of the incident wave and those reflected from and transmitted through the specimen are recorded by strain gauges positioned on either side of the specimen location. Strain rate is directly related to incident pulse and the velocity of the striker bar. The striker bar length and material characteristics also play a large role in the resulting strain and pulse affecting the incident bar. These strain gauge readings and the known parameters of the test apparatus are used to calculate the resulting nominal, or engineering stress (σ), engineering strain (ϵ), and strain rate ($\dot{\epsilon}$) at each sampled time.

The calculations require some simplifying assumptions to translate the readings into measurements of stress and strain. It is presumed the stress distribution is uniaxial and uniform along the specimen, the length of the specimen is very short if compared with the length of the waves, and friction and inertia effects are negligible [26]. It is assumed the specimen is stress equilibrated and deforms nearly uniformly, making equations 1 and 2 adequate representations of the average engineering stress and engineering strain in the specimen [27].

$$\epsilon_{eng} = \frac{C_{bar}}{L_{striker}} \int_0^t (\epsilon_{incident} - \epsilon_{reflected} - \epsilon_{transmitted})\, dt \tag{1}$$

$$\sigma_{eng} = \frac{A_{bar}}{A_{striker}} E_{bar} \epsilon_{transmitted} \tag{2}$$

$$\dot{\epsilon}(t) = \frac{2 * C_{bar}}{L_{specimen}} \epsilon_{reflected}(t) \tag{3}$$

In these equations, C_{bar} is the elastic wave speed of the bar and E_{bar} is the Young's modulus. C_{bar} is found using equation 4 and knowledge of the density of the bar (ρ_{bar}) [20].

$$C_{bar} = \sqrt{\frac{E_{bar}}{\rho_{bar}}} \tag{4}$$

The force applied (P) per unit of cross-sectional area becomes a stress. When expressed in reference to the undeformed configuration of the sample A_o, it is called engineering stress and is shown in equation 5.

$$\sigma_{eng} = \frac{P}{A_o} \tag{5}$$

The corresponding engineering strain involves finding the incremental change in length over the original gage length (L_o) corresponding to a certain measurement in time in equation 6.

$$\epsilon_{eng} = \left(\frac{\Delta L_i}{L_o} \right) \tag{6}$$

However, most materials exhibit some amount of deformation, reducing the cross sectional area. To get the true picture of the material response, the engineering stress and strain is translated into true stress and true strain. Uniaxial true stress (σ_{true}), is defined in equation 7 as the force over the instantaneous cross sectional area (A_i). It can be related to engineering stress quite simply as in equation 8.

$$\sigma_{true} = \frac{P}{A_i} \tag{7}$$

$$\sigma_{true} = \sigma_{eng}\left(\frac{A_o}{A_i}\right) \tag{8}$$

To get a true stress-strain curve approximating the actual measurement values over the course of the test, equation 9 is used to add the change in length over small increments. The instantaneous measurements are taken incrementally, or techniques such as high speed cameras or digital image correlation continuously capture the changing dimensions.

$$\epsilon_{true} = \frac{\Delta L_1}{L_1} + \frac{\Delta L_2}{L_2} + \frac{\Delta L_3}{L_3} + ... = \sum \frac{\Delta L_j}{L_j} \tag{9}$$

Assuming the ΔL is infinitesimal, the summation is equivalent to an integral. If L_{final} is assumed to equal $L_i + \Delta L$, equation 10 relates true strain to engineering strain.

$$\int_{L_o}^{L_{final}} \left(\frac{dL}{L}\right) = ln\left(\frac{L_{final}}{L_i}\right) = ln\left(\frac{L_i + \Delta L}{L_i}\right) = ln\left(1 + \frac{\Delta L}{L_i}\right) = ln(1 + \epsilon_{eng}) \tag{10}$$

In this experiment, incremental measurements were not feasible due to the strain rates used. The continuous measurement setup was also not practical due to the small size of the compression samples and the enclosure of the indirect tension specimens in a metal collar while testing. Therefore, true stress and true strain are found by estimation.

It is reasonable to assume the volume of the specimen is constant, or $A_i L_i = AL$ [27]. Therefore, equation 11 is applicable. Substituting the value returned from equation 11 into equations 1 and 2 yields equation 12.

$$\frac{A_i}{A} = \frac{L - i}{L_o} = \frac{L_o + \Delta L}{L_o} = 1 + \epsilon_{eng} \tag{11}$$

$$\sigma_{true} = \frac{P}{A_i} = \sigma_{eng}\left(\frac{A_o}{A_i}\right) \tag{12}$$

The simple equations in 10 and 12 are adequate for brittle materials, and for the region of more ductile materials where necking is not yet present [28]. These equations are no longer reliable after the cross-sectional area begins to shrink in the necking process of failure [27]. The 15-5PH stainless steel is expected to exhibit necking. However, as previously mentioned, there is no way to make incremental cross-sectional area measurements. Therefore, an approximation method is desired to arrive at a more representative true stress and strain curve.

The approximation method used utilized knowledge of the engineering strain at fracture and physical measurement of the final cross-sectional area of the broken specimen. This area used equations 7 and 9 to calculate a final true stress. Necking is expected to occur after ultimate tensile stress (UTS) is reached and the stress-strain curve begins to decline. Therefore, after the engineering UTS is reached, the material behavior is approximated as a linear trend to the fracture values found, with the Bridgman correction for necking applied to the final value [27]. Physical measurements of the diameter of the smallest point of the neck of each broken specimen enabled calculation of the final cross-sectional area. Although this is not as revealing as continuous measurement methods, it is expected to give an idea of the overall trend.

Even the simple methodology described will tend to overestimate the uniaxial true stress and true strain the specimen experienced. As the specimen undergoes necking, it is no longer subjected to only uniaxial stress, but is also subjected to a significant tensile hoop stress around the circumference in the necked region [29]. The additional hoop stress serves to increase the axial stress above the accounted for uniaxial stress [27]. The Bridgman correction factor in equation 13 is regularly used

to account for the additional hoop stress [29].

$$\sigma_{true} = \frac{\sigma_{axial}}{\left(1 + \frac{2R}{a}\right) \ln\left(1 + \frac{a}{2R}\right)} \tag{13}$$

The Bridgman factor is also a geometry-based measurement, and since there is no instantaneous measurement method there is no way to determine the instantaneous radius at the neck, a, or the corresponding radius of curvature at the neck, R. However, a Bridgman approximation function based upon incremental measurements and experimental data for steels is used. [27].

$$B = 0.0684x^3 + 0.0461x^2 - 0.205x + 0.825 \tag{14}$$

In equation 14 $x = log_{10}(\epsilon_{true})$. Equation 14 is valid for strain values $0.12 \leq \epsilon_{true} \leq 3$. Correction is not required for strains below 0.12. Multiplying the σ_{true} found from equation 7 by the B value in equation 14 creates a σ_B, a new true σ corrected to allow an axial curve to represent the overall response of the 3D hoop stress effect. This correction factor is applied to the SHB tension test results to obtain σ_{true} and ϵ_{true} values discussed in Chapter 4.

$$\sigma_B = B(\sigma_{true}) \tag{15}$$

IV Results

The objective of the research was to determine the dynamic properties of an AM stainless steel formed using pre-alloyed powder matching the specifications of 15-5PH. To obtain enough samples for a full test battery, five different builds were manufactured. Effort was made to keep all the builds manufactured under similar conditions to have assurance each accurately represents AM 15-5PH material. Each build uses identical settings on the same machine with the same type of powder. All but the first build, denoted build 1, are printed into cylinders with the same dimensional specifications: 12.7 mm (0.5 in.) diameter and 50.8 mm (2 in.) long. The planned variable is build orientation, the cylinders were manufactured in either a vertical, with a circular cross-section, or horizontal, with a variable rectangular cross-section. After manufacture, samples of the builds were machined into test specimens to undergo the scans and tests introduced in chapter 3.

Some variation was unavoidable. The builds were spaced over several months, with other production runs in between. Consequently, the input parameters were potentially different. As discussed in chapter 2, certain variance in material or process could have repercussions in material properties. Therefore, the material for the different builds are expected to operate within a performance range reflecting the processing parameters at the time each was built. Of additional interest is the material performance resulting from subjecting specimens manufactured in two opposing build orientations to H900 and H1025 heat treatment protocols. The results are presented in this chapter. Section 1 is an overview of the 5 builds, and sections 2 through 6 discuss the composition, microstructure and dynamic performance of each build.

4.1 Overview of 5 builds

EDS was used to gain a rough idea of the potential variation in the alloying composition between the builds. As presented in chapter 3, the results of EDS scans are semi-quantitative and may not reflect the precise composition of a material. The method has particular difficulty representing the lower atomic mass and trace elements, which could skew the percentage by weight calculation. However, EDS is used to produce a reasonable estimate of the relative amounts of alloys present. The resultant compositions, tabulated as percentage by weight, found for each of the builds using EDS are summarized in Table 1. Histograms of some of the scans of the builds are included in Appendix C.

The American Iron and Steel Institute (AISI) standard for 15-5PH, AISI S15500, is presented to the left side of the table [16]. The resulting EDS values for the AM builds studied are listed to the right. There is a noticeable trend; according to EDS, builds 1 and 2 do not conform to the standard. Builds 3, 4 and 5 do appear to fit within the parameters.

Review of the literature indicates the build environment could influence the microstructure [19]. Due to the EOS machine's ability to support both an Ar and N_2 inert gas environment, two samples were made after the final build, build 5, in each environment to test the compositional stability [2]. Obtaining very precise amounts by mass spectroscopy was desirable to validate not only whether the correct amounts of Cr and Ni are present, but also ensure there was no contamination. Additional elements unintentionally included may inhibit martensite formation upon cooling or promote or stabilize ferrite or austenite crystalline structures at room temperature. The results are presented in table 2 and compared to the AISI S15500 standard for 15-5PH stainless steel. Both samples match the specification, indicating the build environment itself is not the root cause of the compositional variation. This finding

Table 1. Approximate % weight of alloy composition from EDS results for 5 builds.

Alloying Elements	15-5 (AISI)	Build 1	Build 2	Build 3	Build 4	Build 5
C	0.07*	-	-	-	-	-
Mn	1	0.00	0.49	0.73	.51	.54
Si	1	0.47	0.48	0.67	0.63	0.76
Cr	14.00-15.50	9.40	9.06	13.94	14.35	14.29
Ni	3.50-5.50	9.50	9.01	4.51	4.27	4.16
Mo	0	1.79	1.93	0	0	0
Nb	0.15-0.45	0	0	0.55	0	0.37
Cu	2.50-4.50	2.68	2.50	3.57	3.46	3.45
Fe	71.9-77.7	72.18	70.44	73.44	75.34	75.12

*Note: EDS cannot semi-quantatively assess C

also lends credence to the supposition the last three builds are representative samples of AM 15-5PH stainless steel material.

When visually comparing the different builds, Figure 12 shows the visible differences in color of the scale formed due to heat treatment. Scale is often formed during the heat treatment process and is typically removed by strong acids, but removal was not necessary for this study[30]. The scale coloration was consistent within the builds and across heat treatments. The heat treated build 2 specimens portray the appearance of the non-heat treated steel but with a slight additional bluing. Builds 3 and 4 also have bluing but are more coppery in color. Build 5, manufactured from fresh powder after a thorough machine cleaning and examination, retains an overall

Table 2. Results of Mass Spectroscopy Evaluation for Ar and N Build Comparison

	AISI S15500	**Sample 1 (N_2)**	**Sample 2 (Ar)**
% Fe	71.9-77.7	77.1	77.3
% C	0.07	0.0279	0.0283
% Si	1	0.603	0.603
% Mn	1	0.0056	0.0032
% P	-	0.0025	0.0011
% S	-	0.0029	0.0029
% Cr	14.00-15.00	14.1	14
% Mo	-	<0.0005	<0.0005
% Ni	3.5-5.5	4.12	4.04
% Al	-	0.0028	0.0027
% Co	-	0.064	0.0635
% Cu	2.5-4.5	3.53	3.52
% Nb	0.15-0.45	0.338	0.339
% Ta	-	0.0539	0.0578

coppery color without a large amount of additional blue. The contrast between build 2 and the subsequent builds show the lack of coppery coloring may reflect its compositional variation. The extent of the blue tinge stayed relatively constant within each build, and is assumed to be associated with the manufacturing process and not the heat treatment process itself since build 4 and build 5 were heat treated concurrently using the same equipment.

A microstructural examination of the builds enables comparison and insight into how they might perform in the ensuing tests. At least one representative specimen

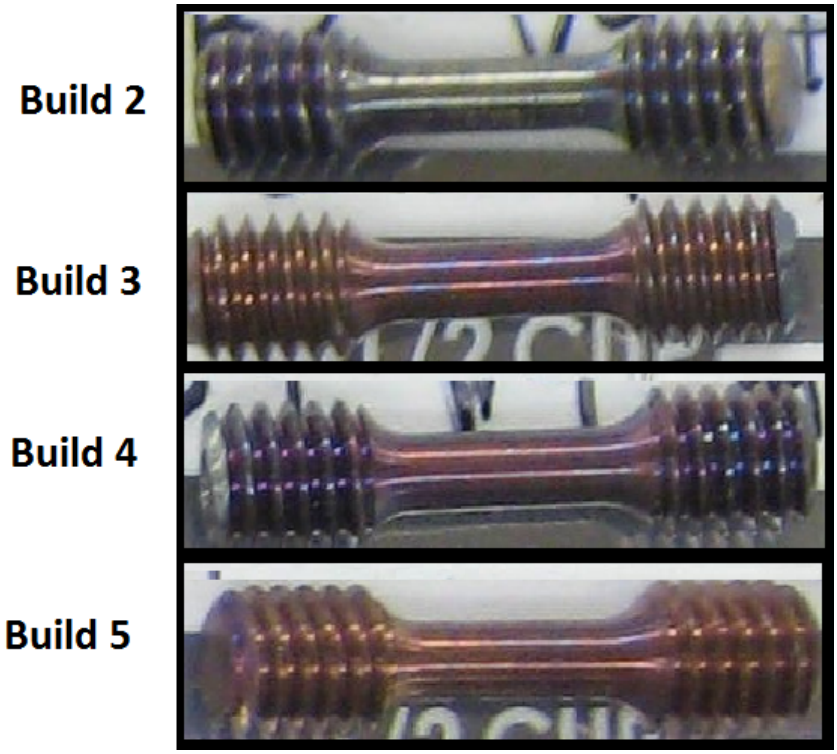

Figure 12. Variation in Surface Coloration by Build, Post H900 Heat Treatment.

was chosen from each to examine using EBSD. Each was subjected to a "large" area scan, approximately 210 μm by 210 μm. This scan is intended to convey a sense of the overall structure and is likely to cover several of the 20 μm powder layers. A spot near the center of the large area scan was chosen to start a smaller area scan, approximate 24 μm by 24 μm. An inverse pole figure, depicting grain shape and color coded to depict crystalline orientation, is included for each scan, along with a phase diagram. The color key to the inverse pole figure is in Figure 13. In the EBSD inverse pole figures presented, the grains colored blue are aligned with the <111> Miller indices, the points in red are <100> oriented and the points in green are <110>. The fluctuations in color within grains are indicative of texture. The phase map is color-coded green and red to show the types of constituents identified: green for austenite and red for martensite or delta ferrite. The small inverse pole scan reveals the morphology, or shapes, of the individual grains. The associated phase

maps may reveal differing percentages of identified structure due to the location, area covered, and focus level.

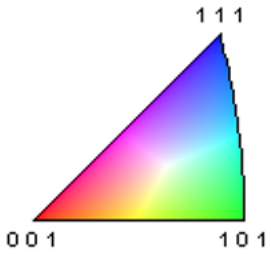

Figure 13. Inverse Pole Figure Crystal Orientation Key.

Build 1 has large martensite grains, and builds 3, 4, and especially 5 display much finer martensite grains. These four builds are overwhelmingly martensite, with only a small percentage of retained austenite, typically no more than 3%. Build 2 is quite different; this build has evident delta ferrite and a very high percentage, approximately 60%, of retained austenite. Builds 4 and 5, both manufactured in horizontal and vertical orientations, show distinct reflections of the AM process. The EBSD scans and microstructures are included and discussed more in-depth in the following sections.

4.1.1 Test Result Summary

Samples of each build were subjected to quasi-static and dynamic SHB tests. It is important to note that, due to an inability to create a larger quasi-static tension specimen uniquely within a build, all quasi-static specimens were made from the same 12.7 mm (0.5 in.) diameter and 50.8 mm (2 in.) long cylinders as the tension specimens. To reduce the variability and enable comparison, each specimen was machined to match the reflected wave SHB specimen specifications and tested using the same machine. Several types of dynamic testing were accomplished using the two SHB apparatus described in Chapter 3. The testing layout in Appendix B shows how

many of each build were subjected to testing using the compression, reflected wave tension or momentum trap tension SHB setup. Compression tests were conducted only at a single rate, $\approx 400\frac{1}{s}$, while each tension test was run for what is considered a mid-level strain rate of $\approx$400-500$\frac{1}{s}$ and a higher rate ranging $\approx$750-900$\frac{1}{s}$. Due to the limitations of the apparatus a rate truly considered high, in excess of $1000\frac{1}{s}$, could not be obtained.

The results of the tests for builds 1 and 2 are in table 3. These results are separated from the others because they are so compositionally different from the others. Build 1 was tested only in compression, on a different apparatus than build 3. Only 5 samples of the 11 tested yielded valid results, the 3 non-heat treated samples averaged a ultimate tensile strength (UTS) of 1465 MPa and a maximum strain (ϵ) of .098. The 2 build 2 H900 samples did increase in UTS to 1520 MPa with slightly less maximum ϵ of .095. Although this fits the expected trend of increased strength and decreased ductility with H900 heat treatment, these values are less than 3% and not considered significant.

Build 2 was tested at a quasi-static rate and in tension on both the reflected wave and momentum trap SHB apparatus. The results in Table 3 are remarkably consistent across the heat treatments for every test. This indicates little to no aging with heat treatment and is consistent with the large amount of retained austenite present in the microstructure of build 2. In addition, all of the quasi-static sample UTS are less than that reported for a condition A wrought material, 1110 MPa [1]. Although the values for the momentum trap SHB were 8%-12% higher than for the reflected wave SHB, there was not a significant strain rate dependency for either.

Build 3 was the most extensively tested of the builds. Table 4 contains the results for the quasi-static, compression SHB and both tension SHB tests conducted on build 3. A comparison of the UTS values with those of build 2 shows a distinct difference;

Table 3. Test Results for Builds 1 and 2

Build		Method	Strain Rate	Heat Treatment	UTS (MPa)	Max ϵ
1	Vertical	Compression	$500s^{-1}$	No HT	1463.57	0.098
				H900	1519.62	0.095
2	Vertical	Quasi-static	.001 s^{-1}	No HT	1078.30	0.333
				H900	1084.99	0.312
				H1025	1093.85	0.290
		Tension, Reflected Wave SHB	500 s^{-1}	No HT	1041.54	0.216
				H900	1050.36	0.225
				H1025	1033.27	0.221
			800 s^{-1}	No HT	1030.41	0.223
				H900	1042.54	0.216
				H1025	1025.71	0.216
		Tension, Momentum Trap SHB	$550s^{-1}$	No HT	1153.00	0.280
				H900	1142.00	0.273
				H1025	1144.00	0.283
			875 s^{-1}	No HT	1182.00	0.251
				H900	1158.00	0.220
				H1025	1152.00	0.249

build 3 UTS hardens with heat treatment. Not only does the UTS of the H900 and H1025 uniformly increase by ≈20% and ≈10% respectively from the non-heat treated material, but also all UTS and max ϵ exceed the wrought UTS and max ϵ expected [1]. In these tests, the UTS for the reflected wave tests tended to be on the order of ≈10% higher than those of the momentum trap tests. The loss of ductility is notable in the reduction of the max ϵ, on the order of 2%-5% loss from the non-heat

treated condition to H900 and 1%-3% to the H1025 for the tension tests.

Table 4. Test Results for Build 3

Build		Method	Strain Rate	Heat Treatment	UTS (MPa)	Max ϵ
3	Horizontal	Quasi-static	.001 s^{-1}	No HT	1240.43	0.221
				H900	1585.19	0.207
				H1025	1450.46	0.2574
		Compression	400 s^{-1}	No HT	1560.26	0.222
				H900	1884.62	0.105
				H1025	1722.98	0.158
		Tension, Reflected Wave SHB	450 s^{-1}	No HT	1219.77	0.224
				H900	1533.94	0.202
				H1025	1457.06	0.212
			750 s^{-1}	No HT	1286.29	0.232
				H900	1588.01	0.205
				H1025	1478.23	0.206
		Tension, Momentum Trap SHB	500 s^{-1}	No HT	1326.00	0.290
				H900	1644.00	0.252
				H1025	1492.00	0.259
			850 s^{-1}	No HT	1345.00	0.278
				H900	1607.00	0.229
				H1025	1464.00	0.225

Build 4, constructed in both the horizontal and vertical orientation, was only subjected to quasi-static and momentum trap tension SHB testing. Examination of the UTS and max ϵ of the results found in Table 5 shows that both orientations follow the age-hardening trend expected. The H900 UTS values are ≈25% higher than the

non-heat treated, and the H1025 are ≈15%, trading strength for a loss of ductility such that the max ϵ for the H900 and H1025 is typically on the order of 5%-10% lower than the non-heat treated.

Table 5. Test Results for Build 4 - Vertical and Horizontal Build Orientation

Build		Method	Strain Rate	Heat Treatment	UTS (MPa)	Max ϵ
4	Vertical	Quasi-static	.001 s^{-1}	No HT	1205.81	0.214
				H900	1529.26	0.171
				H1025	1490.41	0.182
		Tension, Momentum Trap SHB	500 s^{-1}	No HT	1360.00	0.222
				H900	1730.00	0.168
				H1025	1562.00	0.183
			850 s^{-1}	No HT	1352.00	0.201
				H900	1715.00	0.158
				H1025	1526.00	0.169
	Horizontal	Quasi-static	.001 s^{-1}	No HT	1218.25	0.253
				H900	1532.04	0.224
				H1025	1414.79	0.2525
		Tension, Momentum Trap SHB	450 s^{-1}	No HT	1340.00	0.245
				H900	1672.00	0.201
				H1025	1557.00	0.185
			800 s^{-1}	No HT	1377.00	0.272
				H900	1677.00	0.167
				H1025	1547.00	0.185

Build 5 is expected to exemplify the "ideal" AM condition for this material. The machine and supply lines were thoroughly inspected and cleaned before the cylin-

ders were made, and completely fresh powder was used. Encouragingly, the EDS composition measurements in Table 1 match the specifications exactly. Build 5 was also split evenly between horizontal and vertical orientations, therefore should be a good indicator of any build orientation bias. The results in Table 6 do not show a significant change in strength due to orientation, but the max ϵ values are markedly different. The horizontal orientation offers typically about 8% more elongation, much more in the higher rate for the non-heat treated condition. This matches with the results found in build 4, but is more pronounced in build 5.

Table 6. Test Results for Build 5 - Vertical and Horizontal Build Orientation

Build		Method	Strain Rate	Heat Treatment	UTS (MPa)	Max ϵ
5	Vertical	Tension,direct	475 s^{-1}	No HT	1367.00	0.213
				H900	1651.00	0.176
				H1025	1466.00	0.172
			700 s^{-1}	No HT	1376.00	0.198
				H900	1626.00	0.152
				H1025	1466.00	0.172
	Horizontal	Tension,direct	475 s^{-1}	No HT	1332.00	0.279
				H900	1655.00	0.230
				H1025	1466.00	0.249
			850 s^{-1}	No HT	1345.00	0.307
				H900	1650.00	0.217
				H1025	1497.00	0.210

4.1.2 Momentum Trap SHB Test

The direct SHB test using the SHB setup with the momentum trap is the primary test for the study as more of the builds could be incorporated. It was used to compare builds 2 and 3, and both orientations of builds 4 and 5. The experiment matrix is listed in Appendix B. Two strain rates were used to highlight strain rate sensitivity: a mid and high. Although the actual rate varied across the specimens, the mid rate averaged approximately 450-500 s^{-1} and the high between 800-900 s^{-1}. Each specimen broke after experiencing the tensile pulse, displaying variations of a cup and cone fracture surface indicating necking of a ductile material. A smaller circle showed the brittle fracture as the material gave way. The strain gauges collected the strain information during the test, and the information was used to generate engineering stress-strain curves in the method discussed in Chapter 3. After breaking, the final cross-sectional area was measured and used to derive the true stress-strain at fracture, which was then adjusted for hoop stress using the Bridgman correction. The true-stress strain curves utilize a simple linearization after the UTS is reached and plastic deformation is assumed to begin. At times, particularly at the lower strain rates, the curves show non-linear phenomena leading up to the UTS. The UTS is reached only after an initial yield point and subsequent drop in stress. The initial yield point indicates some localized plastic deformation after which the load starts to increase by strain hardening [31].

4.1.2.1 No Heat Treatment

All of the dynamic test true stress-strain graphs portrayed downward sloping curves. This is sharply different than what is expected from quasi-static tensile tests, where the material is able to slip and strain harden at the low strain rates used. Instead, under higher strain rates all the samples undergo slight to significant strain

softening. The results of the non-heat treated samples are shown in Figures 14 and 15. The non-heat treated samples show the most ductile response, elongating the most at the higher rates. The higher rates have gentler slopes and ultimately fracture at slightly higher stresses than the mid strain rate. The trend of fracturing at higher stress and greater elongation seems counterintuitive at first, but

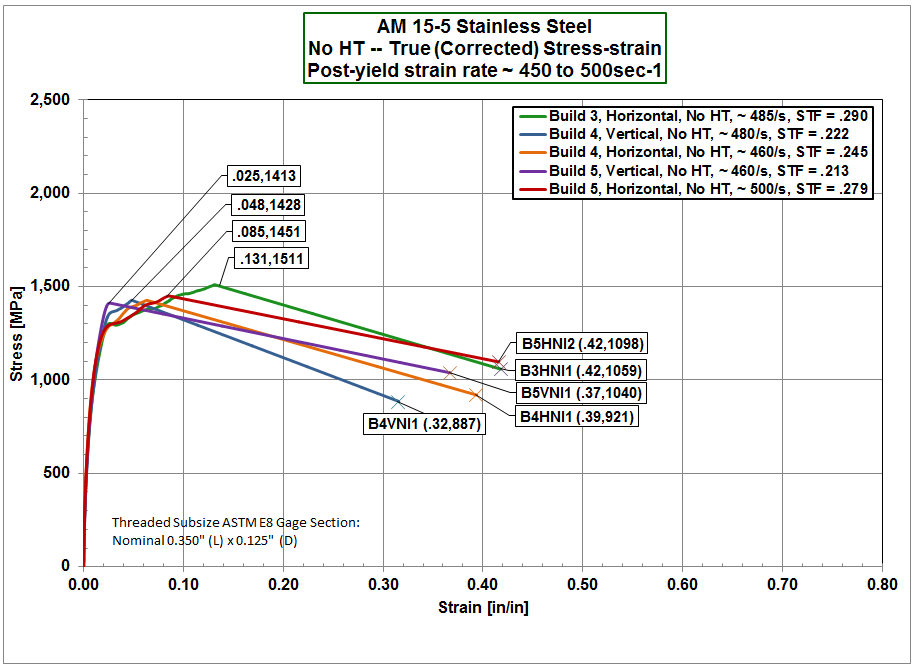

Figure 14. Non Heat Treated Samples, Horizontal Orientation, Direct Tension SHB Test, Mid Rate $\approx 450s^{-1}$ True Stress-Strain

4.1.2.2 H900 Heat Treatment

The results of testing the specimens heat treated to the H900 protocol are shown in Figures 16 and 17. Each of the builds displayed responded to heat treatment, showing stronger but less ductile behavior than the same tests on the non-heat treated specimens. Once again, the more gentle slope behavior is observed in Figure 17 at very similar fracture stresses. The true stress-strain graphs do not yet suggest anisotropic behavior, nor a significantly stronger or more ductile build.

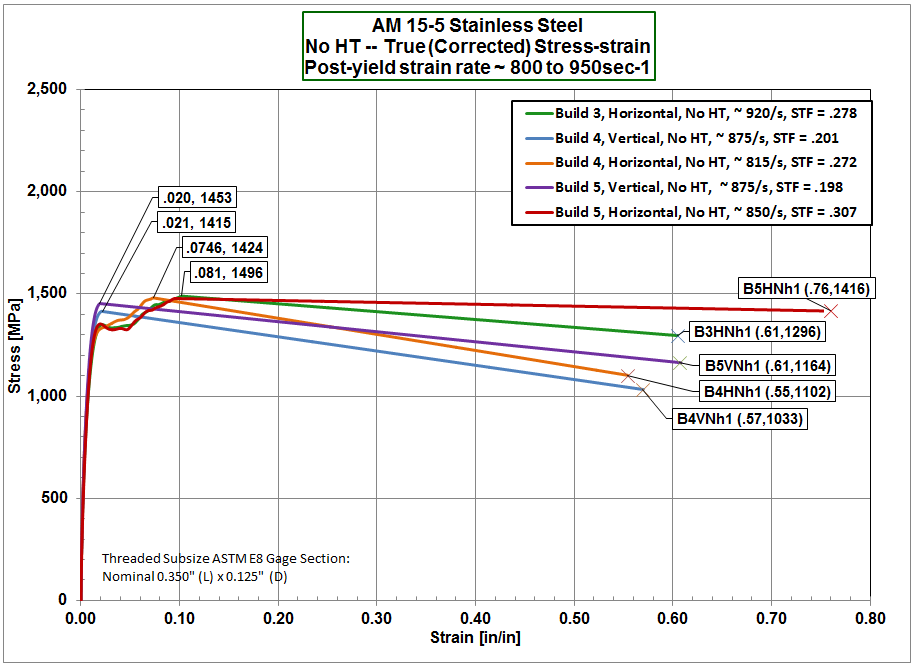

Figure 15. Non Heat Treated Samples, Horizontal Orientation, Direct Tension SHB Test, High Rate $\approx 800s^{-1}$ True Stress-Strain

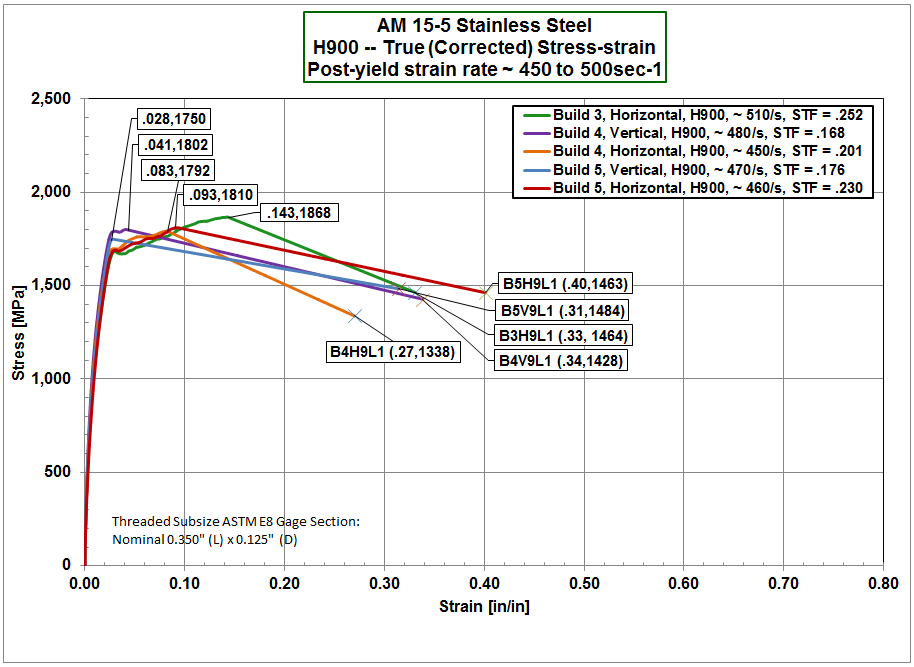

Figure 16. H900 Heat Treated Samples, Horizontal Orientation, Direct Tension SHB Test, Mid Rate $\approx 450\frac{1}{s}$ True Stress-Strain

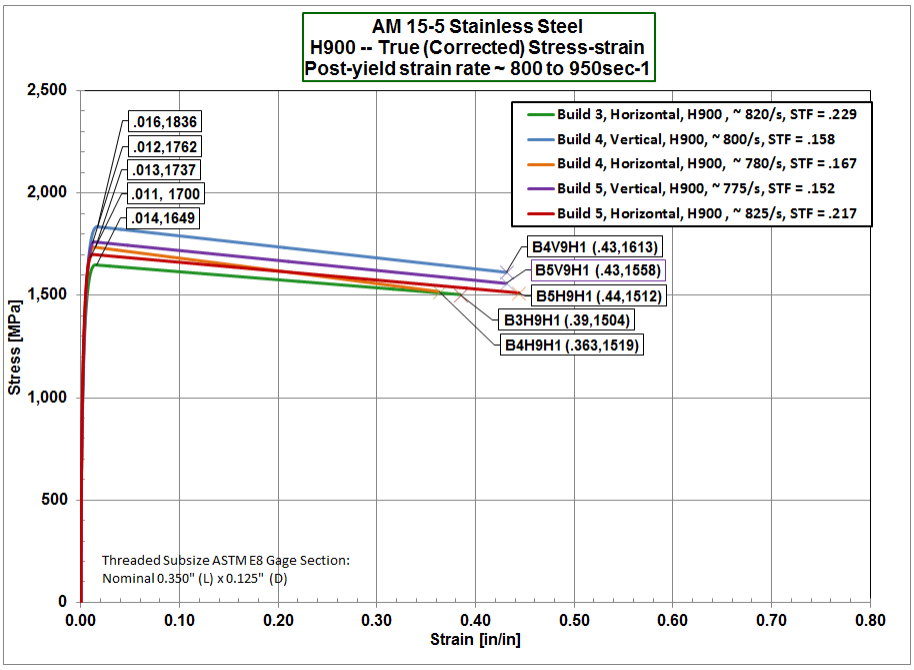

Figure 17. H900 Heat Treated Samples, Horizontal Orientation, Direct Tension SHB Test, High Rate $\approx 800\frac{1}{s}$ True Stress-Strain

4.1.2.3 H1025 Heat Treatment

The slightly overaged specimens subjected to the H1025 protocol are expected to be harder than their non-heat treated counterparts but more ductile than the H900 specimens. In general, that is where the curves in Figures 18 and 19 lie. The slope changes between the strain rates are somewhat less pronounced, but still evident. Overall, the samples of these builds show some variation, but they appear indicative of natural variation, not necessarily something induced by the build or the changes in orientation. The strain rate dependence is pronounced, with evidence of much more softening in the high rate tests than the mid rates.

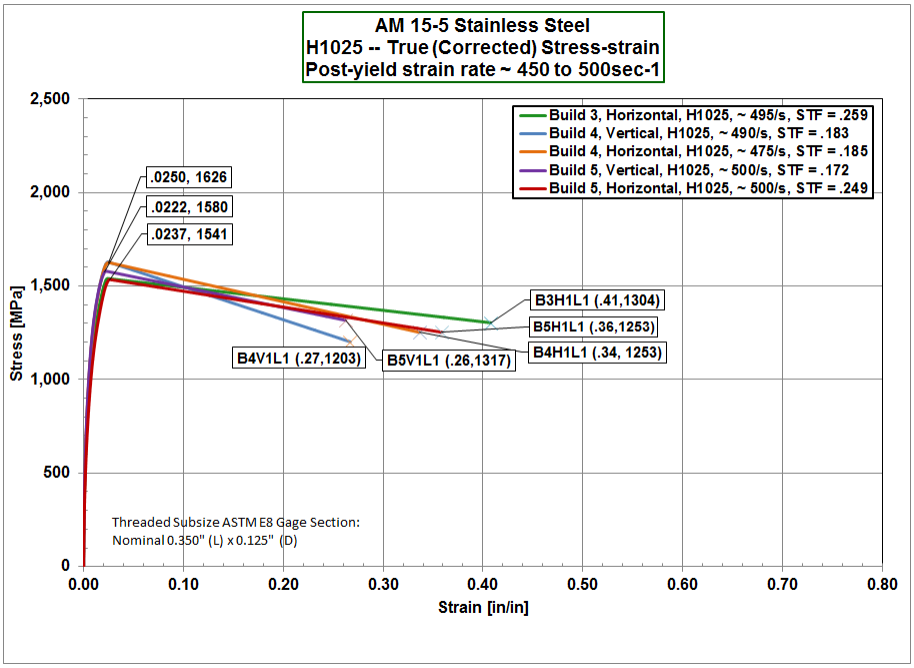

Figure 18. H1025 Heat Treated Samples, Horizontal Orientation, Direct Tension SHB Test, Mid Rate $\approx 450\frac{1}{s}$ True Stress-Strain

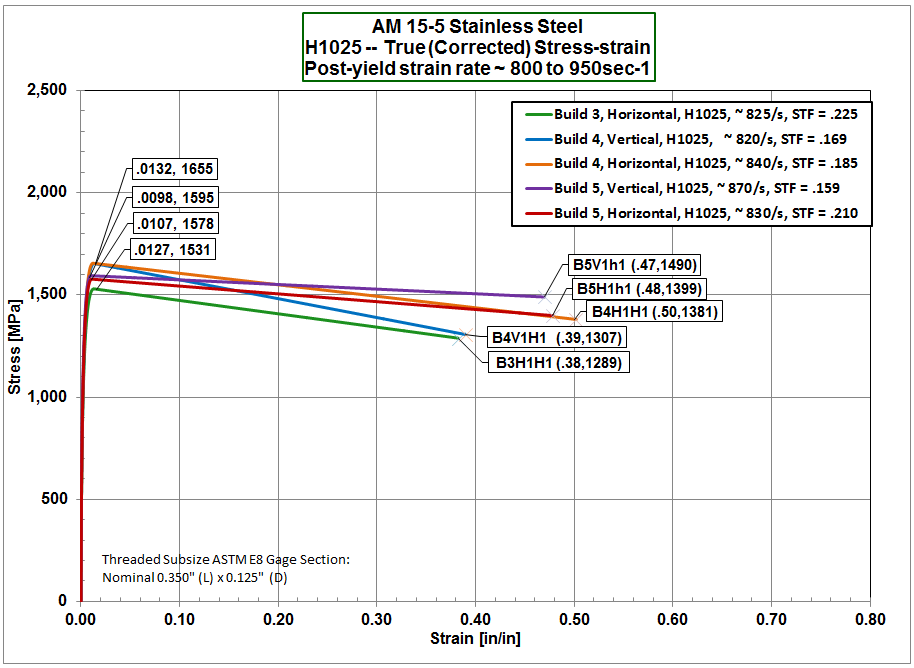

Figure 19. H1025 Heat Treated Samples, Direct Tension SHB Test, High Rate $\approx 800\frac{1}{s}$ True Stress-Strain

4.2 Build 1

Build 1 was used solely for the SHB compression test. The 15 samples were manufactured into net shape, vertically oriented with a 5.08 mm diameter cross-section and a height of 5.08 mm (a 0.2 in by 0.2 in right cylinder). The results of the EDS test in table 1 display an unexpected result: a large disparity between the alloy composition of build 1 and the 15-5PH AISI specification. Roughly equal percentages of Cr and Ni, approximately 9.5% of each instead of the specified 15% Cr and 5% Ni, could dramatically alter the composition from the expected martensite by changing the M_s and M_f temperatures.

The change in composition had a discernable impact to the microstructure, pictured in Figure 20. Although the EBSD scan suggests the resulting microstructure is almost fully martensitic, the grain size and morphology appear to differ substantially from the subsequent builds with alloy composition within the specification. The

grains are assessed to have an area on average approximately 2 to 3 times larger than those of the same orientation scans of builds 4 and 5. These large martensite plates appear somewhat randomly oriented in the circular cross section, where the influence of the powder and surface melt pool effects are expected to dominate and no dominant direction would be expected.

4.2.1 SHB Compression Test

From the engineering stress-strain graphs in Figure 54 and the results listed in Table 3, a brief comparison to the results of the compression test for build 3 display some stark differences. Although both display similar reactions to heat treatments, with noticeably harder and less ductile response, the graphs for the non-heat treated samples displayed substantially lower elongation. Additionally, the H900 hardening treatment did not enable it to reach the same UTS as build 3 experienced. Build 1 material therefore has less area under the curve and is less tough than build 3. Generally, the material in build 1 will be less able to absorb energy than build 3. The large contrast between the two cannot be assued fully explained by the difference in composition shown in table 1 because build orientation and build geometry are also variables of unknown impact. Build 1 was constructed using a vertical cross section of 5.08mm (0.2 in) diameter, and experienced no machining to remove edge effects like voids and partial powder adhesion. Therefore, no final conclusions are possible in comparison to build 3 material.

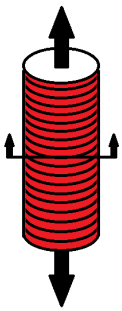

(a) Build 1 EBSD Cut Orientation

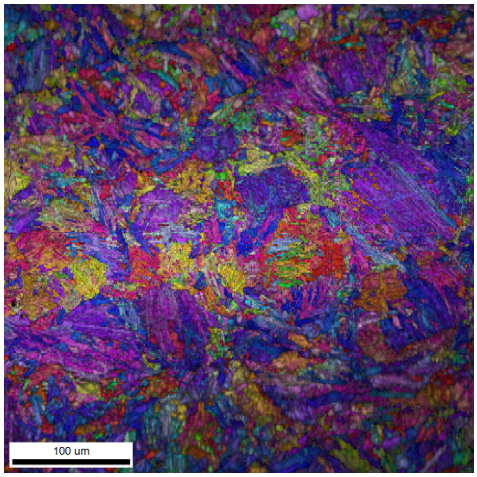

(b) Build 1 Large Area EBSD

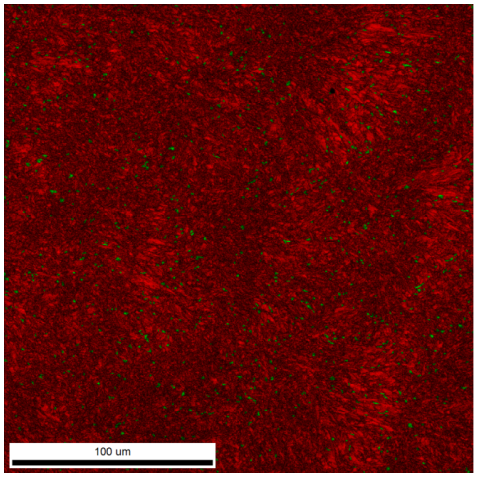

(c) 97.9% martensite, 2.1% austenite

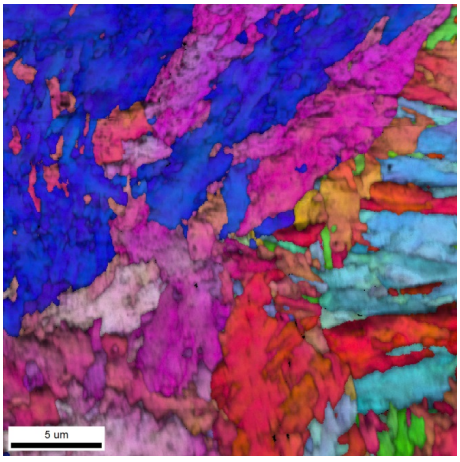

(d) Build 1 Small Area EBSD

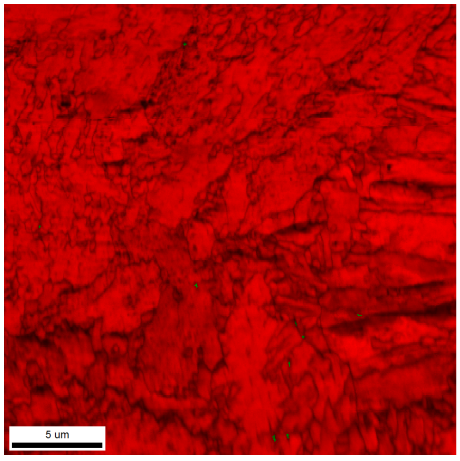

(e) 100% martensite, 0% austenite

Figure 20. Build 1, EBSD Inverse Pole Figure and Phase Map

4.3 Build 2

Build 2 was intended to represent the vertical build specimen for both quasi-static and reflected wave tension SHB tests. The build consisted of 30 cylindrical specimens, oriented vertically and built using a 12.7 mm (0.5 in) diameter cross section. The cylinders, prior to machining, were relatively smooth but with an observed pattern of vertical striations corresponding to the build layers, shown in Figure 21. Although interesting, the surface roughness and geometry effects are expected to have little impact upon material properties in this research due to the machining required to produce test specimens, except as anecdotal evidence to the effect of build layer size and orientation.

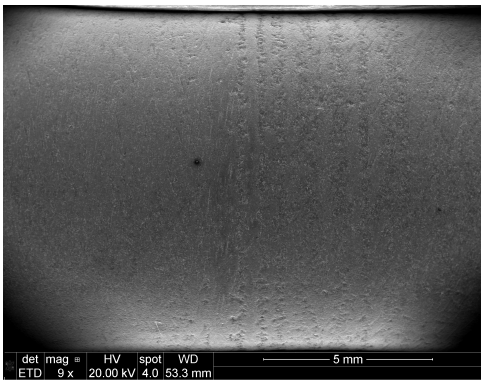

Figure 21. Build 2, Surface Texture under SEM

Of high interest, however, is finding the resultant composition EDS values, listed in Table 1, also do not fit the AISI standards for 15-5PH. Once again, the percentages of Cr and Ni are roughly equal, approximately 9% by weight. The variation, according to some of the composition diagrams [32], is potentially more likely a mix of austenite and martensitic or austenite and ferrite crystalline structure, particularly if more carbon is present than the EDS test can accurately detect. In the case of build 2, the compositional variation appears to have made a more profound impact than in build 1, as the EBSD images presented in Figure 22 show approximately 55%-65%

of the resulting microstructure is austenitic, colored green in the phase diagram. The balance, denoted in red, show the distinct grain morphology of delta ferrite. A quick check with a magnet verified the abundance of the non-magnetic austenite. Additionally, the larger area scan in Figure 22, cut roughly perpendicular to the build direction, appears to show the effect of the melt pool upon the grain formation.

4.3.1 Quasi-static Tension Test

The effect of the crystalline mix of austenite and ferrite is plainly apparent in all of the tests. Nowhere is it more obvious, however, than the almost-perfect overlay of all heat treatment conditions in the quasi-static true stress-strain curve in Figure 23.

The graph shows build 2 has no reaction to heat treatment at low strain rates. All of the test results show a trend of roughly equal moduli and UTS for all heat treatment conditions, instead of the increasing strength due to aging expected. In fact, heat treatment appears to slightly soften the material and in most cases accompany a loss of ductility in the H900 condition from the non-heat treated samples. The effect is consistent with the composition, austenite does not harden via heat treatment. Additionally, because the material has not been transformed fully to martensite, effective precipitate size and spacing distributions are not developed and there are no transformation strains upon the matrix to force the precipitation reaction. Since build 2 was so obviously different from the subsequent builds, and slightly different from build 1, its results are noted as a potential process control issue of unknown origin and seperated from those of builds 3, 4, and 5 for characterization of the AM 15-5PH material.

(a) Build 2 EBSD Cut Orientation

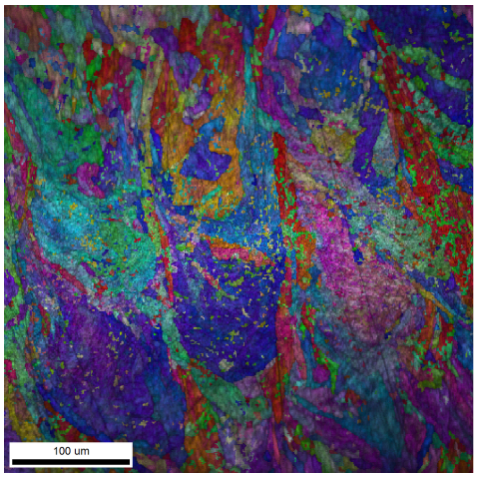

(b) Build 2 Large Area EBSD

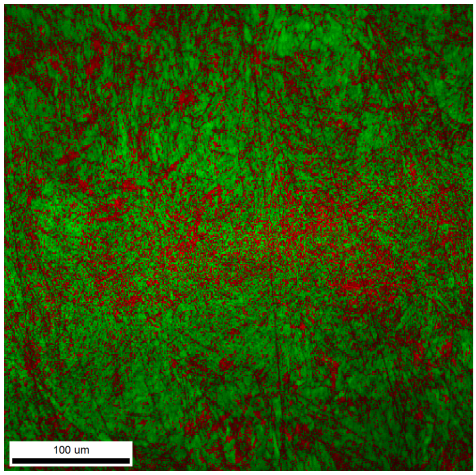

(c) 34.2% ferrite, 65.8% austenite

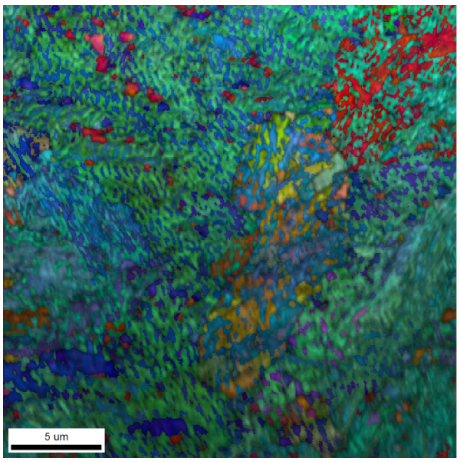

(d) Build 2 Small Area EBSD

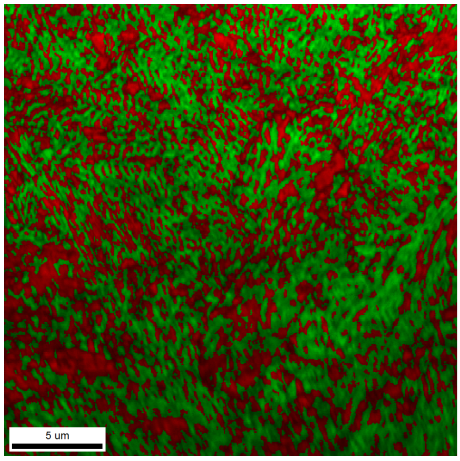

(e) 44.7% ferrite, 55.3% austenite

Figure 22. Build 2, EBSD Inverse Pole Figure and Phase Map

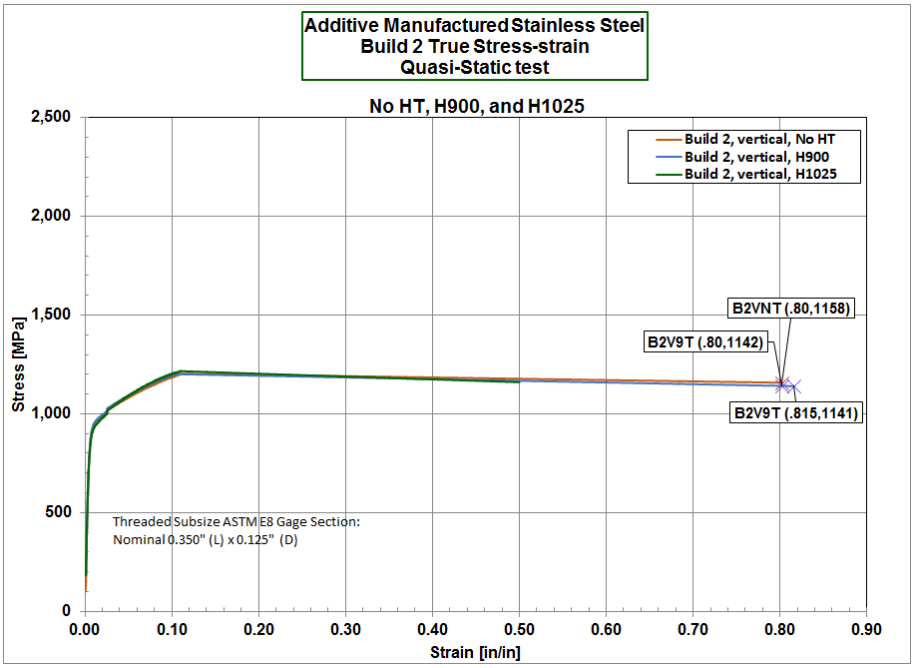

Figure 23. Build 2, Quasi-static Tension Test, True Stress-Strain

4.3.2 Reflected Wave SHB Tension Test

The results of the reflected wave SHB tests for build 2 are listed in table 3. Figure 56 in appendix D of the engineering stress-strain curve generated from the reflected wave SHB conducted at the mid rate and high rate indicate that no age hardening is occuring. All of the specimen results for each strain rate grouping lay on top of each other. A small indication of early yielding and short decline until ascending to a high point is displayed, but these changes is stress are relatively insiginificant. As the specimen fails and the curves fall with the damage evolution, the ductility does vary slightly but the elongation centers around 0.22. The mid rate curves accomodate a slightly higher stress, but the difference compared to the higher rate is negligible.

4.3.3 Momentum Trap SHB Tension Test

Comparing these results with those from the true stress-strain curves obtained from the momentum trap test tell a similar story, but show the ductility differences

far more clearly. Figure 24 of the mid-rate test shows a negligible change in strength, but a true final strain that may indicate some response to the heat treatment: H900 samples clearly the least ductile, followed by the H1025 and exceeded by the non-heat treated sample. Figure 25 of the high rate test also shows this trend, with very similar maximum stress values but much longer, shallower slopes.

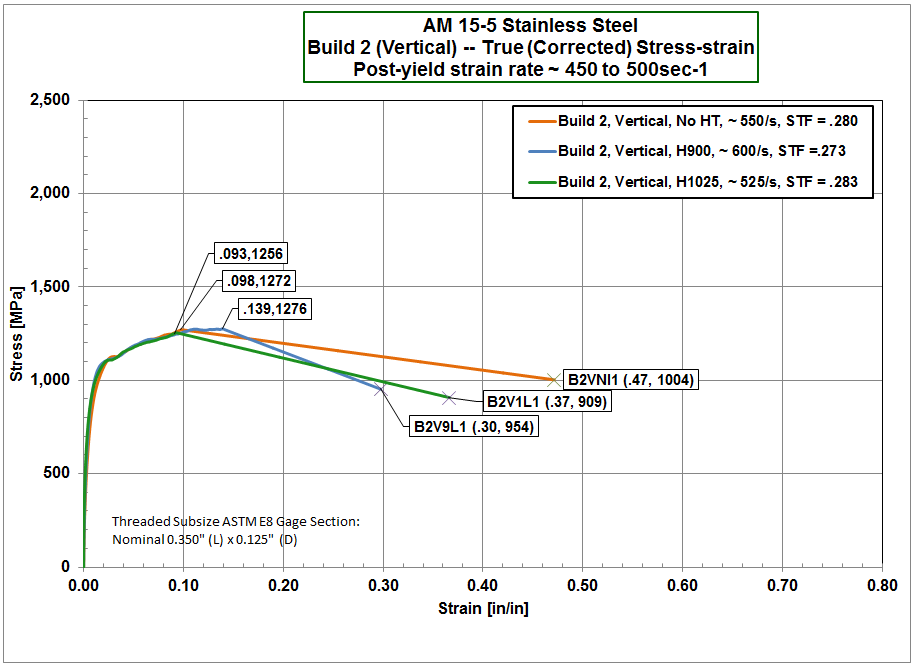

Figure 24. Build 2, Momentum Trap SHB Tension Test, True Stress-Strain, Mid Rate

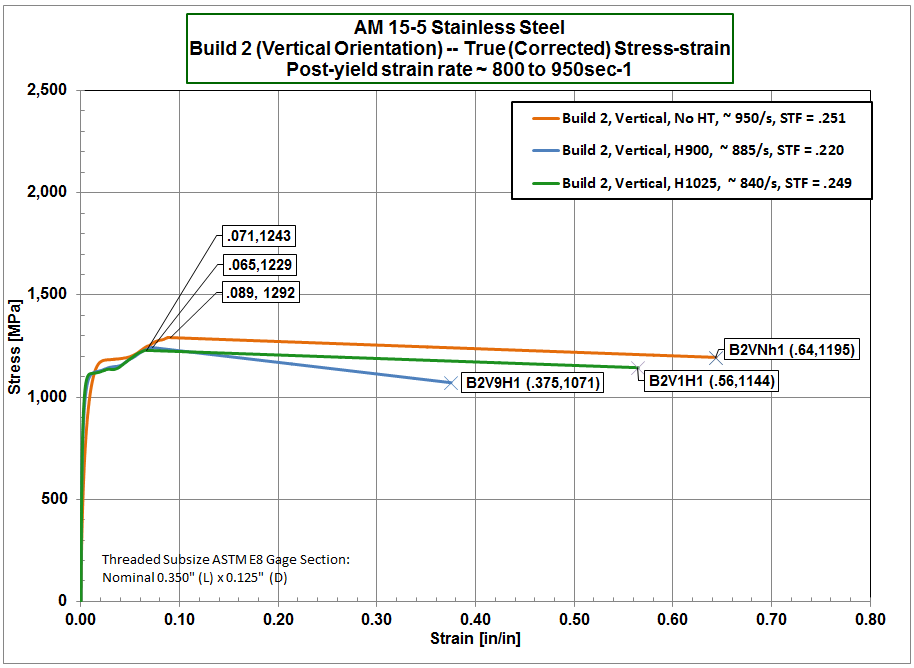

Figure 25. Build 2, Momentum Trap SHB Tension Test, True Stress-Strain, High Rate

4.4 Build 3

Build 3 is the first of the builds, by EDS evaluation, appearing to compositionally approach the 15-5PH stainless steel specification. The 30 cylinders composing the build were the first attempt at manufacturing in a horizontal orientation, using rectangular cross sections 50.8 mm (2 in) long and of varying widths to ultimately build a cylinder of 12.7 mm (0.5 in) diameter. Upon receipt of the build, it was immediately obvious the surface was much rougher than the vertically oriented build and each piece was noticeably bowed, as seen in Figure 26.

The warping is the result of a thermal gradient within the material as it built, coupled with insufficient support during the build. Although the samples were machined into final shape for testing, the residual stresses assumed to still accompany the distortion may have compromised the test data by pre-stressing or pre-cracking the material.

Microstructurally, build 3 displays more desirable characteristics than builds 1

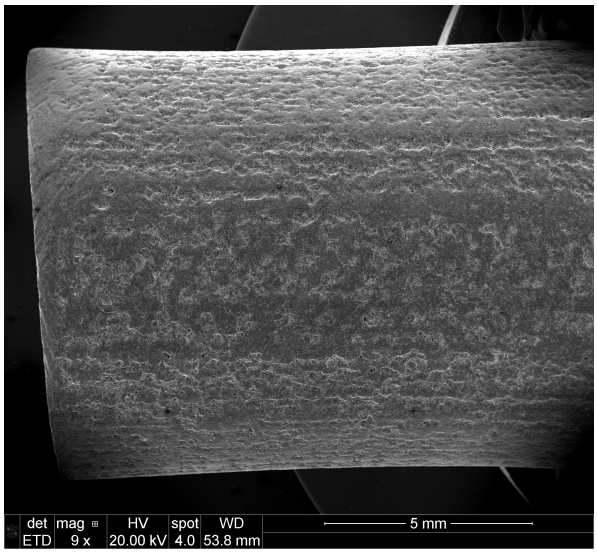

(a) Build 3 Surface under SEM

(b) Build 3 photograph

Figure 26. Build 3, Surface Finish and Image

or 2. The EBSD images in Figure 27 show some retained austenite, approximately 10% in the small area scan, the remainder is composed of relatively fine martensitic laths of various crystalline orientations. The prevalence of martensite indicates that this material should age harden. Except for the concern over the residual stresses that may be involved, tests of build 3 should give a good indication of the dynamic behavior of 15-5PH stainless steel built in an orientation parallel to the load axis.

(a) Build 3 EBSD Cut Orientation

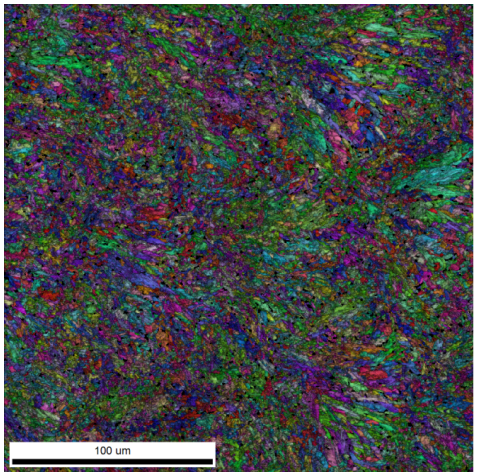

(b) Build 3 Large Area EBSD

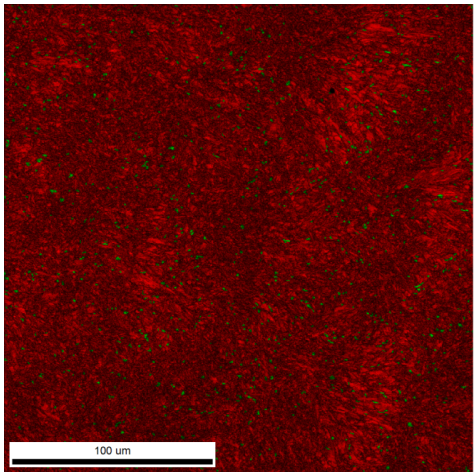

(c) 97.9% martensite, 2.1% austenite

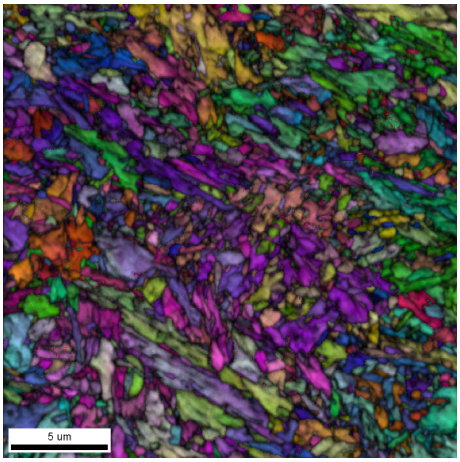

(d) Build 3 Small Area EBSD

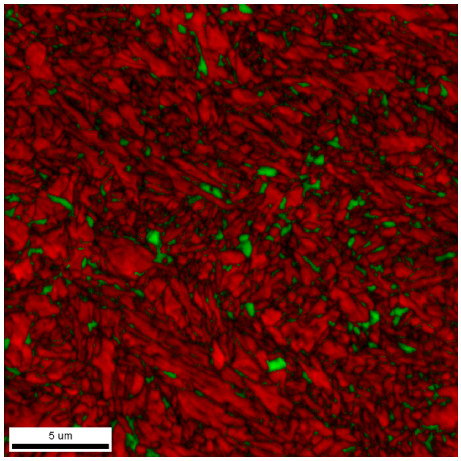

(e) 90.4% martensite, 9.6% austenite

Figure 27. Build 3, EBSD Inverse Pole Figure and Phase Map

4.4.1 Quasi-static Tension Test

The results of the quasi-static test fit the expectation of age hardening. The true stress-strain curve in Figure 28 and results in Table 13. The UTS clearly exceeds the specifications for AK Steel, an example of a standard wrought material [1] and the performance specifications in Military Handbook 5H [3] for each heat treatment condition. Additionally, there is a distinct rise in strength and corresponding drop in ductility for the H900 heat treatment protocol, and a slight drop in strength from the H900 condition and increase in ductility for the H1025 condition.

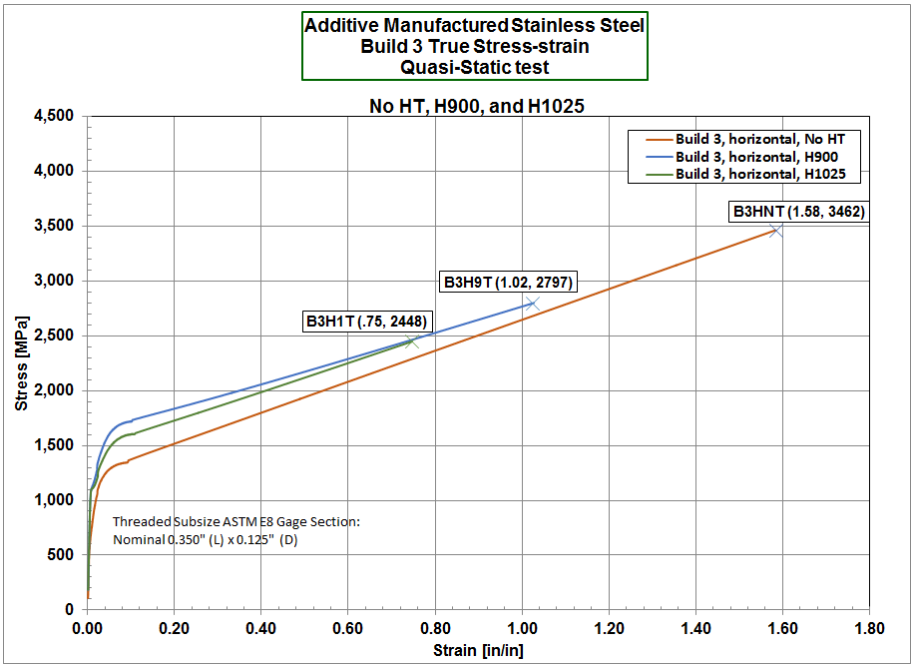

Figure 28. Build 3, Quasi-static Tension Test, True Stress-Strain

4.4.2 SHB Compression Test

The compression SHB curve in Figure 11 corresponding to the results listed in table 14 is dramatically different than for build 1. It was feasible, however, to construct a true-stress strain graph using the final stress-strain calculated by measuring the final cross-sectional area. The results, in Figure 29 display the expected aging

trend with heat treatment, highest ductility for the non-heat treated samples, highest strength at H900, and moderately strong and ductile for the H1025. Additionally, the maximum compression stress value is much larger than the maximum tension stress in the quasi-static test for the same material. The disparity is typical for steels, the compressive stress does not induce yielding at points of stress concentration like cracks or voids and will instead tend to close those defects and work harden the material.

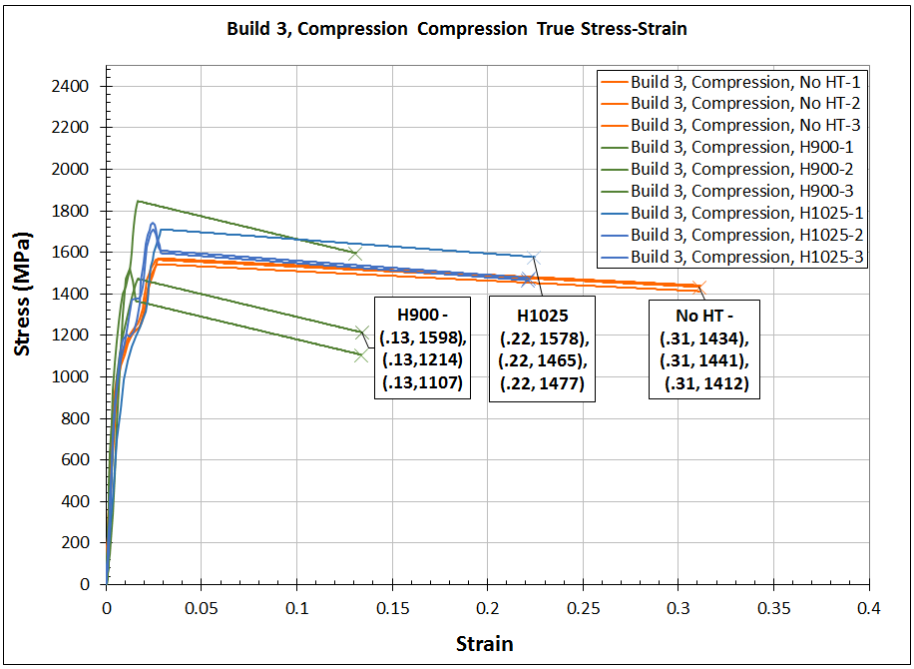

Figure 29. Build 3, SHB Compression Test, True Stress-Strain

4.4.3 Reflected Wave SHB Tension Test

The results for the SHB test conducted using the reflected wave setup are listed in Table 4. The behavior of the material under dynamic tension is displayed in the engineering stress-strain graphs in Figures 57 and 58 in Appendix D. The build 3 engineering stress curves clearly show the precipitation hardening phenomenon. Each also displays discontinuous yielding where the strain quickly reaches an upper yield point until it peaks and falls and then slowly climbs up to the final value. The phenomena is a result of the dislocation density of the material. When a metal is plastically deformed, the flow of the metal matrix generates defects, or dislocations, in the crystal structure [30]. As the metal is loaded, the dislocations tend to get locked until it takes more stress to overcome them. The quick impact of the SHB test imparts a large amount of energy into the specimen. When the upper limit can overcome the resistance of the pinned dislocations is reached, the stress dramatically drops. As the material is deformed more, the stress steadily increases as energy is imparted to plastically deform the material further. In the case of build 3, the residual stress induced by the build could exacerbate the phenomena.

The unexpected compositional variation of build 2 introduced an additional variable to the reflected wave SHB tension test. Therefore, build orientation could not be objectively compared. Additional samples were tested on the direct impact tension SHB to determine the true expected variation in build orientation. A comparison of the results for build 3 for each test in table 4 show the UTS values for the non-heat treated specimens were approximately 5% to 9% higher for the direct tension bar specimens, and the maximum strain values were 20% to 30% higher. The lower values for the reflection method may reflect the method of loading, since the collar used over the sample cannot prevent some of the initial compression wave to affect the sample [20]. Additionally, the difference in threading specifications may impart

some of the deviation.

4.4.4 Momentum Trap SHB Tension Test

The momentum trap SHB test results in Table 4 appear to present fairly stable precipitation hardening trends. The strain rate dependence for build 3 appears small since the UTS varied by less than 2.5%, although the ultimate strain was on average 9% less for the mid strain rate than the high strain rate. In general, build 3, built in the horizontal orientation, slightly underperformed as compared to the vertically built specimens of build 4 and 5 in terms of strength, while agreeing within approximately 5% to the other horizontal results. However, they have significantly better ductility, on the order of 30% for each heat treatment condition.

Examining the direct impact momentum trap tension data of builds 3, 4, and 5 in Figures 14 through 19 appear to show build 3 experienced the highest difference in true stress applied from the non-heat treated condition to the H900 condition for both mid and high strain rates. The higher loss appears due to the anomalous ductility for the non-heat treated condition and is not reflected in the values found for UTS and maximum strain. The maximum tensile strength increase from non-heat treated to H900 is approximately 22% and from non-heat treated to H1025 is 12%, which is within 3% of the other builds. Similarly, the decrease in maximum strain is 12% and 18% for the respective heat treatments, in line with the changes in the other two build groups. The differences between the build 3 heat treatments is further explored in Figures 30 and 31. Of note, the non-heat treated condition seems to retain a higher slope (true stress over true strain) than those of the the other builds.

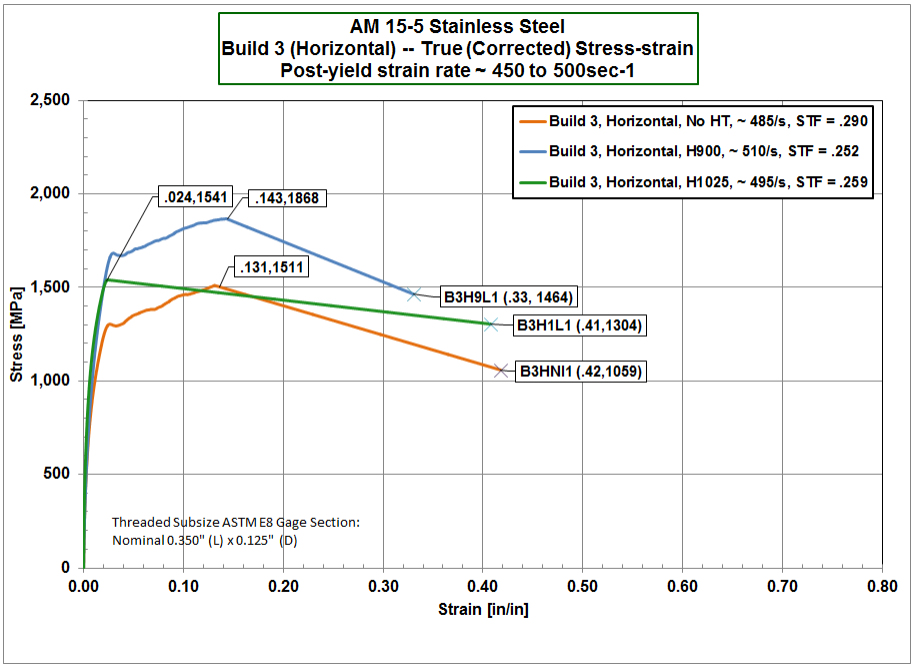

Figure 30. Build 3, Momentum Trap SHB Tension Test, True Stress-Strain, Mid Rate

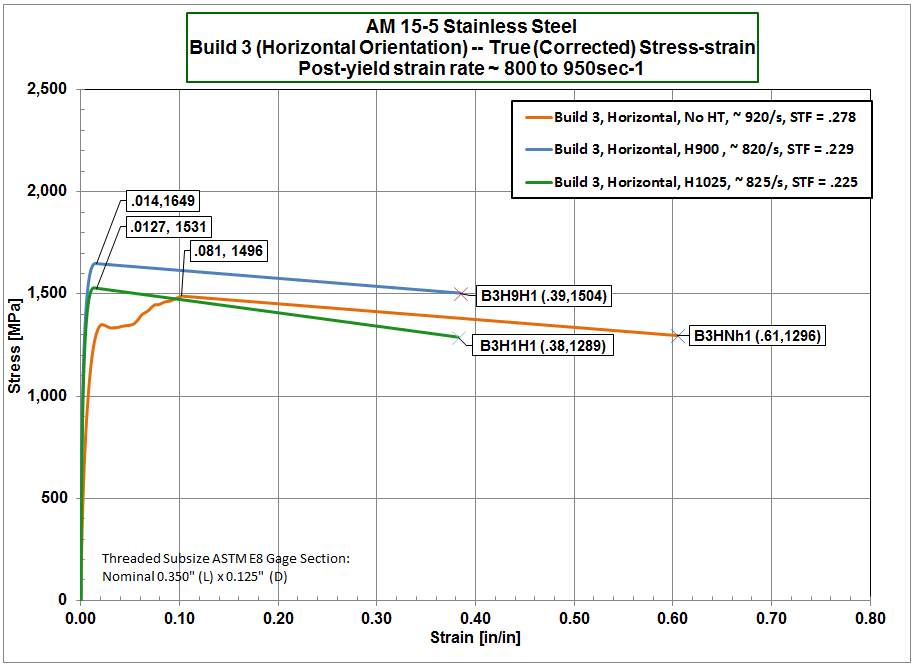

Figure 31. Build 3, Momentum Trap SHB Tension Test, True Stress-Strain, High Rate

4.5 Build 4

According to the EDS results in table 1, build 4 is also compositionally in agreement with the specifications for 15-5PH and is therefore expected to provide a equal basis for comparison to the wrought material. Due to the previous disparity between the builds, build 4 was split into two build directions: 15 of the 12.7 mm (0.5 in.) diameter and 50.8 mm (2 in.) long cylinders were built vertically and 15 more were built horizontally. Those built horizontally were manufactured with concern for eliminating distortion by providing support during the manufacturing process, resulting in relatively smooth surfaces for both the vertical and horizontal build orientations with little warping noted. Three of each orientation were used for quasi-static testing and the remaining were devoted to the direct SHB testing.

4.5.1 EBSD

The EBSD scans of build 4 in Figures 32 through 35 reveal microstructure affected by the method of AM. A scan of each orientation, both across the build direction and roughly within the build direction, are included for comparison. All of the EBSD scans display almost fully martensitic crystalline structure. Those cut to approximate the build direction, Figures 32 and 34, show fine grains without discernable patterning except perhaps a slight grain orientation alignment. Those cut roughly perpendicular to the build direction, Figures 33 and 35, are quite different. In each, sintering layers of approximately 20 μm thickness during the DMLS processing results in some distinct effects upon the grain formation and microstructure. The scans across the build show evidence of the layering, and those with the build show influence of the melt pool in some of the texture effects. The horizontally built circular specimen in Figure 35, are reminiscent of the beam traces seen under microscopy with circular grain patterns that appear to be influenced by cooling of the layers and individual melt pools.

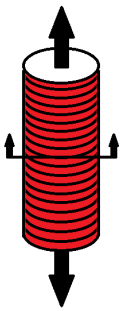

(a) Build 4, Vertical Build, Cut With Build

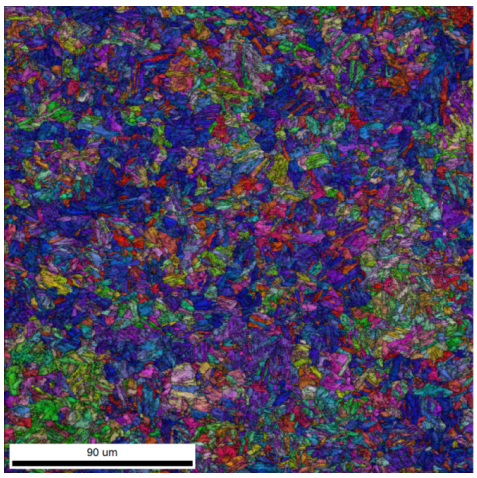

(b) Build 4, Vertical Build, Large Area EBSD

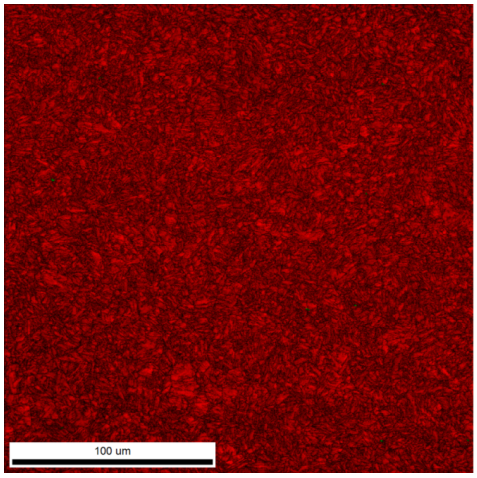

(c) 97.9% martensite, 2.1% austenite

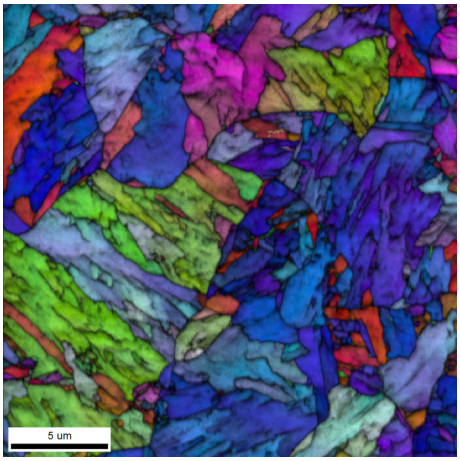

(d) Build 4, Vertical Build, Small Area EBSD

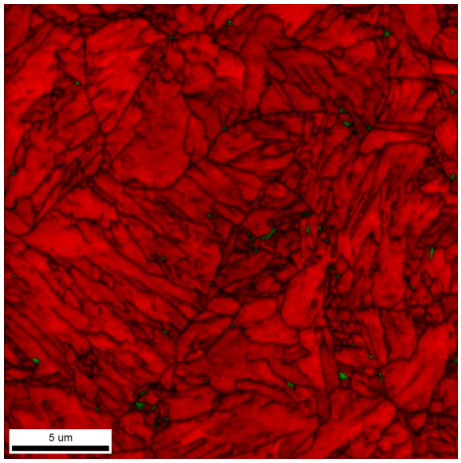

(e) 100% martensite, 0% austenite

Figure 32. Build 4, Vertical Build, Cut With Build Orientation, EBSD Inverse Pole Figure and Phase Map

(a) Build 4, Vertical Build, Cut Across Build

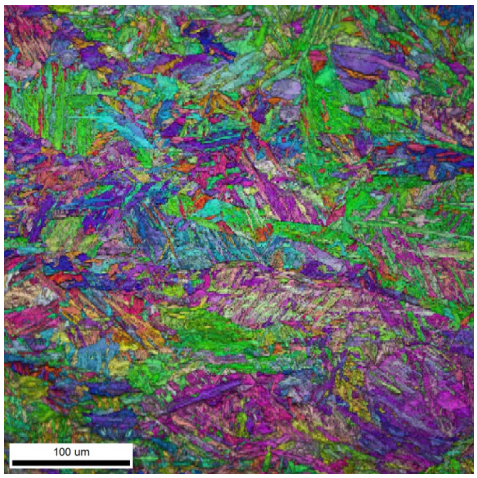

(b) Build 4, Vertical Build, Large Area EBSD

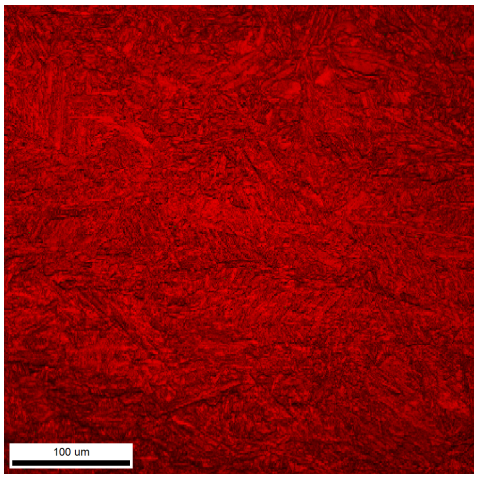

(c) 99.6% martensite, 0.4% austenite

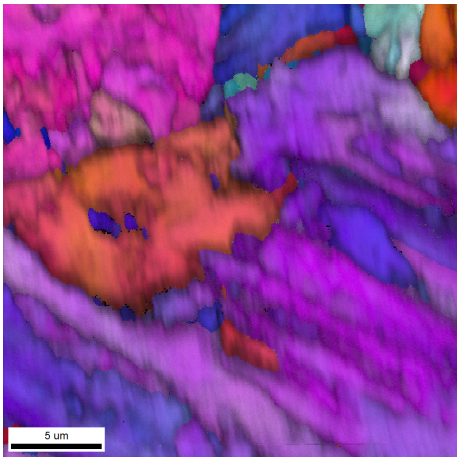

(d) Build 4, Vertical Build, Small Area EBSD

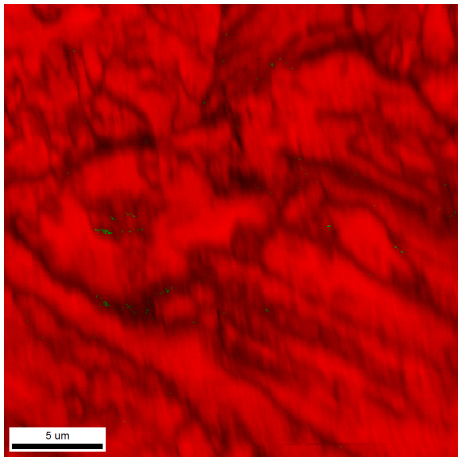

(e) 90.4% martensite, 9.6% austenite

Figure 33. Build 4, Vertical Build, Cut Across Build Orientation, EBSD Inverse Pole Figure and Phase Map

(a) Build 4, Horizontal Build, Cut With Build

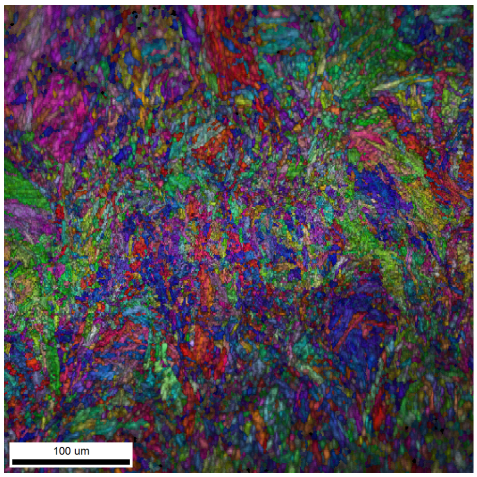

(b) Build 4, Horizontal Build, Large Area EBSD

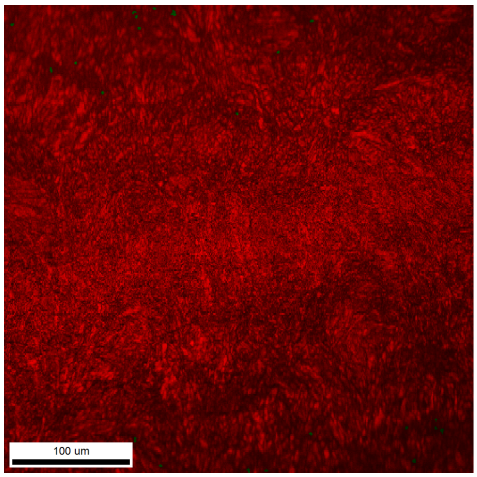

(c) 98.9% martensite, 1.1% austenite

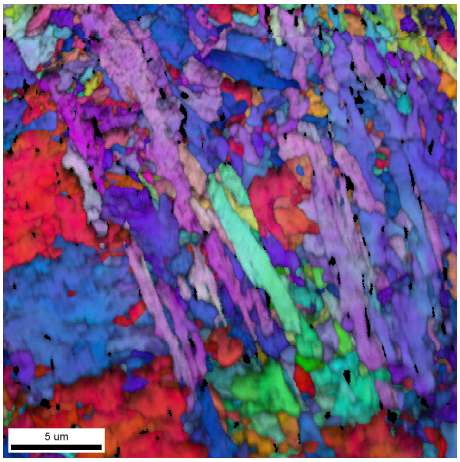

(d) Build 4, Vertical Build, Small Area EBSD

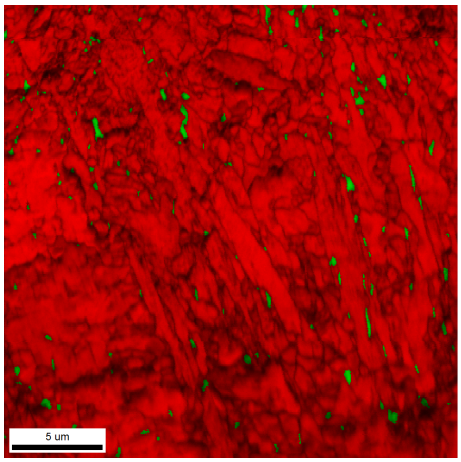

(e) 99.9% martensite, 0.1% austenite

Figure 34. Build 4, Vertical Build, Cut With Build Orientation, EBSD Inverse Pole Figure and Phase Map

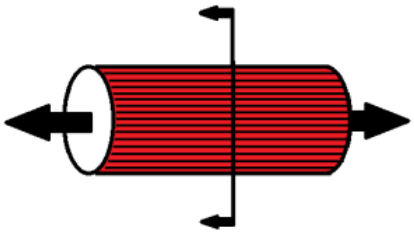

(a) Build 4, Horizontal Build, EBSD Cut Across Build

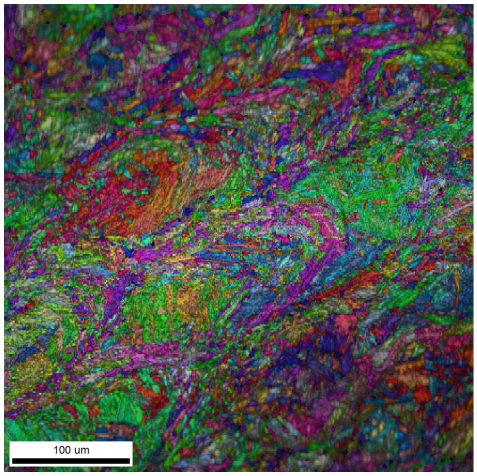

(b) Build 4, Horizontal Build, Large Area EBSD

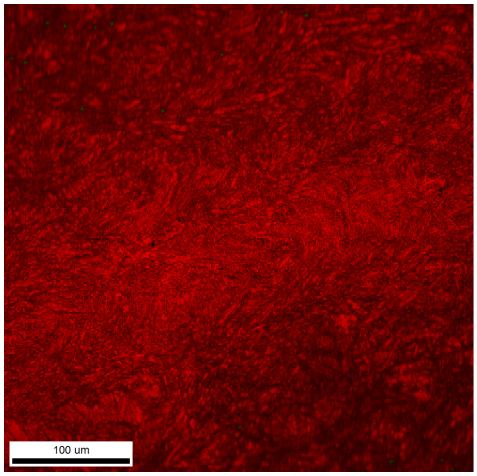

(c) 99.9% martensite, 0.1% austenite

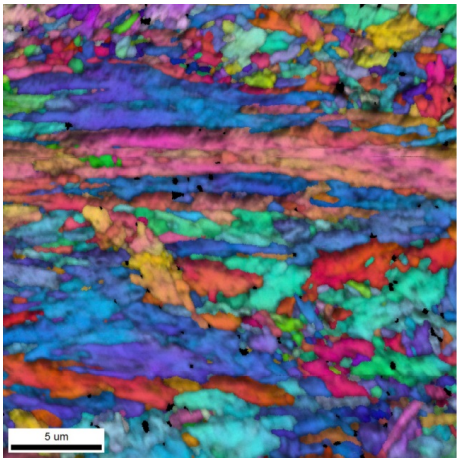

(d) Build 4, Horizontal Build, Small Area EBSD

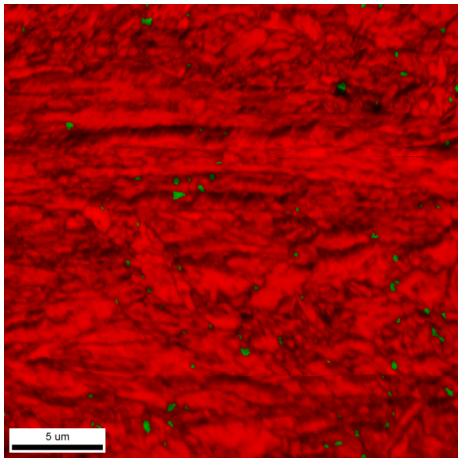

(e) 98.4% martensite, 1.6% austenite

Figure 35. Build 4, Horizontal Build, Cut Across Build Orientation, EBSD Inverse Pole Figure and Phase Map

4.5.2 Quasi-static Tension Test

The quasi-static tension results yield some striking differences in ductility between the build orientations. The results are listed in Table 13. Despite close agreement in UTS, within 1% for the non-heat treated and H900 conditions, the horizontally built samples display much higher ultimate strain behavior, 20% to 30% higher in each heat treatment condition. The results suggest there is anisotropy according to build direction, the bonds within layers may exhibit more strength than those across the melted layers. The difference are seen clearly in the engineering stress-strain graph in Figure 53. Overall, each orientation tends to exceed the published values [1, 3] except for the 0.2% offset yield and modulus values. The behavior suggests a shallower elastic response, with a pronounced drop after initial yield. Therefore, the stiffness of the AM material is potentially as much as 25% lower than the wrought material, and plastic deformation is likely to occur sooner in the AM material.

4.5.3 Momentum Trap SHB Tension Test

The results of the momentum trap, direct SHB tension tests are listed in Table 5. The vertical build orientation results shown in Figure 36 and 37 clearly show the variation by heat treatment and the shallower, longer curves at the higher rates. The horizontal build orientation test results in Figure 39 and 38 are very closely matched in performance, the H900 UTS vary by less than 1.5%, the H1025 by only 2%.

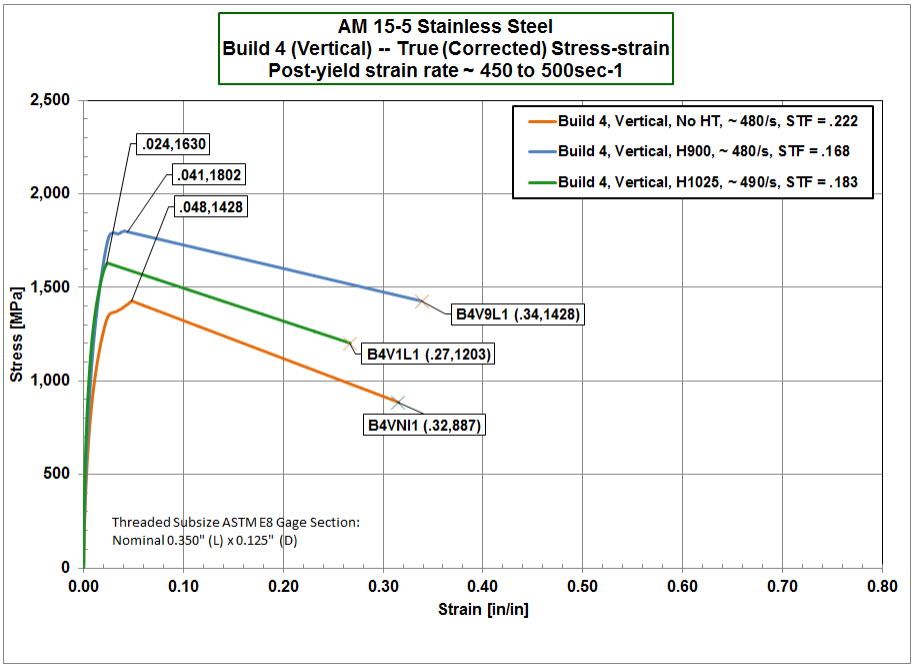

Figure 36. Build 4, Momentum Trap SHB Tension Test, True Stress-Strain, Mid Rate

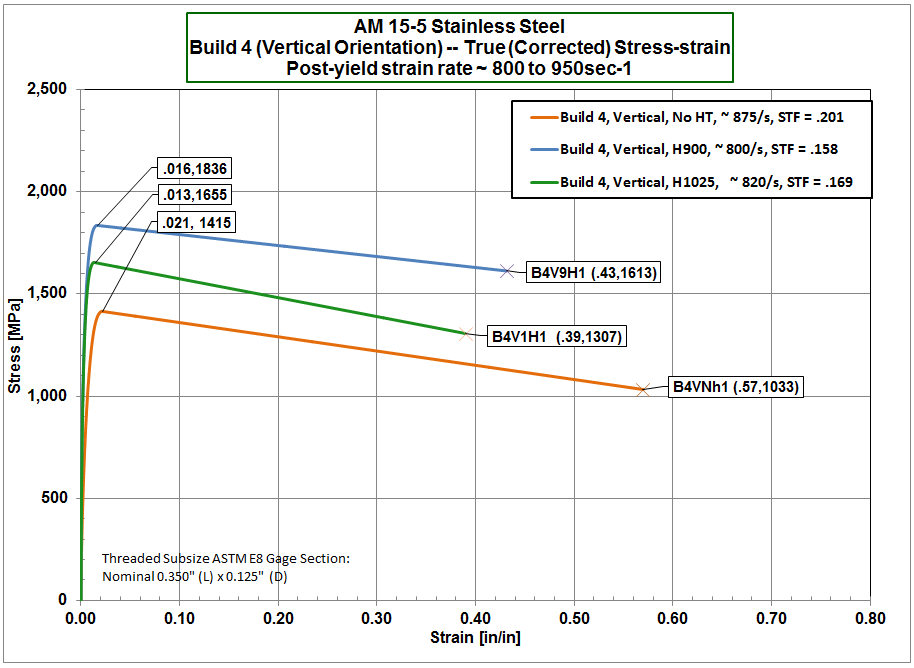

Figure 37. Build 4, Momentum Trap SHB Tension Test, True Stress-Strain, High Rate

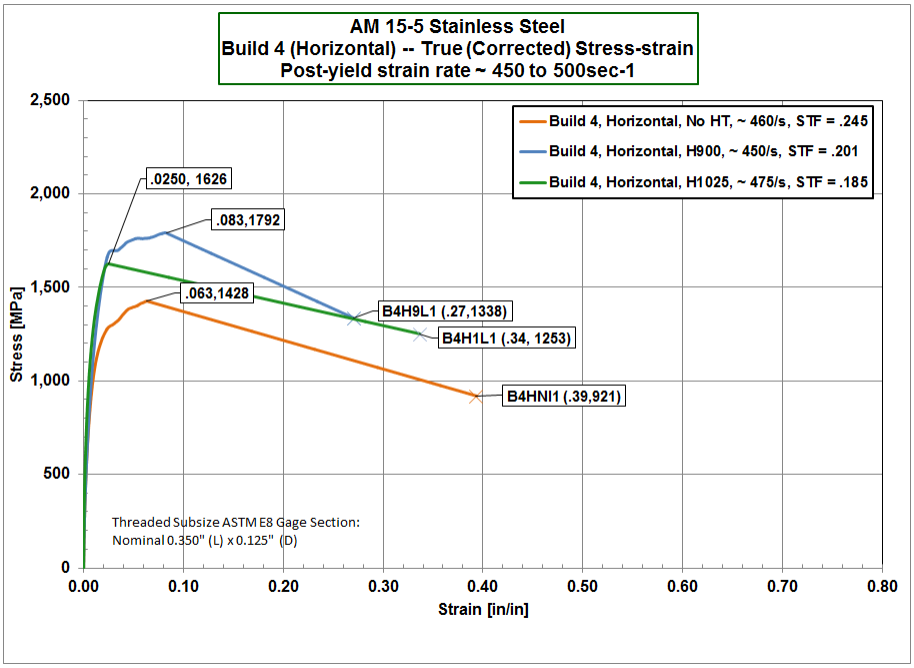

Figure 38. Build 4, Momentum Trap SHB Tension Test, True Stress-Strain, Mid Rate

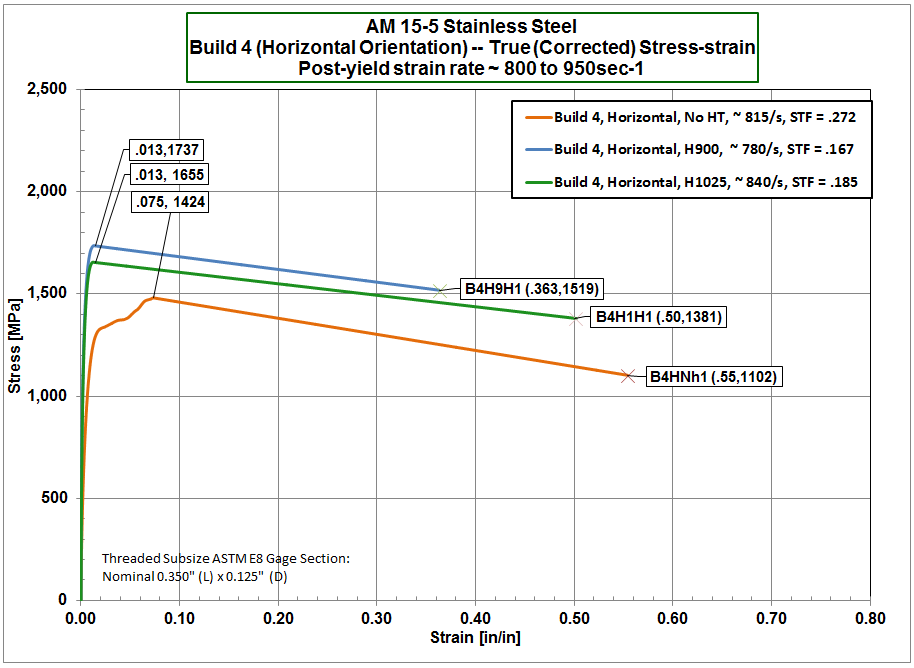

Figure 39. Build 4, Momentum Trap SHB Tension Test, True Stress-Strain, High Rate

4.6 Build 5

Build 5 is also expected to accurately represent AM 15-5PH by composition. The results of the EDS semi-quantitative analysis shown in Table 1 meet the standard for the wrought material. The EBSD scans in Figure 40 through 43 reflect the change as an extremely fine grained material that is again almost completely martensite.

4.6.1 Momentum Trap SHB Tension Tests

As in build 4, the 30 12.7 mm (0.5 in.) diameter and 50.8 mm (2 in.) long cylinders were split into two build batches: 15 vertically oriented and 15 horizontally oriented. They were machined into the cylindrical samples for use in the direct tension SHB test. However, these were only subjected to the Momentum Trap SHB test. The results are listed in Table 6. They are graphically displayed in Figures 44 through 47.

While the UTS values between the vertical and horizontal build 5 are within 3% of each other, the maximum strains average more than 35% more for the horizontal build orientation. The outcome is the same when comparing the vertical orientation of build 4 to the horizontal orientation of build 5. Overall, the UTS for build 5 are slightly lower than for the other builds, but tend to be within 5%. The elongation of the vertical is roughly equivalent to the elongation of the build 4 vertical orientation, but the horizontal orientation ductility is greater than all of the previously tested materials.

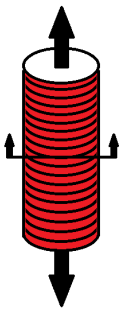

(a) Build 5, Vertical Build, Cut With Build

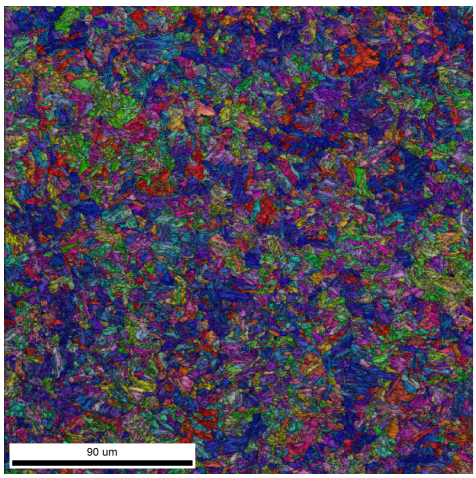

(b) Build 5, Vertical Build, Large Area EBSD

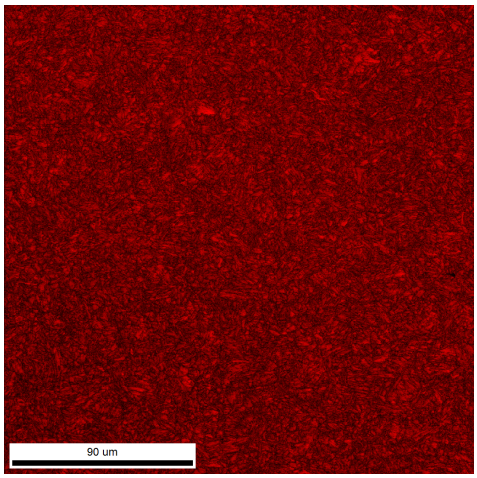

(c) 100% martensite, 0% austenite

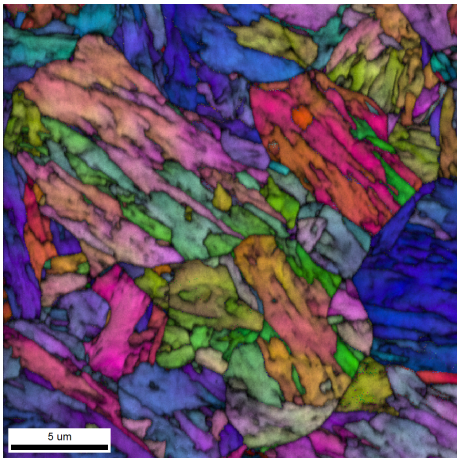

(d) Build 5, Vertical Build, Small Area EBSD

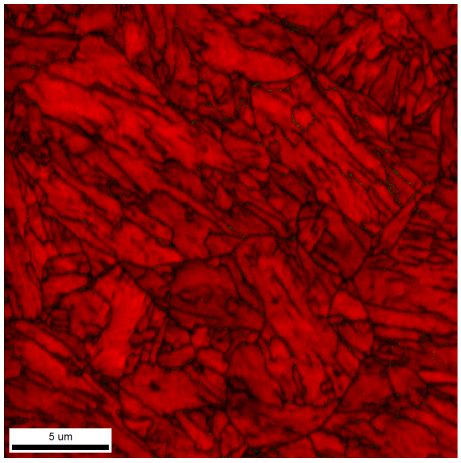

(e) 99.4% martensite, 0.6% austenite

Figure 40. Build 5, Vertical Build, Cut With Build Orientation, EBSD Inverse Pole Figure and Phase Map

(a) Build 5, Vertical Build, Cut Across Build

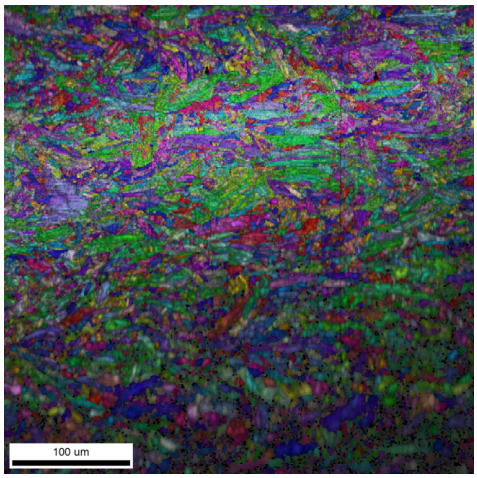

(b) Build 5, Vertical Build, Large Area EBSD

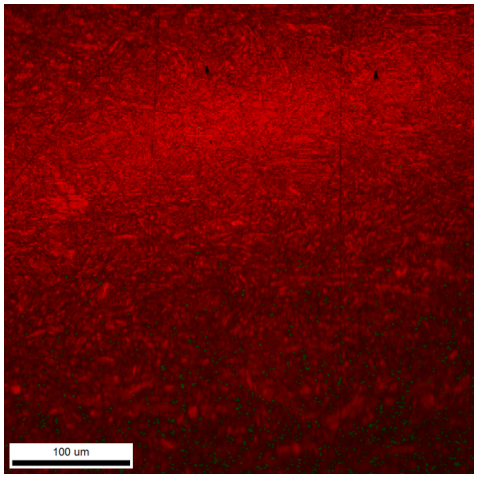

(c) 100% martensite, 0% austenite

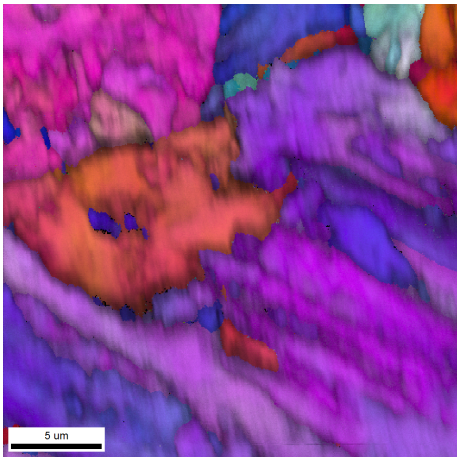

(d) Build 5, Vertical Build, Small Area EBSD

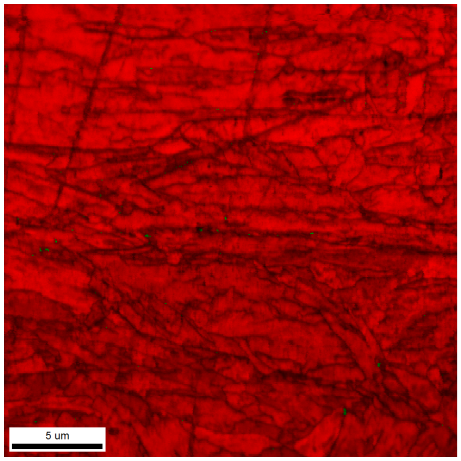

(e) 99.2% martensite, 0.8% austenite

Figure 41. Build 5, Vertical Build, Cut Across Build Orientation, EBSD Inverse Pole Figure and Phase Map

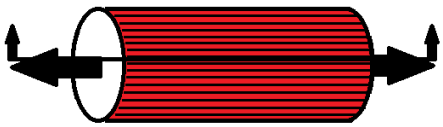

(a) Build 5, Horizontal Build, Cut With Build

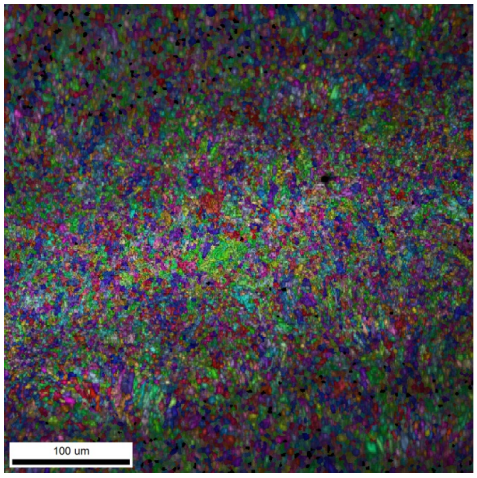

(b) Build 5, Horizontal Build, Large Area EBSD

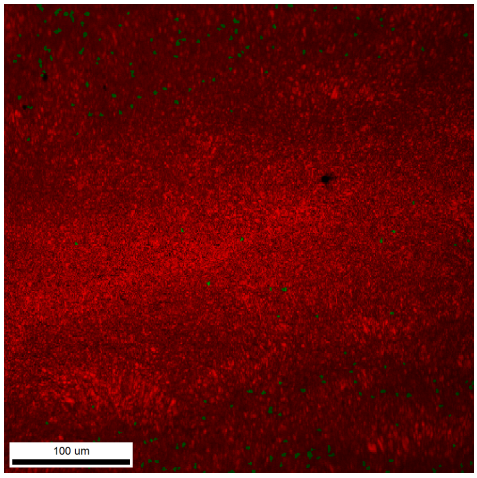

(c) 98.4% martensite, 1.6% austenite

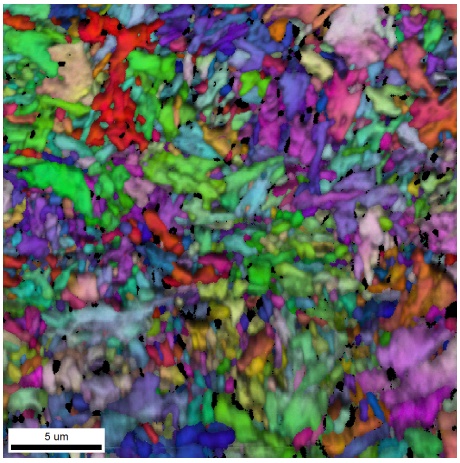

(d) Build 5, Vertical Build, Small Area EBSD

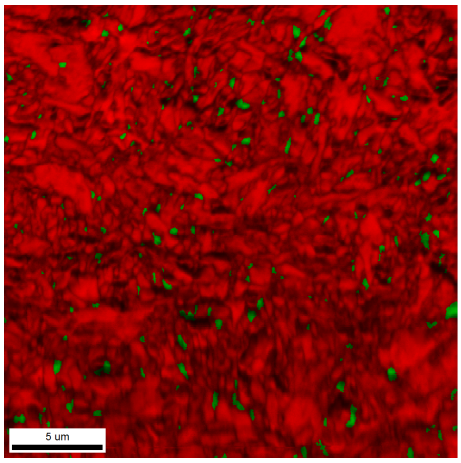

(e) 99.9% martensite, 0.1% austenite

Figure 42. Build 5, Vertical Build, Cut With Build Orientation, EBSD Inverse Pole Figure and Phase Map

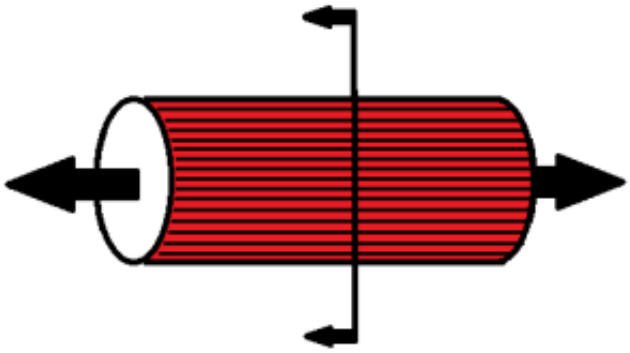

(a) Build 5, Horizontal Build, EBSD Cut Across Build

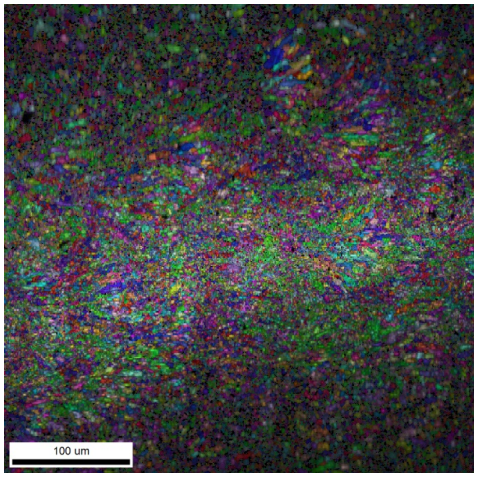

(b) Build 5, Horizontal Build, Large Area EBSD

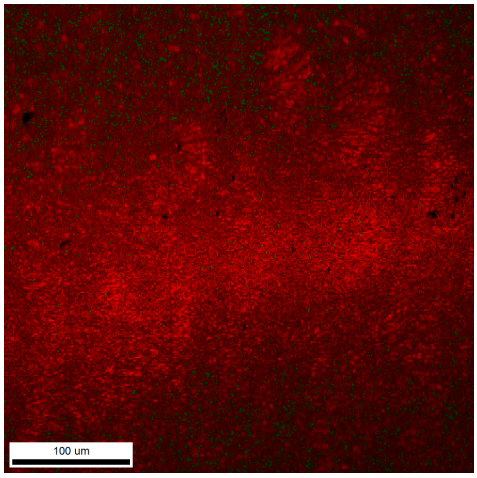

(c) 97.9% martensite, 2.1% austenite

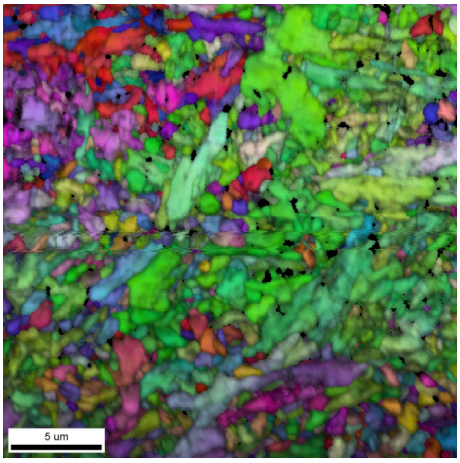

(d) Build 5, Horizontal Build, Small Area EBSD

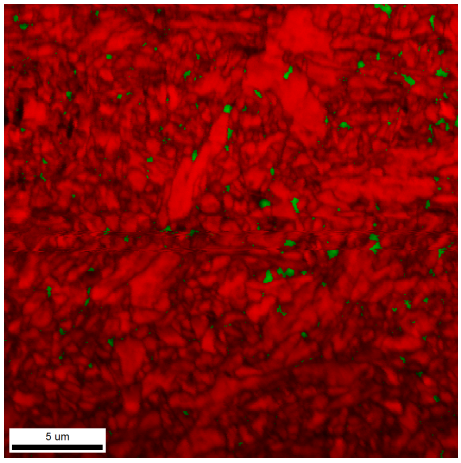

(e) 90.4% martensite, 9.6% austenite

Figure 43. Build 5, Horizontal Build, Cut Across Build Orientation, EBSD Inverse Pole Figure and Phase Map

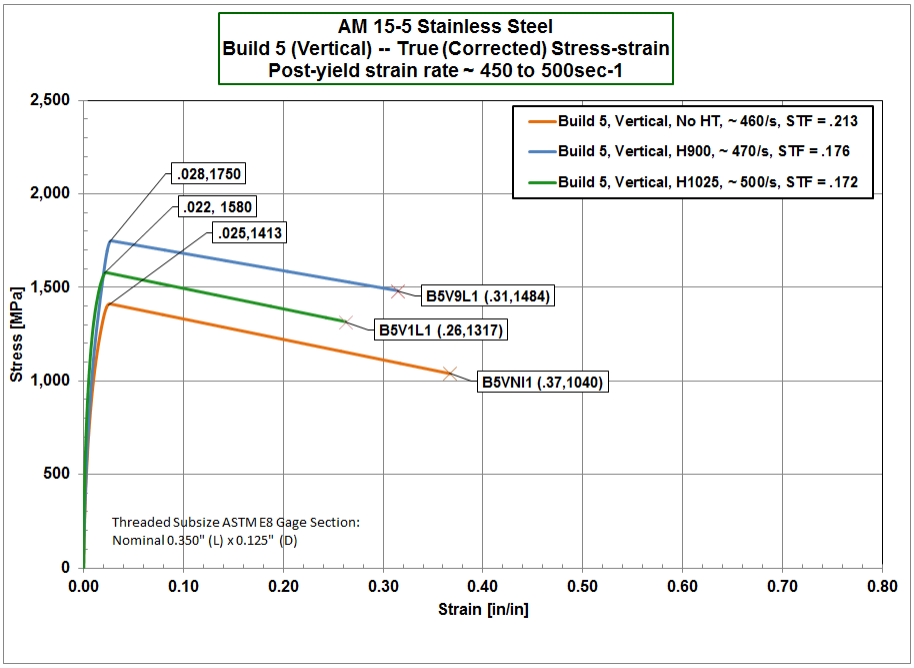

Figure 44. Build 5, Momentum Trap SHB Tension Test, True Stress-Strain, Mid Rate

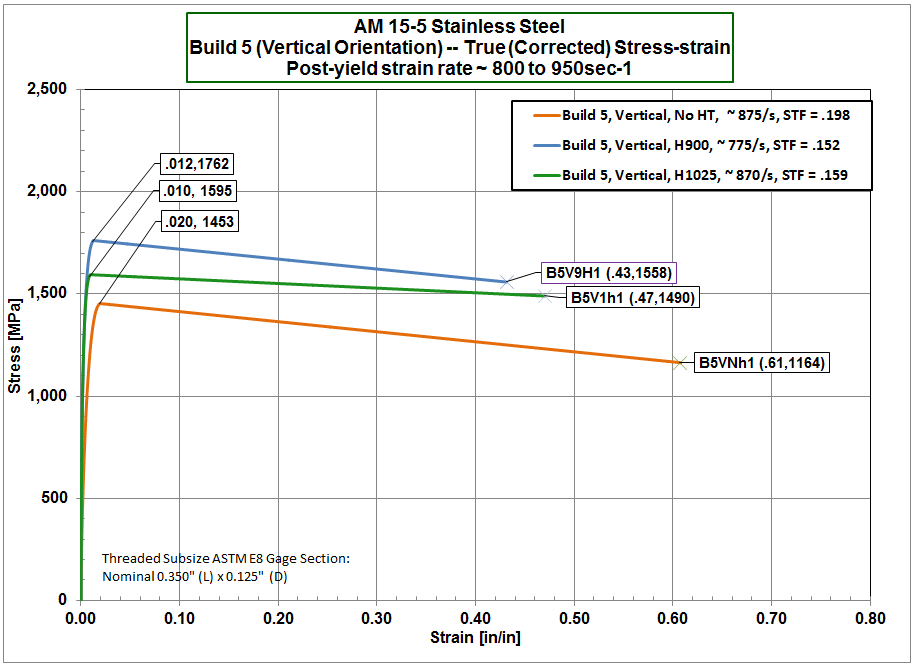

Figure 45. Build 5, Momentum Trap SHB Tension Test, True Stress-Strain, High Rate

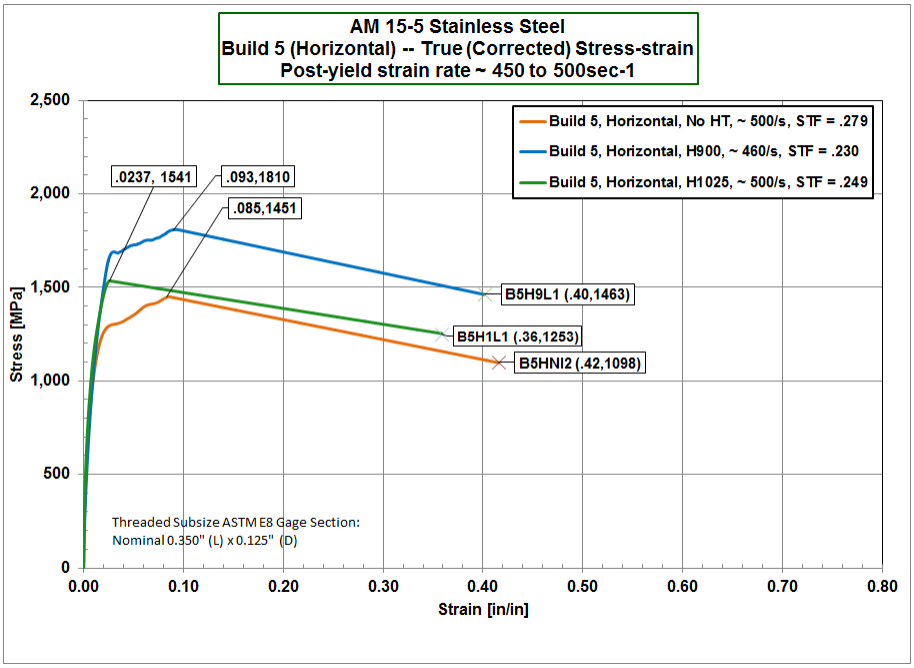

Figure 46. Build 5, Momentum Trap SHB Tension Test, True Stress-Strain, Mid Rate

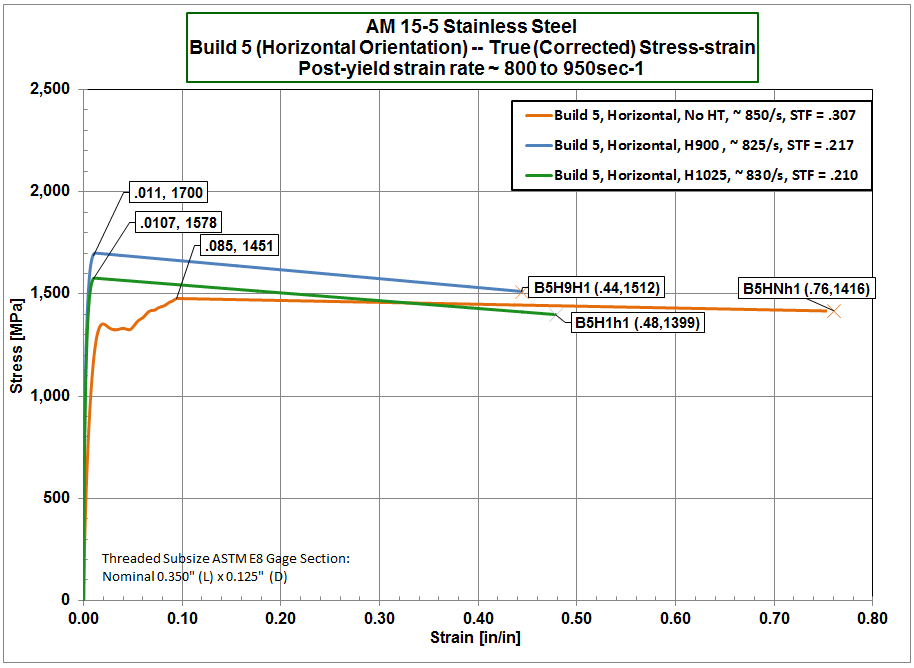

Figure 47. Build 5, Momentum Trap SHB Tension Test, True Stress-Strain, High Rate

4.7 Results Conclusion

The unknown reason for the variation in composition for builds 1 and 2 is a large concern, but the material properties for the remaining builds are considered representative of the 15-5PH stainless steel AM desired. There is some natural variation between the builds, but in general the samples from the same build and orientation agreed were within 7% of each other, the same amount that the samples across builds and orientation typically displayed. The largest disparity was actually within builds, the horizontal orientation of build 4 and build 5 were often 7% to 10% greater than the corresponding vertical orientation.

V Conclusions and Recommendations

5.1 Chapter Overview

This chapter consists of two sections, the first summarizes the conclusions reached in pursuit of this thesis. The overarching goal was to determine how AM 15-5PH stainless steel performs under dynamic load conditions. The main test variables were build orientation, heat treatment, and strain rate. The method of manufacture was the same throughout the builds so that a natural variation in properties over time could be accounted for. A total of 18 compression, 12 quasi-static, and 89 tension SHB specimens were machined from cylinders formed in a total of 5 production runs on a EOSINT M 280 DMLS operated by a commercial vendor. The specimens were formed using two different build orientations and two heat treatment conditions in addition to the non-heat treated condition. All heat treatments were performed in accordance with the H900 or H1025 protocols specified in AMS-H-6875B and listed in Appendix A.

The second section presents recommendations for future study. It encompasses concepts that were either out of scope of this thesis, or presented as unknowns relevant to using AM material under dynamic loading conditions. A considerable amount of future research is needed to understand the dynamic performance of AM material produced under a variety of conditions and parameters. Work is also required to predict and improve the material characteristics.

5.2 Conclusions

The tests performed accomplished the overall goal. Examination of the microstructure of the samples and execution of quasi-static testing established a baseline for the material. Data collected on the crystallographic phases and orientations

present in the samples allowed understanding of how the microstructure is affected by the AM process. Quasi-static testing established the link between microstructure and performance and enabled comparison to wrought material standards. Dynamic testing in compression and tension on two SHB setups demonstrated the dynamic performance of the material and ascertained the range of natural variation between material of separate builds. The variables tested show the resultant difference in build orientation, heat treatment, and strain rate sensitivity. Utilizing the results, and heeding the lessons learned, enables future use of 15-5PH AM material in more critical applications.

5.2.1 Material Performance

The materials tested quasi-statically, with the exception of build 2, tended to perform at the top end or higher than the EOS reported strength and ductility values [2]. Table 7 shows that builds 3 through 5 exceeded the reported standards for the wrought material [1] in almost every case except for a significantly lower average modulus. The material stiffness, measured by the modulus, is on the order of 10% lower than the wrought material. A material with a lower moduls than expected will elastically deform more easily than a stiffer material, resulting in unforseen consequences in some applications. However, the test results also indicate increased ductility, so the lower modulus does not result in a decrease in toughness, measured by the area under the true stress-strain curve.

5.2.2 Strain Rate Sensitivity

Testing at a mid and high rate enabled determination of the material's strain rate sensitivity. Comparing the results of the momentum trap SHB tests at the two rates shows a definite trend of strain softening at both of the elevated strain rates

Table 7. Experimental Tensile Test Results Comparison to Wrought [1] and AM Manufacturer [2] Data

As Built:	Ultimate Tensile Strength (MPa)	0.2% Yield Strength (MPa)	Strain To Failure (in/in)	Modulus (Msi)
EOS (Horiz)	1150 ± 50	1050 ± 50	.16 ± .04	
EOS (Vert)	1050 ± 50	1000 ± 50	.17 ± .04	
AK Steel (Long)	1116	985	0.084	28.5
AK Steel (Transverse)	1110	965	0.076	28.5
Present Study (Horiz)	1230	795	0.24	18.5
Present Study (Vert)	1205	890	0.21	21.55
H900:				
EOS (Horiz & Vert)	1450 ± 100 (typ)	1300 ± 100 (typ)		
AK Steel (Long)	1441	1172	0.084	28.5
AK Steel (Transverse)	1468	1172	0.076	28.5
Present Study (Horiz)	1560	1215	0.215	24.4
Present Study (Vert)	1530	1460	0.170	26.1
H1025:				
AK Steel (Long & Trans)	1200	1179	0.1075	28.5
Present Study (Horiz)	1430	1187	0.255	25
Present Study (Vert)	1490	1414	0.18	25.9

used. The corresponding quasi-static true stress-strain curves, however, show strain hardening. The phenomena producing the strain softening behavior is linked to the elevated strain rate. Subjecting the specimen to a quick, violent tensile pulse is significantly different at a microstructure level than the slow 0.001 s_{-1} quasi-static pull. Specimens subjected to the mid rate appeared to undergo a steeper curve of

strain softening, which seems counter-intuitive as the energy for the higher rate is greater. The dynamic force is not allowing slow, plastic deformation, and instead the major part of the deformation energy is transformed to heat while the rest is used by the material to cover the increase of internal energy [31]. These inertial and thermal forces induced from the high strain rates are likely a large part of the strain softening effect.

5.2.3 Build Orientation

In general, a slight effect of build orientation was noted. Quasi-static tests conducted on build 4 show typically about 4% more elongation for the horizontal build orientation. The elongation at both orientations beat the published STF values for wrought material by more than 4%. At the mid and high strain rates the horizontal build orientation also often had higher ductility than the vertical. However, the difference was not significant enough in all cases to conclude a substantial build orientation bias or anisotropy effect.

5.2.4 Heat Treatment

The heat treatments used appeared to have the desired effect upon the martensitic builds 3 through 5. The precipitate is so small it is not detectable via the spectroscopy methods used, but the effects of the aging process were evident during the tests. A 25% to 30% increase in UTS of the AM material upon H900 heat treatment is a reasonable result when compared to the wrought material response. The quasi-static and dynamic tension tests for the martensitic builds all displayed an increase in strength at or near that range. The 7% to 10% UTS increase for the tested H1025 heat treatment AM samples also matches the wrought behavior. EBSD scans of the heat treated specimens show no additional change in the microstructure, therefore

the change in test results is assumed to be directly attributable to the precipitation hardening effect. The specimens with a large amount of retained austenite in build 2 did not show any increased UTS with heat treatment, although the ductility was slightly changed.

5.2.5 Material Composition

The results of the tests conducted demonstrate the need to either have tight process control or strict quality control checks. One of the builds, build 2, did not meet the AISI 15500 specifications. The build underperformed in every material property category but STF when compared to the wrought standards. Upon examination, the composition and crystalline structure was completely different than expected. However, this build was supposed to be manufactured with the same process, parameters, and powder used in the other builds. The quasi-static and compression test results confirm the variation from the desired crystalline structure. The poor performance of the material and lack of indication prior to test are a potential safety issue; if the precipitation hardened version of the martensitic material is expected in a final part, build 2 would fail quickly.

5.2.6 Thermal Gradients and Residual Stresses

Build 3 compared favorably to the published values even though the manufactured cylinders experienced distortion during the build. It is not known if the warping actually affected the test results. Machining the tension specimens mitigated the observable dimensional warping, and may have released some of the residual stress. Machining also negated edge effects and allowed the specimens to fit into the testing apparatus and accomplish all desired testing. The occurrence, however, illustrates the AM method can cause uneven heating and cooling dictated by the geometry

of the build itself. The result is unexpected thermal gradients and residual stresses. Proper pre-planning and support to the AM structure lessen the effect, if not mitigate it entirely. The effect of geometry instability is a factor in future certification and suitabilty requirements.

5.2.7 Test Setup

The test setup is an important parameter in the final results. The specimens tested on the reflected wave SHB were consistent, typically within 6% of each other. However, those results were uniformly below those found for the same build using the momentum trap SHB apparatus. The comparison between the build 3 SHB tension tests is shown in Figure 59 in Appendix D. The curves produced from the reflected wave SHB using the collared specimen are much noisier and lower than the curves from the momentum trap SHB. The difference likely stems from the initial compression wave through the collar actually impacting the specimen or how the wave traverses the threaded ends of the specimens themselves. Regardless of the reason, future work should consider reconciling the two and determining how the values returned for a uniaxial load case relate to the complex loading present in a uncontrolled dynamic loading event.

5.3 Future Work

5.3.1 Material Performance

The results found in this test lay the foundation for evolution of modelling constants specifically for this material. Replicating the tests at varying temperatures and noting trends in the behavior as the temperature is increased from room temperature could combine this work to produce the full Johnson-Cook equation. The ability to model the exact AM material of interest is valuable to finite element modeling and

simulations of dynamic loading and fracture. Having an equation that explains the precise material of interest enables better AM design, facilitating insight into where the AM material may differ from standard material and need additional support.

5.3.2 Strain Rate Sensitivity

The work described in this thesis was a first foray into whether or not there was significant strain rate sensitivity noted for two very different rates. Given the results of the strain softening effects, there is potential for future work thoroughly exploring the strain softening effect noticed in the tests. One possible method is repeating the tension tests for a single build through a range of strain rates on a SHB apparatus that allows digital image correlation. Not only would this precisely replicate the curves, it would also show the complex elastic-plastic deformation as the specimen deforms through the upper and lower yield points, a source of non-linear behavior observed in the stress-strain curves.

5.3.3 Build Parameters

In the work presented, the main build parameter studied was build orientation. However, there is a growing body of work that describes the effects of changing the AM parameters and build geometry. Future work could encompass a host of unknowns in how changes in build environment affect the final part; everything from the humidity in the air to the scan pattern of the laser can affect the solidification of the AM part. Additionally, it is apparent from a literature review the material properties of thin walled geometries are a source of variation. Understanding the effect upon thin walls and ascertaining the influence of edge effects on complex geometries that cannot undergo machining or final finishing would provide valuable information.

5.3.4 Material Composition

Although the final three builds are considered most relevant to the original intention of this work since they possess the desired composition, the first two builds are still of interest. It would be useful to investigate possible causes of the compositional deviation in future research. Inducing changes in composition could yield important insight into the AM process for this material. If the retention of austenite is directly resultant from operating conditions or contamination, avoidance of these issues could limit the flexibility of the process or make it more costly. If the variation is linked to the parameters of the manufacturing recipe, awareness of potential outcomes enables optimization for better or more consistent results.

5.3.5 Thermal Gradients and Residual Stresses

Residual stress affecting the test results was not anticipated with the cylindrical geometry used. One lesson learned is that even simple geometries can experience thermal gradients with AM processes if not preplanned properly. Designing for AM processes is more complex than a simple substitution for wrought material in the same form, so there is opportunity to explore design parameters for some desired final geometries. Building a knowledge base of how the build parameters affect the thermal properties and determining the optimal solidification process or post processing options paves the way for future utilization of the technology. Scalability is becoming a higher concer as the capability to create larger parts grows, but ensuring a stable process is going to rely upon knowledge of methods of avoiding residual stresses. Future work developing methods of optimizing complex geometry build sequencing, exploring and scaling lattice constructs, or proper support of enclosed internal structures would prove valuable to the continued investigation of using AM to produce complex parts.

5.4 Summary

The investigation of additive manufacturing holds great promise and will provide remarkable opportunities for innovation in aerospace applications once the variables are better understood. This work contributes to building that knowledge base by investigating the range of dynamic properties gathered from multiple builds of AM 15-5PH stainless steel produced in the same manner. The conclusions reached include the observation of a microstructure dominated by the method of manufacture which contributes to some variation from the wrought properties. Most noticeable is an increased ductility and decreased modulus of elasticity with similar strength characteristics for the material with the desired crystalline structure. Therefore, the AM part is expected to exceed the toughness of the wrought material, with slightly less stiffness in the elastic region. The knowledge gathered in this study are directly applicable to the applications of interest by instituting an expected mechanical performance range, uncovering some undesirable effects and suggesting ways to detect or mitigate them, and laying the groundwork for derivation of modeling parameters. Further understanding of how the tested properties relate to final parts under dynamic loads, more development of modeling tools, and production of better analysis tools will further facilitate optimization of AM part design to achieve desired mechanical properties.

Appendix A. 15-5PH Stainless Steel Heat Treatment Protocols

See next page.

Table 8. Heat Treatment Protocols [3]

Condition	Heat To ±15°F (8.4°C	Time at Temp (hrs)	Type of Cooling
H900	900°F (482°C)	1	Air
H925	925°F (496°C)	4	Air
H1025	1025°F (551°C)	4	Air
H1075	1075°F (580°C)	4	Air
H1100	1100°F (593°C)	4	Air
H1150	1150°F (621°C)	4	Air
H1150+H1150	1150°F (621°C)	4 followed by	Air
	1150°F (621°C)	4	Air
H1150M	1400°F (760°C)	2 followed by	Air
	1150°F (621°C)	4	Air

Appendix B. Design of Tests: Quasi-Static, Compression SHB, and Tension SHB

See next page.

Table 9. Build orders

Build	Build 1	Build 2	Build 3	Build 4	Build 5
Vertical	15	30	0	15	15
Horizontal	0	0	30	15	15

Table 10. Quasi-static test plan

Specimen Type	Build 2 (Vertical)	Build 3 (Horizontal)	Build 4 (Vertical)	Build 4 (Horizontal)
Non-heat treated	1	1	1	1
H900	1	1	1	1
H1025	1	1	1	1

Table 11. Compression SHB test plan

	Build 1 (Vertical)		Build 3 (Horizontal)	
Specimen Type	Mid ($\approx 400\frac{1}{s}$)	High($\approx 850\frac{1}{s}$)	Mid ($\approx 400\frac{1}{s}$)	High ($\approx 850\frac{1}{s}$)
Non-heat treated	3	3	3	3
H900	3	3	3	3
H1025	3	3	3	3
Total	18		18	

Table 12. Direct Tension SHB test plan

Specimen Type	Vertical						Horizontal					
Rate	Mid ($\approx 400\frac{1}{s}$)			High($\approx 850\frac{1}{s}$)			Mid ($\approx 400\frac{1}{s}$)			High($\approx 850\frac{1}{s}$)		
Build	**2**	**4**	**5**	**2**	**4**	**5**	**3**	**4**	**5**	**3**	**4**	**5**
Non-heat treated	1	1	1	1	1	1	1	1	1	1	1	1
H900	1	1	1	1	1	1	1	1	1	1	1	1
H1025	1	1	1	1	1	1	1	1	1	1	1	1
Total	3	3	3	3	3	3	3	3	3	3	3	3
	18						18					

Appendix C. EDS Results

See next page.

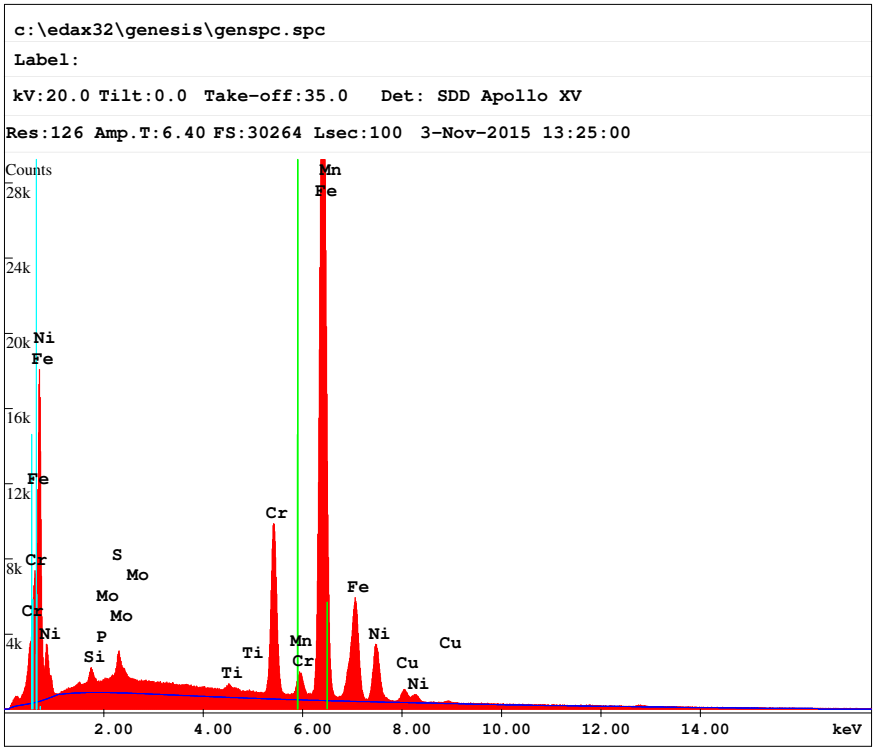

EDAX ZAF Quantification (Standardless)
Element Normalized
SEC Table : Default

Element	Wt %	At %	K-Ratio	Z	A	F
SiK	0.84	1.67	0.0041	1.1163	0.4324	1.0021
P K	0.48	0.87	0.0029	1.0908	0.5487	1.0036
MoL	3.92	2.29	0.0279	0.9019	0.7872	1.0010
S K	0.00	0.00	0.0000	1.1242	0.6568	1.0042
TiK	0.64	0.75	0.0067	0.9999	0.9537	1.0929
CrK	10.10	10.88	0.1158	0.9988	0.9803	1.1717
MnK	0.44	0.45	0.0043	0.9817	0.9888	1.0107
FeK	71.72	71.96	0.7119	1.0011	0.9772	1.0145
NiK	9.26	8.83	0.0849	1.0188	0.9001	1.0000
CuK	2.60	2.29	0.0232	0.9715	0.9206	1.0000
Total	100.00	100.00				

Figure 48. Typical Build 1 EDS

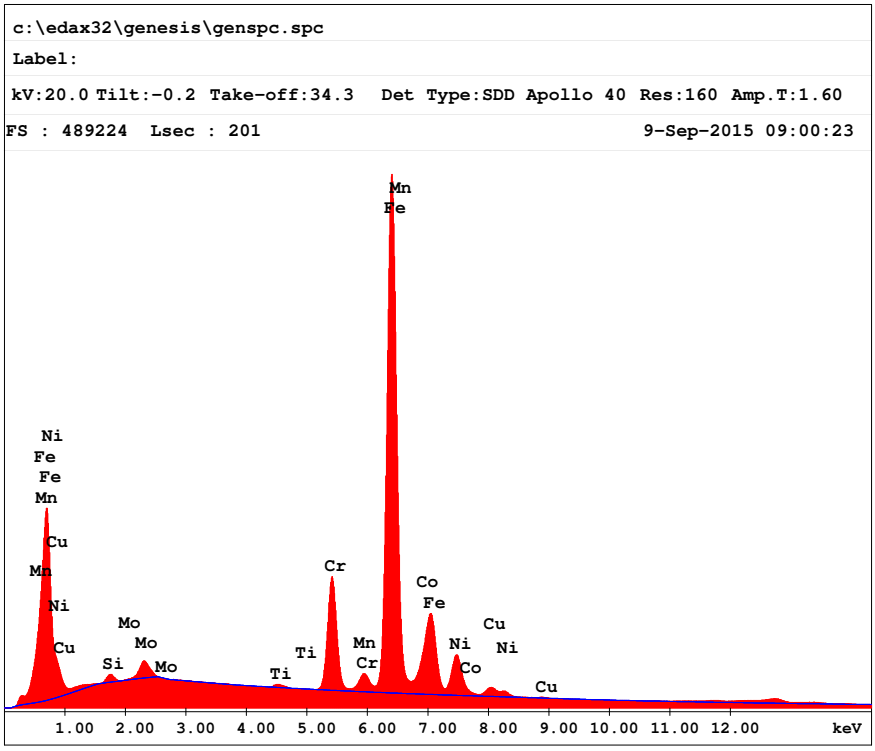

EDAX ZAF Quantification (Standardless)
Element Normalized
SEC Table : Default

Element	Wt %	At %	K-Ratio	Z	A	F
SiK	0.49	0.97	0.0023	1.1168	0.4191	1.0015
MoL	1.92	1.12	0.0135	0.9022	0.7799	1.0009
TiK	0.22	0.25	0.0023	1.0004	0.9578	1.0989
CrK	9.18	9.92	0.1074	0.9992	0.9840	1.1897
MnK	0.47	0.48	0.0047	0.9821	0.9917	1.0272
FeK	70.48	70.94	0.7023	1.0015	0.9809	1.0143
CoK	5.87	5.59	0.0571	0.9823	0.9870	1.0036
NiK	8.84	8.46	0.0813	1.0191	0.9021	1.0000
CuK	2.55	2.26	0.0227	0.9718	0.9161	1.0000
Total	100.00	100.00				

Figure 49. Typical Build 2 EDS

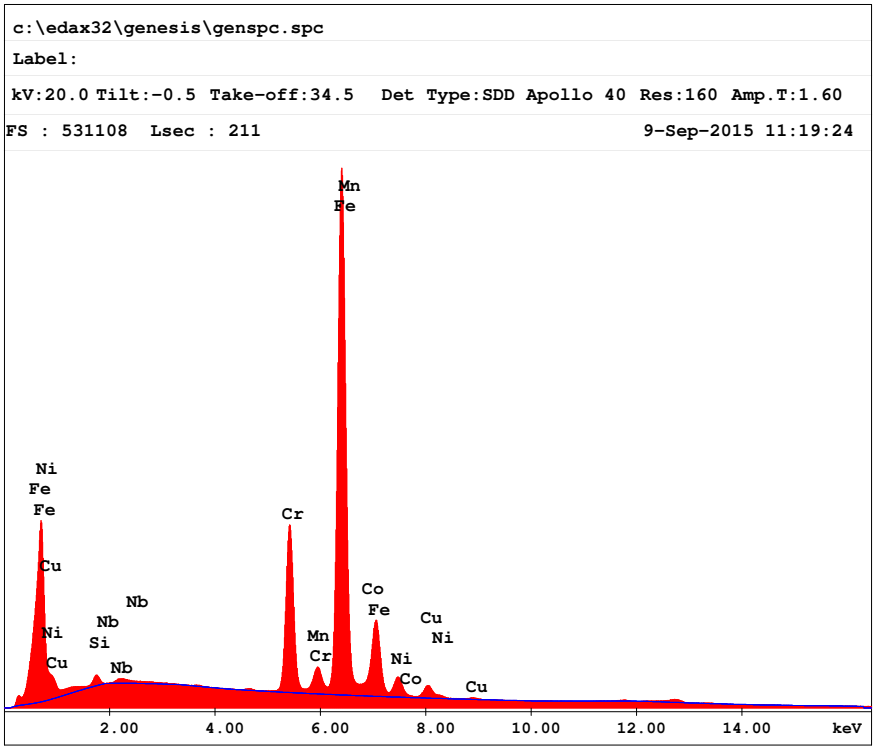

EDAX ZAF Quantification (Standardless)
Element Normalized
SEC Table : Default

Element	Wt %	At %	K-Ratio	Z	A	F
SiK	0.67	1.31	0.0032	1.1163	0.4251	1.0014
NbL	0.55	0.33	0.0037	0.9104	0.7380	1.0010
CrK	13.94	14.86	0.1623	0.9984	0.9877	1.1808
MnK	0.73	0.74	0.0072	0.9812	0.9947	1.0139
FeK	73.44	72.94	0.7229	1.0006	0.9749	1.0090
CoK	2.59	2.44	0.0251	0.9814	0.9818	1.0048
NiK	4.51	4.26	0.0411	1.0180	0.8951	1.0000
CuK	3.57	3.12	0.0317	0.9707	0.9138	1.0000
Total	100.00	100.00				

Figure 50. Typical Build 3 EDS

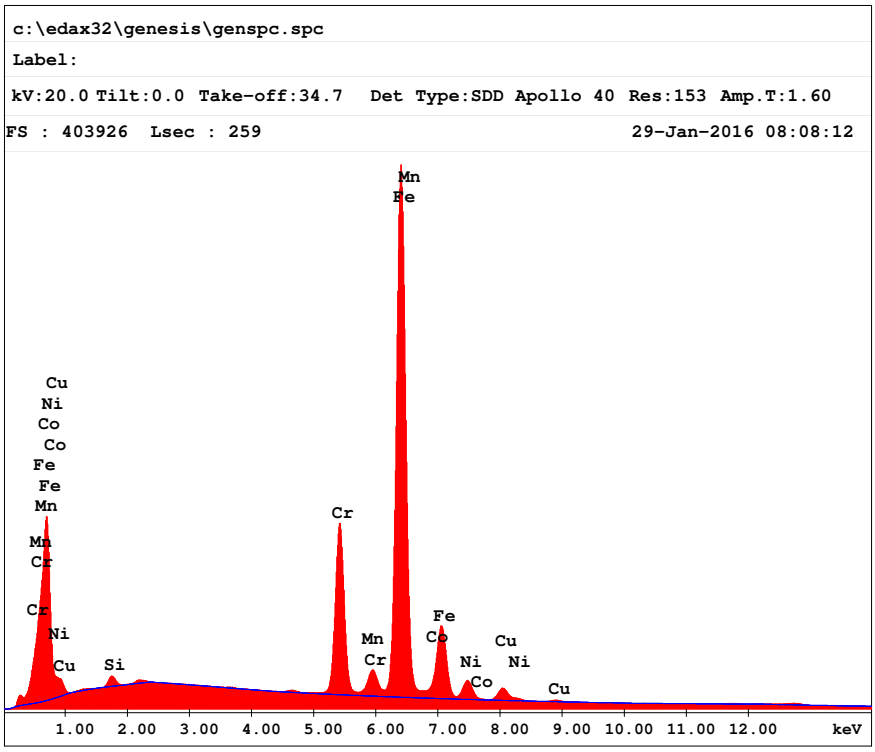

EDAX ZAF Quantification (Standardless)
Element Normalized
SEC Table : Default

Element	Wt %	At %	K-Ratio	Z	A	F
SiK	0.63	1.24	0.0030	1.1157	0.4261	1.0013
CrK	14.35	15.26	0.1676	0.9978	0.9888	1.1839
MnK	0.51	0.52	0.0051	0.9806	0.9955	1.0104
FeK	75.34	74.60	0.7408	1.0000	0.9749	1.0086
CoK	1.44	1.35	0.0139	0.9807	0.9821	1.0047
NiK	4.27	4.02	0.0388	1.0174	0.8935	1.0000
CuK	3.46	3.01	0.0306	0.9700	0.9136	1.0000
Total	100.00	100.00				

Figure 51. Typical Build 4 EDS

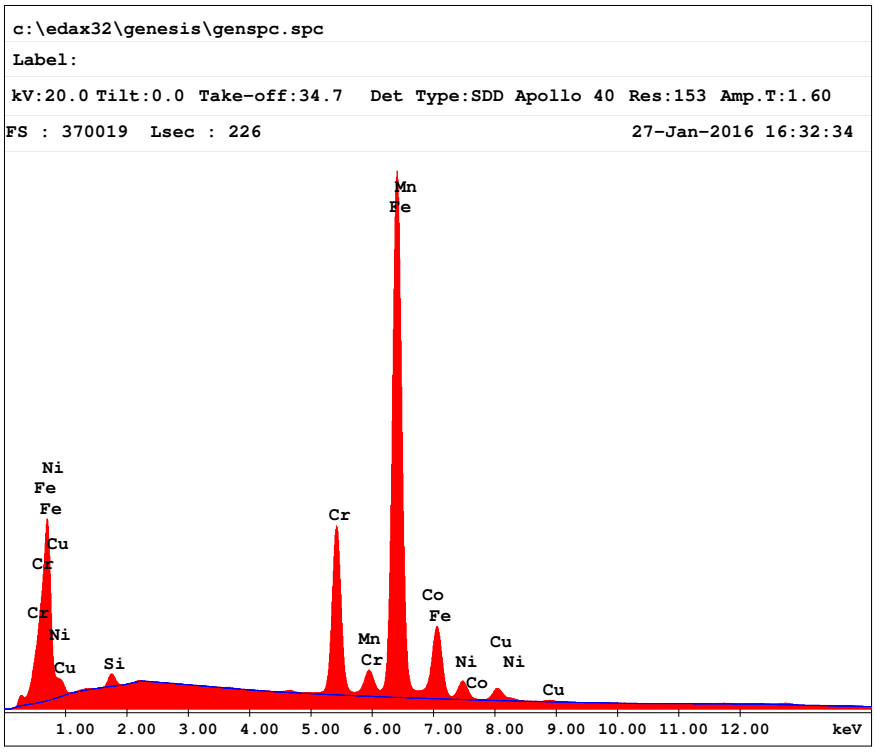

EDAX ZAF Quantification (Standardless)
Element Normalized
SEC Table : Default

Element	Wt %	At %	K-Ratio	Z	A	F
SiK	0.76	1.50	0.0036	1.1156	0.4267	1.0013
CrK	14.29	15.18	0.1669	0.9977	0.9887	1.1839
MnK	0.54	0.55	0.0054	0.9805	0.9954	1.0110
FeK	75.12	74.30	0.7385	0.9998	0.9750	1.0084
CoK	1.67	1.57	0.0162	0.9806	0.9821	1.0047
NiK	4.16	3.91	0.0378	1.0172	0.8938	1.0000
CuK	3.45	3.00	0.0306	0.9699	0.9137	1.0000
Total	100.00	100.00				

Figure 52. Typical Build 5 EDS

Appendix D. Test Results: Quasi-Static, Compression SHB, Indirect and Direct Tension SHB

See next page.

4.1 Quasi-Static Test Results

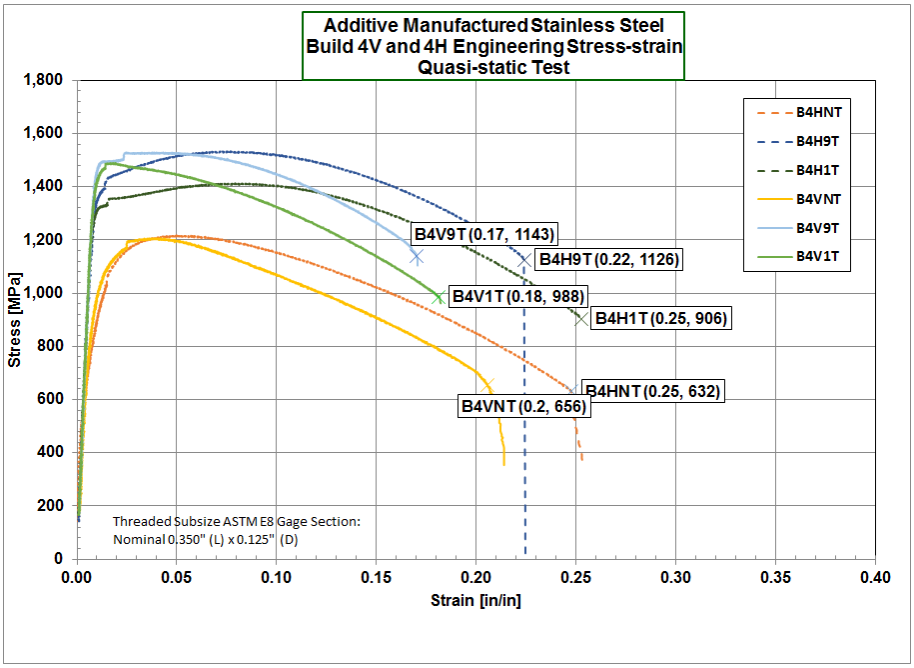

Figure 53. Builds 4V and 4H, Quasi-static Tension Test, Engineering Stress-Strain

Table 13. Quasi-Static Test Results: Builds 2,3,4V,4H all HT

		UTS (MPa)	0.2% YS (MPa)	STF (in/in)	Elong %	Modulus (Msi)
Quasi-Static Test	B2 V NoHT	1078.30	901.60	0.3336	33.36	22.62
	B2 V H900	1084.99	906.89	0.3121	31.21	19.73
	B2 V H1025	1093.85	878.32	0.29	28.96	19.55
	B3 H No HT	1240.43	693.61	0.2205	22.05	15.47
	B3 H H900	1585.19	1100.17	0.2069	20.69	23.80
	B3 H H1025	1450.46	1079.03	0.2574	25.74	25.18
	B4 V No HT	1205.81	890.80	0.2139	21.39	21.55
	B4 V H900	1529.26	1462.79	0.1706	17.06	26.07
	B4 V H1025	1490.41	1414.12	0.1822	18.22	25.87
	B4 H No HT	1218.25	698.78	0.2531	25.31	21.52
	B4 H H900	1532.04	1332.62	0.2240	22.40	25.04
	B4 H H1025	1414.79	1296.21	0.2525	25.25	24.80
AK Steel [1]	Cond A (L)	1110.06	965.27	0.0840	8.40	28.50
	H900 (L)	1441.00	1385.85	0.1010	10.10	28.50
	H1025 (L)	1199.69	1179.00	0.1220	12.20	28.50
	Cond A (T)	1116.95	985.95	0.0760	7.60	28.50
	H900 (T)	1468.58	1392.74	0.0940	9.40	28.50
	H1025 (T)	1206.58	1179.00	0.0930	9.30	28.50
MIL-HBK 5H [3]	H900 (L)	1310.00	1172.11	0.10	10.00	28.50
	H900 (T)	1172.11	1172.11	0.06	6.00	28.50
	H1025 (L)	1068.69	999.74	0.12	12.00	28.50
	H1025 (T)	999.74	999.74	0.08	8.00	28.50

4.2 Compression Test Results

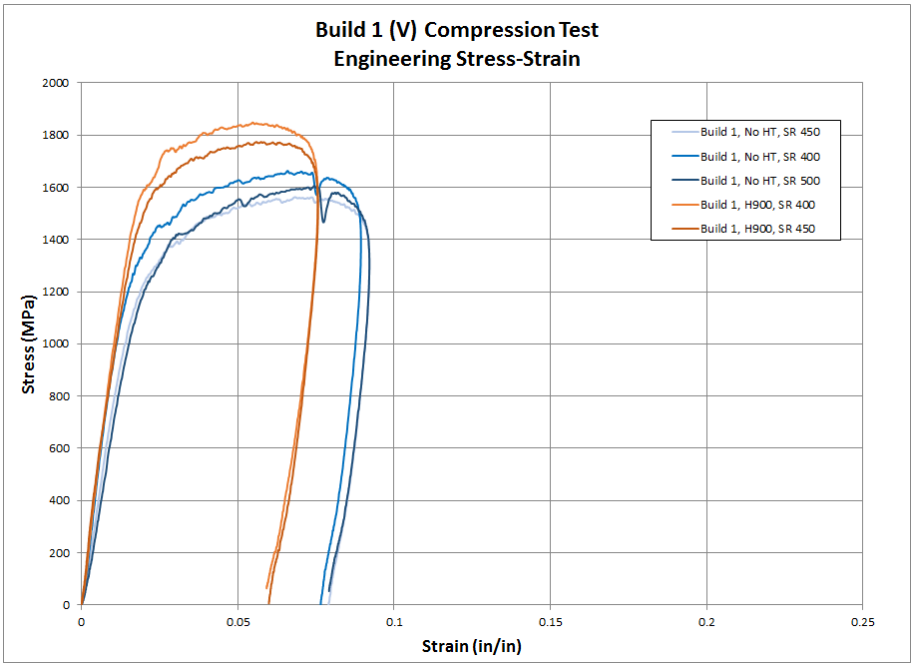

Figure 54. Build 1, Compression SHB Test, Engineering Stress-Strain

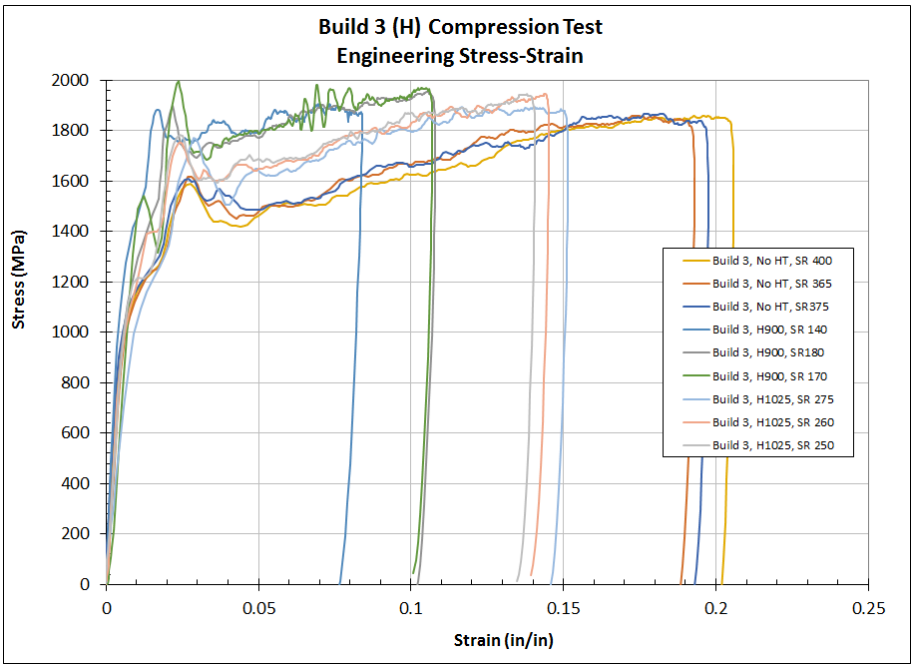

Figure 55. Build 3, Compression SHB Test, Engineering Stress-Strain

Table 14. Compression SHB, Builds 1 and 3

Build	Condition	UCS (MPa)	0.2% Offset Yield (MPa)	Modulus (GPa)
Build 1	No HT	1463.57	1064.20	76.0
	H900	1519.62	1123.33	84.3
Build 3	No HT	1560.26	1111.97	199.9
	H900	1884.62	1309.62	204.1
	H1025	1722.98	1116.11	164.2

4.3 Indirect Tension Tests

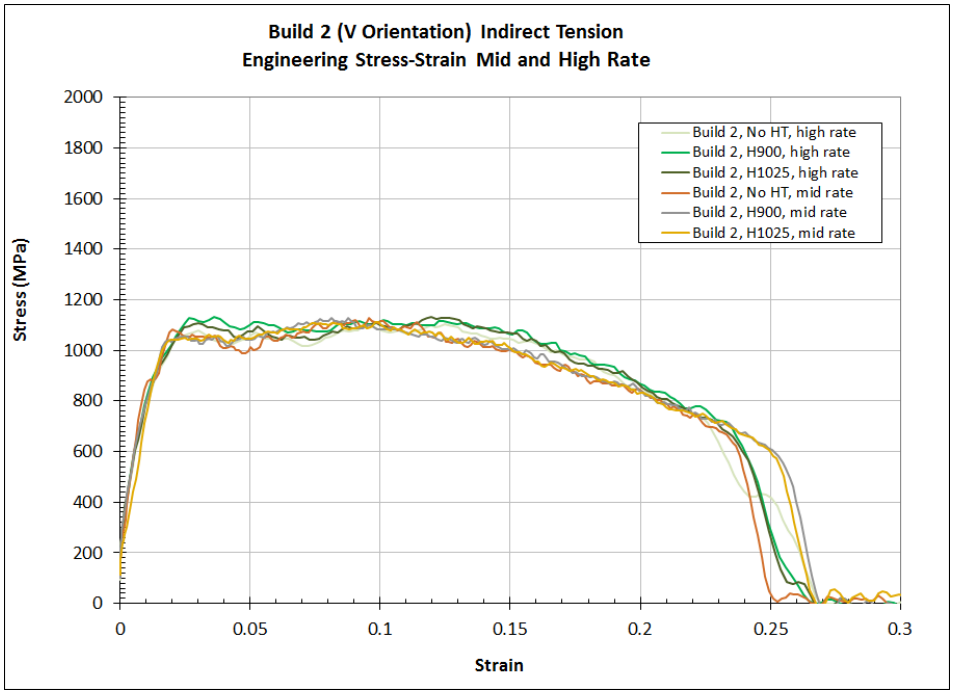

Figure 56. Build 2, Indirect Tension SHB Test, Mid $\approx 450\frac{1}{s}$ and High Rate $\approx 800\frac{1}{s}$ Engineering Stress-Strain

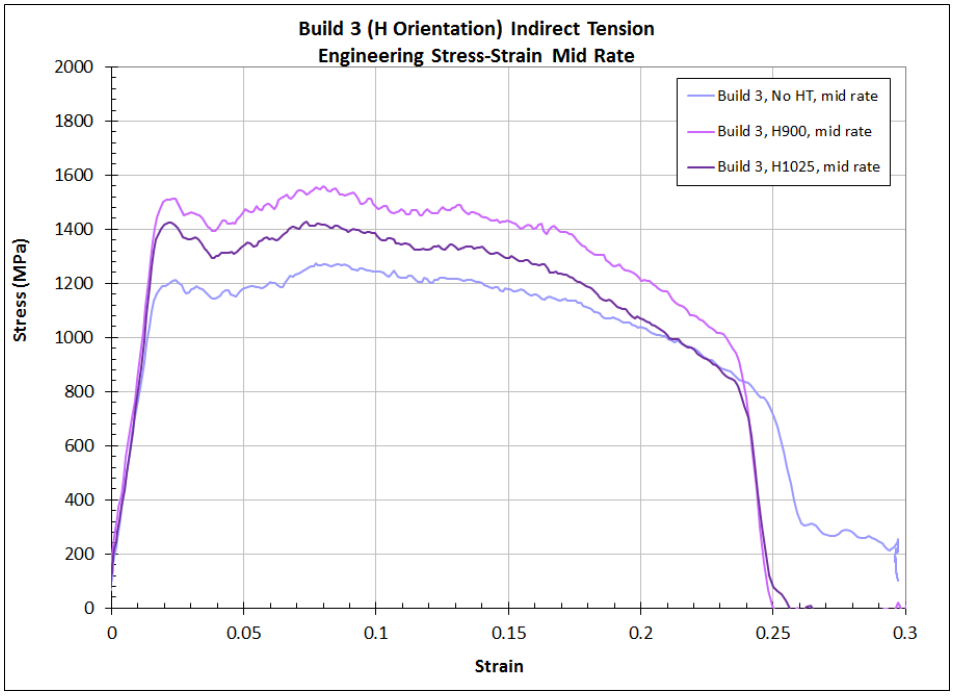

Figure 57. Build 3, Indirect Tension SHB Test, Mid Rate $\approx 450\frac{1}{s}$ Engineering Stress-Strain

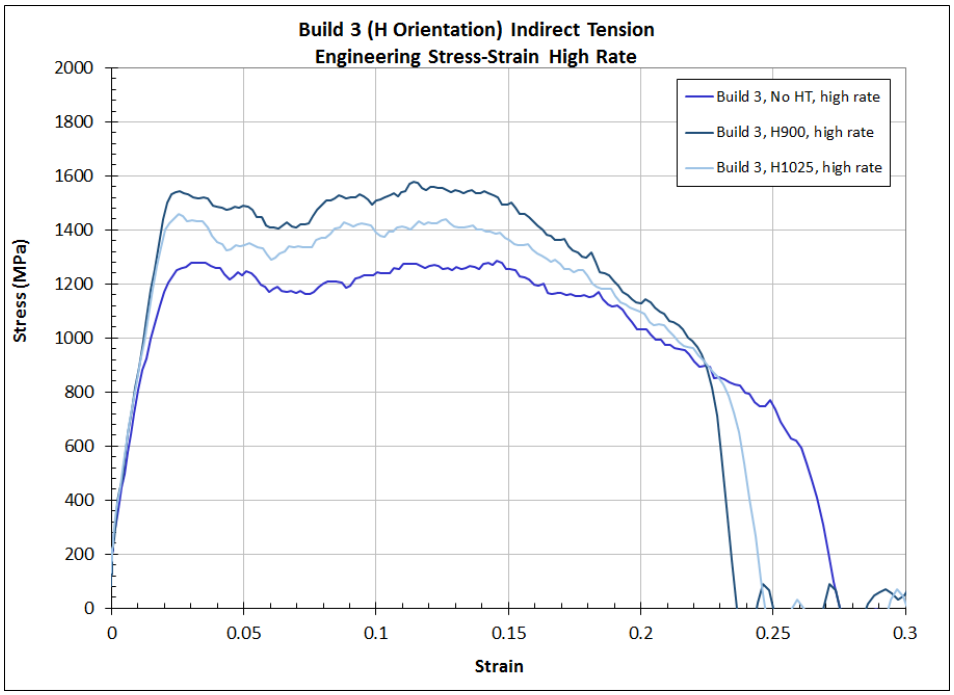

Figure 58. Build 3, Indirect Tension SHB Test, High Rate $\approx 800\frac{1}{s}$ Engineering Stress-Strain

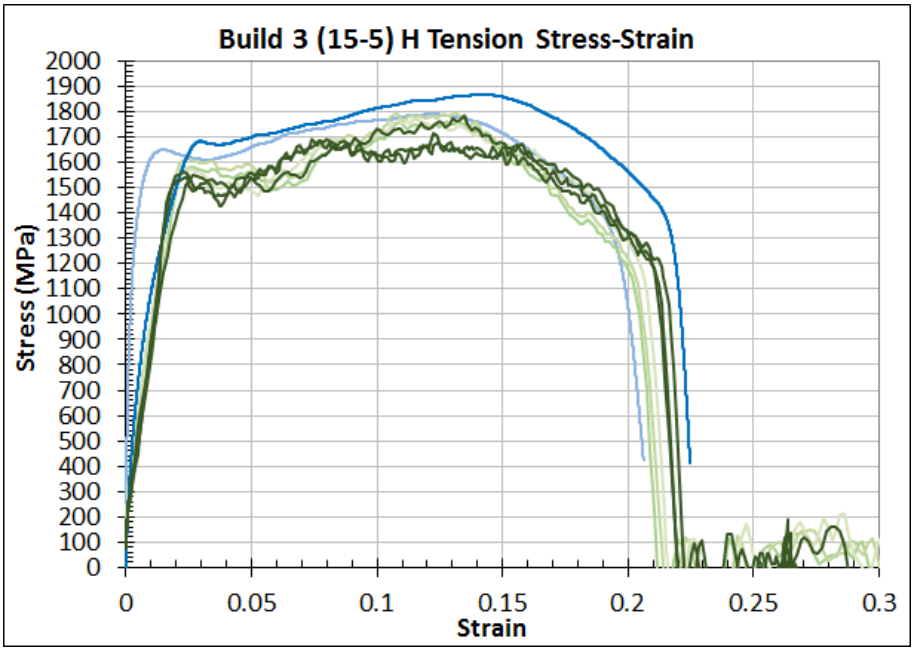

Figure 59. Example of Comparison of Stress-Strain Curves from Reflected Wave (green) and Momentum Trap (blue) SHB tests

Bibliography

1. AK Steel, "15-5PH Stainless Steel Product Data Bulletin," April 22, 2014.

2. i3DMFG, "EOS Stainless Steel PH1 for EOSINT M 270," 2008.

3. AFLR/MLSC, "Military handbook: Metallic materials and elements for aerospace vehicle structures," Tech. Rep. MIL-HDBK-5H, AMSC, 1 December 1998.

4. J. Freeman, G. P. Paoli, Q. Ladetto, G. L. D. Benedetto, R. R. John Erkoyuncu, S. Williams, P. Colegrove, F. Martina, and A. Busachi, "Additive Manufacturing and Obsolescence Management in the Defence Context," *RAND Europe PE-171-AST*, 2015.

5. AF/ST, "Global Science and Technology Vision," Tech. Rep. TR 13-01, United States Air Force, 21 June 2013.

6. I. W. Gibson, D. W. Rosen, and B. Stucker, *Additive Manufacturing Technologies: 3D Printing, Rapid Prototyping, and Direct Digital Manufacturing*. SpringerLink : Bücher, Springer New York, 2014.

7. M. E. Chenoweth, J. Arkes, and N. Y. Moore, "Best Practices in Developing Proactive Supply Strategies for Air Force Low-Demand Service Parts," *RAND Corporation*, 2010.

8. "EOS StainlessSteel PH1 for EOSINT M270," 2015.

9. RDECOM Public Affairs, "3-D Printed Metals May Transform Army Logistics," *Army Technology Magazine*, pp. 1–13, 2014.

10. T. T. Wohlers and T. Gornet, *History of Additive Manufacturing: State of the Industry.* Fort Collins, CO: Wohlers Associates, 2014.

11. J. Gordon, "3-d printer creates models that save time, money," *Robins Air Force Base Public Affairs*, 2015.

12. J. Parker, "Planning a larger role for 3-d printing," *Tinker Air Force Base Public Affairs*, 2015.

13. www.3ders.org, "The FAA Cleared the First 3D Printed Part to Fly in a GE Commercial Jet Engine," *www.3ders.org*, 16 April 2015. http://www.3ders.org/articles/20150416-the-faa-cleared-the-first-3d-printed-part-to-fly-in-a-ge-commercial-jet-engine.html.

14. www.3ders.org, "China Developing World's Largest 3D Printer, Prints 6m Metal Parts in one Piece," *www.3ders.org*, 7 February 2014. http://www.3ders.org/articles/20140207-china-developing-world-largest-3d-printer–prints-6m-metal-parts-in-one-piece.html.

15. S. Kalpakjian, *Manufacturing Engineering and Technology.* Reading, MA: Addison-Wesley Publishing Company, 1995.

16. J. Davis and A. Committee, *Stainless Steels.* ASM specialty handbook, ASM International, 1994.

17. A. Hall, A. Hoenie, and C. Slunder, "Thermal and mechanical treatment for precipitation-hardening stainless steels," Tech. Rep. Volume NASA-SP-5089, NASA Special Publication, 1967.

18. A. Hoenie and D. Roach, "New developments in high-strength stainless steels," Tech. Rep. Report 233, Defense Metals Information Center, January 3, 1966.

19. S. Cheruvathur, E. A. Lass, and C. E. Campbell, "Additive Manufacturing of 17-4 PH Stainless Steel: Post-processing Heat Treatment to Achieve Uniform Reproducible Microstructure," *Journal of Minerals, Metals, and Materials*, pp. 1–13, 2015.

20. W. W. Chen and B. Song, *Split Hopkinson (Kolsky) Bar: Design, Testing and Applications*. Mechanical Engineering Series, New York: Springer US, 2011.

21. ASM International Handbook Committee, ed., *ASM handbook: Heat treating of Stainless Steels*, vol. 2 of *ASM Handbook*. ASM International, 8 ed., 1964.

22. D. Briggs, J. Brady, and B. Newton, "Scanning Electron Microscopy and X-Ray Microanalysis," 2000.

23. J. Heath and N. Taylor, eds., *Essential Knowledge Briefings: Energy Dispersive Spectroscopy*. Microscopy and Analysis, West Sussex: John Wiley & Sons Ltd, second ed., 2015.

24. Oxford Instruments, *EBSD Explained from Data Acquisition to Advanced Analysis*. Oxfordshire, England: Oxford Instruments plc, 2015.

25. R. Hoffman, "Johnson-cook material constants for treated 4130 steel," Tech. Rep. UDR-TR-2014-xx, Air Force Institute of Technology, 2014.

26. M. Sasso, M. Costanzi, G. Newaz, and D. Amodio, eds., *Determining True Stress-Strain Curve by Dynamic Tensile Tests*, 2004.

27. N. E. Dowling, *Mechanical Behavior of Materials: Engineering Methods for Deformation, Fracture, and Fatigue*. McGraw-Hill Series in Materials Science and Engineering, New Jersey: Prentice Hall, 1999.

28. J. Nunes, "Flow stress-strain relationships in tension tests of steel," Tech. Rep. WAL TR 834.2/10, Watertown Arsenal Laboratories, 1963.

29. P. W. Bridgman, *The Stress Distribution at the Neck of a Tension Specimen, Transactions*, vol. 32. New Jersey: ASM, 1944.

30. J. D. Verhoeven, *Steel Metallurgy for the Non-Metallurgist*. Materials Park, OH: ASM International, 2007.

31. E. El-Magd, "Mechanical Properties at High Strain Rates," *Journal de Physique IV*, vol. 4, pp. C8–149–C8–170, 1994. ¡10.1051/jp4:1994823¿.

32. Allegheny Technologies Incorporated, "ATI15-5 Technical Data Sheet," March 15, 2012.

REPORT DOCUMENTATION PAGE

Form Approved
OMB No. 0704–0188

1. REPORT DATE *(DD–MM–YYYY)*	2. REPORT TYPE	3. DATES COVERED *(From — To)*
03–26–2016	Master's Thesis	Sept 2014 — Mar 2016

4. TITLE AND SUBTITLE

DYNAMIC PROPERTIES OF ADDITIVELY MANUFATURED 15-5PH STAINLESS STEEL

5a. CONTRACT NUMBER

5b. GRANT NUMBER

5c. PROGRAM ELEMENT NUMBER

6. AUTHOR(S)

Allison A. Dempsey

5d. PROJECT NUMBER

5e. TASK NUMBER

5f. WORK UNIT NUMBER

7. PERFORMING ORGANIZATION NAME(S) AND ADDRESS(ES)

Air Force Institute of Technology
Graduate School of Engineering and Management (AFIT/EN)
2950 Hobson Way
WPAFB OH 45433-7765

8. PERFORMING ORGANIZATION REPORT NUMBER

AFIT-ENY-MS-16-M-205

9. SPONSORING / MONITORING AGENCY NAME(S) AND ADDRESS(ES)

Air Force Research Lab RWM
101 West Eglin Blvd
Attn: Donald Littrell
Eglin AFB FL 32542
DSN 872-6802, COMM 850-882-6802
Email: donald.littrell@us.af.mil

10. SPONSOR/MONITOR'S ACRONYM(S)

AFRL

11. SPONSOR/MONITOR'S REPORT NUMBER(S)

12. DISTRIBUTION / AVAILABILITY STATEMENT

DISTRIBUTION STATEMENT A:
APPROVED FOR PUBLIC RELEASE; DISTRIBUTION UNLIMITED.

13. SUPPLEMENTARY NOTES

14. ABSTRACT

Experimental research was conducted to determine the dynamic properties and characterize the microstructure of 15-5PH Stainless Steel manufactured through Direct Metal Laser Sintering (DMLS) additive manufacturing (AM) processes and heat treated using common heat treatment protocols. A thorough understanding of the material's properties is necessary before such parts are utilized in an operational capacity. Of the five builds, two deviated significantly from the specified composition of 15-5PH stainless steel. The remaining three builds, possessing the desired composition and crystalline structure, were tested in compression and tension at two strain rates. Tension tests using a reflected wave and a momentum trap SHB setup collected data reflecting a natural variation within builds and across builds and orientation of typically less than 7%. A slight build orientation bias is noted resulting in higher ductility of the horizontal build orientation compared to the vertical of the same material. A simplistic linear interpolation of true stress-strain curves show fairly consistent strain softening trends at higher strain rates across the material subject sets.

15. SUBJECT TERMS

Additive Manufacturing, Stainless Steel, 15-5PH Stainless Steel, Steel Microstructure

16. SECURITY CLASSIFICATION OF:			17. LIMITATION OF ABSTRACT	18. NUMBER OF PAGES	19a. NAME OF RESPONSIBLE PERSON
a. REPORT	b. ABSTRACT	c. THIS PAGE			Maj David Liu, AFIT/ENY
U	U	U	U	110	19b. TELEPHONE NUMBER *(include area code)* (937) 255-3636, x4518; david.liu@afit.edu